THE INFLUENCE OF FOREST ON THE DISTRIBUTION AND SIZE OF SURFACE HOAR IN SMALL MEADOWS

by

Matthew Allen Wieland

A thesis submitted in partial fulfillment
of the requirements for the degree

of

Master of Science

in

Earth Sciences

MONTANA STATE UNIVERSITY
Bozeman, Montana

November 2015

©COPYRIGHT

by

Mathew Allen Wieland

2015

All Rights Reserved

ACKNOWLEDGEMENTS

I would like to thank Dr. Jordy Hendrikx, Dr. Karl Birkeland, and Dr. Paul Stoy for their advice, support, and guidance during this research. I also thank Dr. Megan Higgs, Jay Rosencrantz, and John Sherrill for their statistical discussions and instruction. I thank Dr. Ed Adams for his thoughts on surface hoar and radiation.

This work could not have been accomplished without the help of my sole field assistant, Maggi Kraft. Your patience after waking early in the morning and standing around in the cold was unwavering. I also thank you for testing the strength and durability of the snowmobiles. Equipment support from the Montana State University Snow and Avalanche Laboratory was vital in performing this research. Thanks to Holt Hancock for the many snow related and off-topic discussions over a pint. Thanks to the Gallatin National Forest Avalanche Center for their discussions and providing weather data.

I am grateful for financial support from the American Avalanche Association, the Barry C. Bishop Scholarship for Mountain Research, and a graduate teaching assistantship through the Earth Science Department at Montana State University.

TABLE OF CONTENTS

1. INTRODUCTION 1

1.1 Background 1
1.2 Research Questions 4

2. LITERATURE REVIEW 5

2.1 Surface Hoar Formation 5
2.2 Surface Hoar Destruction and Changes Post Burial 9
2.3 Surface Hoar In Forests 11
2.4 The Role of Aspect in Surface Hoar Formation 13
2.5 Spatial Variability 14
2.6 Hemispheric Photography 19
2.7 Snow Crystal Sizing 21

3. METHODS 27

3.1 Study Area 27
3.2 Site Selection and Study Sites 30
3.2.1 North Site 33
3.2.2 South Site 34
3.3 Sampling Design 36
3.4 Data Collection 39
3.5 Data Processing 42
3.5.1 Crystal Sizing 42
3.5.2 Hemispheric Photography 44
3.5.3 Camera Calibration 48
3.6 Data Analysis 50
3.6.1 Response Variables 51
3.6.2 Data Exploration 53
3.6.3 Linear Regression Analysis 54
3.6.4 Regression Trees 56
3.6.5 Spatial Analysis 60

4. RESULTS 66

4.1 Attempted Sample Days 66
4.2 Preceding Weather and Avalanche Conditions 67
4.2.1 Jan2014 Event 67
4.2.1.1 North Site 68
4.2.1.2 South Site 71

TABLE OF CONTENTS- CONTINUED

4.2.2 April2014 Event....74
4.2.2.1 North Site....75
4.2.2.2 South Site....75
4.2.3 Jan2015 Event....78
4.2.3.1 North Site....79
4.2.3.2 South Site....84
4.3 Regression Analysis: Single Explanatory Variable....87
4.3.1 Linear Regressions....89
4.3.1.1 Jan2014 North Site....89
4.3.1.2 Jan2014 South Site....90
4.3.1.3 April2014 South Site....90
4.3.1.4 Jan2015 North Site....90
4.3.1.5 Jan2015 South Site....91
4.4 Regression Analysis: Multiple Explanatory Variables....91
4.4.1 Linear Regressions....91
4.4.1.1 Jan2014 North Site....92
4.4.1.2 Jan2014 South Site....92
4.4.1.3 April2014 South Site....93
4.4.1.4 Jan2015 North Site....94
4.4.1.5 Jan2015 South Site....94
4.4.2 Regression Trees....95
4.4.2.1 Jan2014 North Site....96
4.4.2.2 Jan2014 South Site....97
4.4.2.3 April2014 South Site....99
4.4.2.4 Jan2015 North Site....99
4.4.2.5 Jan2015 South Site....101
4.4.2.6 Regression Tree Summary....103
4.5 Spatial Analysis....104

5. DISCUSSION....112

5.1 Environmental Determinants of Surface Hoar Size....113
5.1.1 Jan2014 North Site....115
5.1.2 Jan2014 South Site....116
5.1.3 April2014 South Site....117
5.1.4 Jan2015 North Site....118
5.1.5 Jan2015 South Site....119
5.2 Spatial Structure....120
5.3 Conceptual Model....123
5.4 Site Comparisons....125
5.5 Event Comparisons....127
5.6 Summary Measures....129

TABLE OF CONTENTS- CONTINUED

5.7 Inferences and Uncertainty 130

6. CONCLUSION.....131

7. CHALLENGES AND FUTURE RESEARCH RECOMMENDATIONS.....134

REFERENCES CITED.....136

APPENDICES 145

APPENDIX A: Sampling Layouts.....146
APPENDIX B: Sample Semi-variograms 151
APPENDIX C: Morans's I and Linear Regressions.....155
APPENDIX D: Overfit Regression Trees.....178
APPENDIX E: Camera Calibration.....191

LIST OF TABLES

Table Page

1. Surface Hoar Research Summary 23

2. Crystal Sizes Recorded by ISSW Participants 53

3. Jan2014 Event Summaries for Surface Hoar Size, ψ_{Sky}, $\Sigma_{Sunfleck}$, and $\Sigma_{Shortwave}$ 70

4. April2014 Event Summaries for Surface Hoar Size, ψ_{Sky}, $\Sigma_{Sunfleck}$, and $\Sigma_{Shortwave}$ 77

5. Jan2015 Event Summaries for Surface Hoar Size, ψ_{Sky}, $\Sigma_{Sunfleck}$, and $\Sigma_{Shortwave}$ 83

6. Correlation Coefficients for Environmental Determinants and Surface Hoar Size 88

7. Significant Regressions for the Jan2014 Event at the North Site 90

8. Significant Regressions for the April2014 Event at the South Site 90

9. Significant Regressions for the Jan2015 Event at the North Site 90

10. Significant Regressions for the Jan2015 Event at the South Site 91

11. Significant Multiple Regressions for the Jan2014 Event at the North Site 93

12. Significant Multiple Regressions for the Jan2014 Event at the South Site 93

13. Significant Multiple Regressions for the April2014 Event at the South Site 94

14. Significant Multiple Regressions for the Jan2015 Event at the North Site 94

LIST OF TABLES – CONTINUED

Table Page

15. Significant Multiple Regressions for the Jan2014 Event at the South Site 95

16. Regression Tree Results Summary 104

17. Linear Trend Regression Coefficients 105

18. Extracted Semi-variogram Model Measures 111

LIST OF FIGURES

Figure Page

1. Surface Hoar Variability Over a Small Area 3

2. Scale Triplet 16

3. Regional Map of Taylor Fork Study Area 28

4. Location Map of Taylor Fork Study Sites 31

5. Overview of Taylor Fork Study Sites 34

6. Landscape Perspective of the North Site 35

7. Landscape Perspective of the South Site 35

8. Example Sample Layout 37

9. Random Sample Technique 39

10. Digital Camera and Crystal Card Configuration 40

11. Sample Crystal Card Image 43

12. Hemispheric Image Processing 45

13. Alternative Hemispheric Image Processing 46

14. Hemispheric Image with Sun Track 48

15. Office Calibration of Fisheye Lens 49

16. Field Calibration of Fisheye Lens 50

17. Sample and Model Semi-variogram with Descriptive Parameters 62

18. Temperature and Relative Humidity Measured at the North Site for the Jan2014 Event. 69

19. Boxplots of Sized Crystals and Crystal Size Summary Measures at the North Site for the Jan2014 Event 71

LIST OF FIGURES – CONTINUED

Figure Page

20. Temperature and Relative Humidity Measured at the South Site for the Jan2014 Event 72

21. Boxplots of Sized Crystals and Crystal Size Summary Measures at the South Site for the Jan2014 Event 73

22. Temperature and Relative Humidity Measured at the South Site for the April2014 Event 76

23. Boxplot of Sized Crystals at the South Site for the April2014 Event 77

24. Landscape Perspective of the South Site for the April2014 Event 78

25. Scatterplot of Temperature and Relative Humidity Measurements at the Study Sites 80

26. Estimated Temperature and Relative Humidity at the North Site for the Jan2015 Event 81

27. Hemispheric Perspective of the North Site for the Jan2015 Event 82

28. Boxplots of Sized Crystals and Crystal Size Summary Measures at the North Site for the Jan2015 Event 83

29. Temperature and Relative Humidity Measured at the South Site for the Jan2015 Event 85

30. Large Surface Hoar Crystals at the South Site for the Jan2015 Event 86

31. Boxplots of Sized Crystals and Crystal Size Summary Measures at the South Site for the Jan2015 Event 86

32. Scatterplots of $Size_{90th}$ vs. $\Sigma_{Sunfleck}$ and $\Sigma_{Shortwave}$ 88

33. Scatterplots of $Size_{Mean}$ vs. $\Sigma_{Sunfleck}$ and ψ_{Sky} 89

34. Overfit Regression Tree for $Size_{90th}$ at the North Site for the Jan2014 Event 97

LIST OF FIGURES – CONTINUED

Figure Page

35. Pruned Regression Tree for $Size_{Mean}$ at the South Site for the Jan2014 Event 98

36. Pruned Regression Tree for $Size_{90th}$ at the South Site for the Jan2014 Event 98

37. Pruned Regression Tree for $Size_{Max}$ at the South Site for the Jan2014 Event 99

38. Pruned Regression Tree for $Size_{Mean}$ at the North Site for the Jan2015 Event 100

39. Pruned Regression Tree for $Size_{90th}$ at the North Site for the Jan2015 Event 100

40. Pruned Regression Tree for $Size_{Max}$ at the North Site for the Jan2015 Event 101

41. Pruned Regression Tree for $Size_{Mean}$ at the South Site for the Jan2015 Event 102

42. Pruned Regression Tree for $Size_{90th}$ at the South Site for the Jan2015 Event 102

43. Pruned Regression Tree for $Size_{Max}$ at the South Site for the Jan2015 Event 103

44. Sample and Model Semi-variograms for $Size_{Mean}$ at the South Site for the Jan2014 Event.....106

45. Sample and Model Semi-variograms for $Size_{Max}$ at the South Site for the Jan2014 Event.....107

46. Sample and Model Semi-variograms for $Size_{Mean}$ at the North Site for the Jan2015 Event.....108

47. Sample and Model Semi-variograms for $Size_{90th}$ at the North Site for the Jan2015 Event.....108

LIST OF FIGURES – CONTINUED

Figure Page

48. Sample and Model Semi-variograms for $Size_{Max}$ at the North Site for the Jan2015 Event....109

49. Sample and Model Semi-variograms for $Size_{90th}$ at the South Site for the Jan2015 Event....109

50. Sample and Model Semi-variograms for $Size_{Max}$ at the South Site for the Jan2015 Event....110

51. Conceptual Model....124

52. Hypothetical Crystal Sample....129

ABSTRACT

Snow avalanches pose a significant hazard to winter recreationalists travelling in the backcountry and are difficult to predict on individual slopes. Weak layers responsible for these avalanches may form at the surface multiple times during the winter season and are buried by subsequent snowfall. Understanding causes of slope-scale weak layer variations during formation and destruction periods is crucial for gaining an understanding of their distribution after burial. Persistent weak snow layers, such as surface hoar, can pose hazards for months after burial. This study examines surface hoar crystals on the surface, directly after formation, in two small meadow openings in southwest Montana. Data collection occurred during two winter seasons for three surface hoar formation events. Three environmental metrics associated with surface hoar growth processes in meadow openings are explored and their relationships with crystal size examined using spatial regression and regression tree analysis. The spatial structure for each event is described using multiple crystal sizing measures through semi-variograms. Surface hoar crystals tended to grow largest in areas that were both shaded and possessed large unobstructed views of the sky on north and south aspects. The range of spatial autocorrelation for surface hoar crystal sizes varied from 7 m to beyond 25 m and differed depending on event or crystal sizing measure. Results vary between events and suggest the drivers controlling surface hoar growth are unique to each area and not consistent between events. This research highlights the need for multiple slope-scale snow stability assessments for understanding the distribution of a buried weak layer of surface hoar in a meadow opening. Targeted areas for assessment should incorporate a basic understanding of a meadow's shading and canopy openness and how this varies over a winter season.

1. INTRODUCTION

1.1 Background

Snow avalanches are natural hazards that pose significant threats to humans and infrastructure. These hazards are found worldwide and cause injuries, the loss of human life, and structural damage. Every year, millions of dollars are used for avalanche control measures and repairs to damaged infrastructure (McClung and Schaerer, 2006). Avalanche fatalities in the United States often involve snowmobilers and backcountry tourers and fatalities have increased over the past sixty years (CAIC, 2015). Fatalities during the 2013-2014 winter season totaled 35, of which six were located in Montana.

Two common avalanche release types are loose snow and slab (Schweizer et al., 2003). Slab avalanches occur when a trigger (e.g. a skier) initiates a crack that propagates in a relatively weaker snow layer that lies below stronger, more cohesive snow known as a slab. Depending on the snow grain form, weaker snow layers may gain strength rapidly and only pose threats lasting for a few hours to days. Some weak layers produce instabilities lasting for weeks, months, or an entire season. These layers are known as persistent weak layers and account for a majority of the weak layer types in slab avalanches (Jamieson and Johnston, 1992). Persistent weak layers can propagate fractures from remote triggers over long distances and involve very large avalanches. Often, triggering persistent layers becomes more difficult as a layer ages, but the avalanche size and resulting hazard becomes greater (McClung and Schaerer, 2006). Common persistent weak layer crystal forms include surface hoar, depth hoar, and faceted crystals.

Understanding the distribution of persistent weak layers is of utmost importance to backcountry users and avalanche forecasters. While the general growth conditions for each persistent layer type are relatively well known and have been the focus of extensive research (e.g. Lang et al., 1984; Gubler, 1984; Colbeck, 1988; Hachikubo and Akitaya, 1997; Hachikubo, 2001; Feick, 2007), being aware of or forecasting the locations and inherent variability for these layers remains difficult. While in the field, backcountry users assess slopes for the purpose of travelling in or near these areas. They conduct slope investigations with multiple assessment methods, but most approaches require digging into the snow to examine its properties and conduct stability tests. Without the ability to sample an entire slope exhaustively, limited internal snowpack observations are conducted at locations that are relatively safe but will hopefully provide crucial information about the surrounding slope (Schweizer et al., 2003). While observations are limited, using information from a single snow pit may not accurately represent the weak layer distribution or entire slope's stability. By conducting multiple well-placed stability tests, false-stable results may be reduced (Birkeland and Chabot, 2006). However, the spacing and location of these tests is difficult to determine and varies depending on the weak layer type or slope (Birkeland et al., 2010). Understanding probable persistent weak layer locations allows backcountry users to target these layers in stability tests or practice avoidance of potential unstable areas.

Surface hoar crystals form at the snow surface and become covered by snowfall, forming a buried weak layer. Buried surface hoar accounts for 30% of the avalanches along Snoqualmie Pass, ~50% of the avalanches in the Snake River Range, and 59% of

the of avalanches in Canada (34% of fatal avalanches) (Breyfogle, 1986; Jamieson and Johnston, 1992; Schweizer and Jamieson, 2001; American Avalanche Institute, 2014). Surface hoar variability is present across multiple spatial scales and is affected by differing mechanisms depending on the spatial extent (Fig. 1). Variability, in presence/absence and size, exists from differing meteorological conditions and radiation balances during formation. This variability is further increased by destructive mechanisms (e.g. wind or solar radiation) due to its fragility. Predictions of surface hoar are confounded as the time periods and meteorological conditions during formation and destruction are not known.

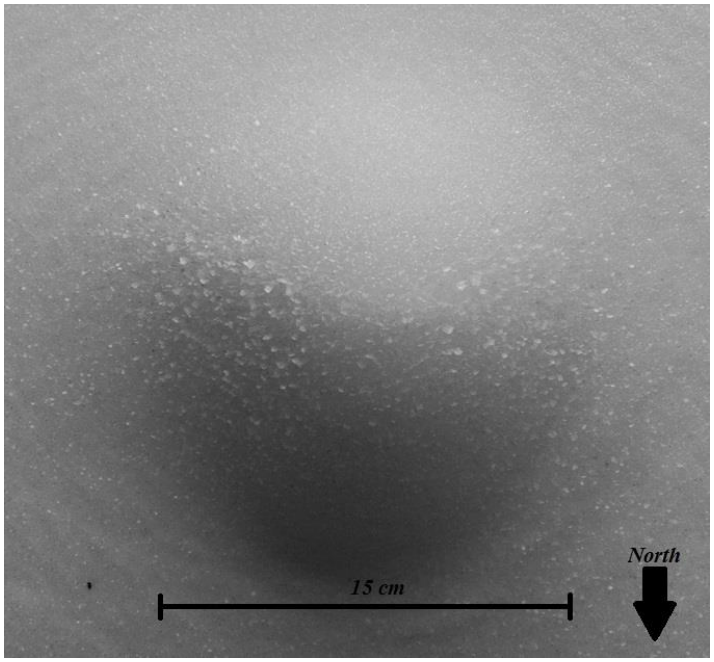


Figure 1. A 15 cm diameter mound of snow with variations in surface hoar size across the small feature.

The stochastic nature and weak correlations with many physical and meteorological processes makes prediction of surface hoar formation at the slope and

mountain range scales inherently difficult. By identifying effective environmental proxies that lead to this variability on individual slopes, backcountry users and forecasters gain an improved capacity in evaluating the avalanche hazard when a buried surface hoar layer exists.

1.2 Research Questions

The objective of this study is to further the understanding of un-buried surface hoar crystals at the slope scale at two small forested meadow openings in southwest Montana over multiple formation events. Specifically, I examine several environmental proxies related to surface hoar growth and quantify their relationship with surface hoar crystal size. Also of interest are the spatial patterns of surface hoar crystals across these two meadows. The specific research questions addressing these interests are: 1) What is the relationship between slope-scale vegetation cover, shading, and solar radiation with surface hoar crystal size at a meadow for a formation event; and 2) what are the slope-scale spatial patterns of surface hoar crystal size across a meadow for each formation event?

2. LITERATURE REVIEW

2.1 Surface Hoar Formation

Surface hoar, or hoar frost as it has been termed outside of avalanche research, has been a topic of interest in snow research dating back to the 1930's (e.g. Nakaya, 1935; Seligman, 1936). Surface hoar crystals are striated or needle-like ice crystals that grow on the snow surface (Fierz et al., 2009). These crystals form through the deposition of water vapor from a saturated air mass onto the snow surface. This process begins with a cooling of the snow surface due to longwave energy losses to a clear atmosphere. The cold snow surface in turn cools the surrounding air mass resulting in a supersaturated parcel of air (respective to the snow surface) directly above (Lang et al., 1984). A large vapor pressure gradient forms at the air-snow boundary which results in the deposition of water vapor directly onto the snow surface from the saturated air mass (McClung and Shaerer, 2006). If deposition occurs for a sufficient amount of time, surface hoar crystals form. The types of crystals that form depend mainly on air temperatures during formation and to a lesser extent, the excess vapor density over ice (McClung and Schaerer, 2006). Typical surface hoar forms include striated, flat crystals with occasional needle-like forms (Fierz et al., 2009).

While early avalanche research qualitatively understood a weak layer of surface hoar is an important element in avalanche formation (e.g. Perla and Martinelli, 1976), few quantitative studies on the formation conditions, destructive mechanisms, and subsequent changes post burial were conducted for some time.

Lang et al. (1984) was one of the first field studies to thoroughly investigate overnight formations of surface hoar in a mountain environment. This study used a topographically flat area with few surrounding obstructions to reduce the effects of emitted or reflected radiation from these objects onto the snow surface. Thermocouples, placed on the snow surface, measured snow temperatures which were used for computations of temperature gradients during surface hoar formation periods. Observations of surface crystals and meteorological conditions of several overnight surface hoar events near Big Sky, MT, USA during two winter seasons were examined. Surface hoar crystals grew overnight in relation to the parent grain orientation of surface crystals while secondary growth forms were "oriented more randomly" (Lang et al., 1984). Air temperatures during "plate-like" growth ranged between -12.5° C and -21° C with near surface temperature gradients reaching a maximum of 380° C/m. Surface growth of "needle-like" crystals was observed for air temperatures below -21° C. During formation periods, slight horizontal air movement as well as "high cirruform [sic]" cloud conditions were hypothesized to inhibit surface hoar formation at their site (Lang et al., 1984) (Table 1).

At a similar time, studies on surface hoar growth focused on the specific meteorological conditions necessary for a formation event. Observations of surface hoar growth on mirrors placed in the field indicated favorable growth conditions occurred when the relative humidity was between 10% and 100% (Gubler, 1984). A smaller relative humidity range was given by Breyfogle (1986) who found optimum surface hoar growth occurred when the relative humidity was greater than 70% (Table 1). This study

also noted that small amounts of air movement are needed to replenish moisture in the air parcel after deposition to continue the process. However, too much movement was thought to destroy any temperature inversion. Both studies fail to mention the heights meteorological measurements were taken.

Later research supported the assertion that some air movement is needed for surface hoar formation. Colbeck (1988) found observed surface hoar growth rates could not be achieved simply through vapor diffusion onto the surface layer. While this mechanism may be sufficient during the initial stages of surface crystal growth, it could not account for crystal growth rates observed in mountain environments (Colbeck, 1988) (Table 1). Hachikubo and Akitaya (1997) found optimum surface hoar growth conditions in maritime environments occur when wind speeds are 1-2 m/s (measured at a height of 10 cm). They also note that, in general, optimal surface hoar growth occurs when snow surface temperatures are 5° C lower than the air temperature and the relative humidity is greater than 90% (measured at a 10 cm height). Later research indicated that for relative humidities less than 80% (measured at a 10 cm height), a specific wind speed between 0-6 m/s optimized sublimation rates (Hachikubo, 2001). When the relative humidity is greater than 90% (measured at a height of 10 cm), sublimation rates increased when wind speeds were in the 0.5-3.5 m/s range (Hachikubo, 2001) (Table 1).

The introduction of heavily instrumented field study sites allowed calculations of latent heat fluxes and rates of mass deposition and sublimation for *in situ* surface hoar studies. Feick et al. (2007) measured surface hoar growth near four alpine weather stations over multiple surface hoar formation events. The correlation between calculated

sublimation rates and surface hoar growth was poor and positive latent heat fluxes were observed to have little effect on the growth or destruction of surface hoar crystals. In their alpine terrain, predictions of surface hoar growth using sublimation rates was deemed unreliable unless small scale winds (<10 m) were known (Table 1). Stossel et al. (2010) expand on this research by using eddy covariance measurements to calculate latent heat fluxes. Additionally, they placed field lysimeters to measure snow mass changes before and after formation events. They found turbulent latent heat fluxes were a contributing factor in providing a moisture source during surface hoar formation. They also noted a weak trend between deposited mass (measured by lysimeters) and maximum crystal size, but conducted no quantitative analysis (Table 1).

The research in this section highlights the importance of lower (but not calm) wind speeds, relatively colder snow/air temperatures, relatively higher relative humidities, and clear overnight sky conditions for surface hoar formation. Synoptic weather patterns that may foster these conditions tend to be high pressure systems that move colder air into mountain areas (Yokley et al., 2014). Numerical weather forecasts have been used in snow cover models to predict surface hoar formation. Horton et al. (2014) investigated latent heat fluxes and vapor mass flux on surface hoar growth using a Canadian numerical weather forecast and the SNOWPACK snow cover model. A GEM15 weather forecast model was run for a 15 km grid in the Columbia Mountains, British Columbia and integrated into the snow model. Results suggested that surface hoar formation events could be predicted using the forecasted weather at this grid scale (Table 1).

2.2 Surface Hoar Destruction and Changes Post Burial

After initial growth and prior to burial, surface hoar may be pushed over, reduced in size, or completely destroyed by elements such as avalanches, solar radiation, wind, above freezing air temperatures, or rain (McClung and Schaerer, 2006). These natural elements may act independently or in unison to produce irregular spatial patterns of surface hoar.

Direct solar radiation alters surface hoar by melting part or all of a crystal, or increasing sublimation rates resulting in a reduction of crystal mass (Feick et al., 2007; Armstrong and Brun, 2008). While several studies mention these influences on surface hoar crystals (e.g. Schweizer and Kronholm, 2007; Helbig and van Herwijnen, 2012), others have noted that even with large amounts of direct solar radiation, surface hoar crystals survived or changed insignificantly (Shea and Jamieson, 2011; Feick et al., 2007). These opposing findings may be a function of latitude or time of year which result in large differences in radiation amounts (Oke, 1987).

Wind influences surface hoar by mechanically pushing crystals over, or increasing sublimation rates which reduce crystal mass (McClung and Schaerer, 2006; Gubler, 1998). Feick et al., (2007) found winds destroyed surface hoar on individual slopes (due to localized gusts) and at larger spatial extents (due to windward prevalence). They also noted a reduction in crystal size with increasing sublimation rates (Table 1). However, even when calculated sublimation rates have indicated evaporation should have eradicated crystals, they have been observed to survive (Hachikubo and Akitaya, 1998).

The individual effect of any one of these destructive mechanisms may be difficult to deduce when multiple temporal observations cannot be conducted. Schweizer and Kronholm (2007) postulated that surface hoar destruction in their study was due to the combined effects of wind and solar radiation.

After burial, surface hoar crystals are considered a layer with defined boundaries and a burial date is recorded if known (Greene et al., 2010). Buried surface hoar layers can persist for several months with few changes in crystal texture but with noticeable decreases in weak layer height and increases in shear strength (Davis et al., 1996; Jamieson and Schweizer, 2000) (Table 1). Larger surface hoar crystals tend to persist longer and form fewer bonds than smaller surface hoar crystals (Jamieson and Schweizer, 2000). Larger buried crystals bond at slower rates than smaller crystals which may be due, in part, to the number of snow grains that fall between crystals (Davis et al., 1996). Larger crystals also persist longer than smaller crystals as dry-snow metamorphism tends to preserve them (Jamieson and Schweizer, 2000). As load on a buried layer increases from subsequent snowfall, surface hoar crystals penetrate into layers above and below. This penetration increases the number of bonds that form at the layer boundaries (Jamieson and Johnston, 1999). Shear strength of buried layers usually increases over time and may become more variable on individual slopes (Birkeland et al., 2004b; Logan, 2005). While larger crystals (or thicker layers) are commonly thought to stabilize more slowly and harbor relatively lower shear strengths, both Zeidler and Jamieson (2006) and Horton et al. (2014) found poor correlations with these parameters and measured shear strengths.

2.3 Surface Hoar in Forests

Avalanche terrain in mountain environments can exhibit large changes in elevation, and differing amounts and types of vegetation cover. These environmental factors affect the local climate and alter wind speeds, air temperatures, snowfall amounts, and radiation balances which then directly alter the surrounding snowpack (Oke, 1987; McClung and Schaerer, 2006). Knowing how environmental factors influence meteorological conditions and subsequently the snowpack is crucial in understanding weak layer formation and evolution.

Gubler and Rychetnik (1991) documented the effects of forests on the formation of surface hoar and other avalanche weak layers. Three forest stands (one surrounded by larch trees and two surrounded by spruce trees) and one open study plot were investigated during four winter seasons. They found the surrounding forest canopy altered shortwave and longwave radiation balances, wind speeds, air temperatures (measured at 2 m heights), and precipitation reaching the forest floor (Gubler and Rychetnik, 1991). While no snow surface temperature measurements were recorded, temperatures directly below the snow surface were measured. Differences between sub-surface temperatures and air temperatures were reduced in spruce stands (1.5° C) when compared to open fields (10° C). With such small differences between sub-surface and air temperatures, "…formation of surface hoar under spruce trees is very unlikely." (Gubler and Rychetnik, 1991). Summarizing their discussion, Gubler and Rychetnik (1991) hypothesize that surface hoar formation is most effective in areas that have a large view to the sky but are also shaded from incoming solar radiation (Table 1).

Later studies investigated the effects forests have on the meteorological factors associated with surface hoar formation. Using an open field and two areas in a larch forest (a small 6 m x 6 m clearing and a site with dense tree cover), Holler (1998) observed similar diurnal air temperatures and relative humidities among the study sites. The largest difference between sites was the radiation balance, which was influenced directly by the forest canopy. Holler (1998) suggests surface hoar growth occurs in forest clearings when the relative humidity is >75% and in larch forests with high canopy densities, when the relative humidity is greater than 95% (Table 1). Holler (2001) later investigated snow surface temperatures with respect to forest cover in stone pine stands. Again, measured air temperatures between sites were relatively similar yet differences in the amount of incoming longwave radiation and snow surface temperatures were large. Measured snow surface temperatures were 3-7° C cooler in the open field when compared to the forested sites. For areas with larger canopy covers (i.e. smaller unobstructed view of the sky), they attributed reduced snow surface cooling to the greater amounts of emitted longwave radiation from the canopy (Table 1).

Later studies show how influential incoming longwave radiation is on snow surface temperatures and surface hoar formation. Slaughter (2010) found the amount of incoming longwave radiation incident at the snow surface was the most important parameter when investigating the presence/absence of surface hoar at The Yellowstone Club in Big Sky, Montana. One of Slaughter's (2010) sites was later used for an investigation into modelled longwave radiation and snow surface temperatures when trees at the site were snow-covered and snow-free. Incident incoming longwave radiation

was lower at the snow surface when trees were snow covered. The lower incoming longwave radiation resulted in lower modelled snow surface temperatures (Adams et al., 2011) (Table 1).

Lutz (2009) investigated a layer of buried surface hoar at a small, north-east facing meadow opening in southwest Montana. Measurements of layer thickness and shear strength of a buried surface hoar layer were compared to measurements of canopy cover and estimations of incoming longwave and shortwave radiation. Longwave radiation was estimated using canopy and sky measurements (estimated from site images and GIS models) and their associated emissivities (also estimated). Areas that received the greatest amount of incident longwave radiation (typically in areas with the highest canopy cover), the largest amount of direct solar radiation, or both, harbored thinner surface hoar layers. Similar studies have shown that simple estimates of canopy cover are correlated with surface hoar crystals sized on the snow surface at north facing locations (Shea, 2011) (Table 1).

2.4 The Role of Aspect in Surface Hoar Formation

Slope aspect influences the snow surface and surface hoar formation due to differences in radiation balances. North facing snow temperatures are generally colder and less influenced by direct solar radiation as compared to southerly facing aspects due to lower angles of incidence to the sun and enhanced shading (Holler, 2001; McClung and Schaerer, 2006; Adams, 2011). These effects change throughout the winter season as solar elevation angles become greater in the latter part of the winter. An investigation by

Cooperstein (2008) found overnight formations of surface hoar crystals were significantly larger on north facing slopes when compared to south facing slopes. Larger incoming shortwave radiation amounts on southern slopes were attributed to this difference (longwave radiation was not measured). However, other surface hoar research (e.g. Feick et al., 2007) notes aspect was only a minor influence on surface hoar formation when studied at larger spatial extents (Table 1).

The coupling of aspect and terrain/vegetation influences on multiple aspects has received little attention. Recall that Gubler and Rychetnik (1991) assert surface hoar will grow largest in areas with greater sky visibility and lower solar radiation amounts based on observations from their north facing study areas. While Lutz (2009) studied a northeast facing slope, he too hypothesized that surface hoar on southerly slopes would grow larger and persist longer in areas that possess larger skyviews and are shaded. The intertwined influence of canopy cover and radiation on surface hoar for southern aspects has only briefly been investigated by Hendrikx et al. (2012) and Hendrikx et al. (2014). These studies found differences in skyview at study sites influenced surface hoar formation and noted this factor was more important than elevation or aspect.

2.5 Spatial Variability

For recreationalists, forecasters, and researchers, the question of not only when, but where an avalanche will occur are important considerations when travelling in avalanche terrain (Schweizer et al., 2003). Understanding the inherent spatial variability of snowpack properties, including weak layers such as surface hoar, is an important

element when forecasting for avalanches (McClung and Schaerer, 2006). Previous snow and avalanche studies focus on temporal snowpack observations and spatial observations distributed over a variety of distances (Schweizer et al., 2008). These spatial studies examine snowpack characteristics over a variety of spatial scales and distances.

The term ‘scale’ refers to a “characteristic length or time” and is a fundamental concept when examining spatial variability of snow related processes (Bloschl, 1999). Scales used for snow studies are: grain (0.1 mm – 1 cm), layer (1 cm – 0.5 m), snowpack (0.5 m – 5 m), slope (5 m – 100 m), basin (100 m – 1 km), and mountain range (0 km – 100 km). These scales are used to quantify differing types of processes in snow and hydrologic data (Bloschl, 1999).

Three types of scale dimensions are of interest: process scale, measurement scale, and model scale. The process scale refers to the spatial dimension of the natural variability of a parameter of interest. The correlation length (or integral scale) is the distance at which this parameter is no longer correlated and is the most common way to define a process scale. The correlation length is typically calculated using variogram analysis. Variograms (or semi-variograms) are constructed with an assumption of local stationarity and the integral scale is extracted using the distance where the variogram flattens (Bloschl, 1999).

Measurement scale refers to the spatial dimensions of a sampling scheme and consists of a ‘scale triplet’. The scale triplet refers to the spacing, extent, and support of samples and the sampling area over which the data are being collected (Bloschl, 1999) (Fig. 2). The sample spacing is the distance between measurements and can be constant

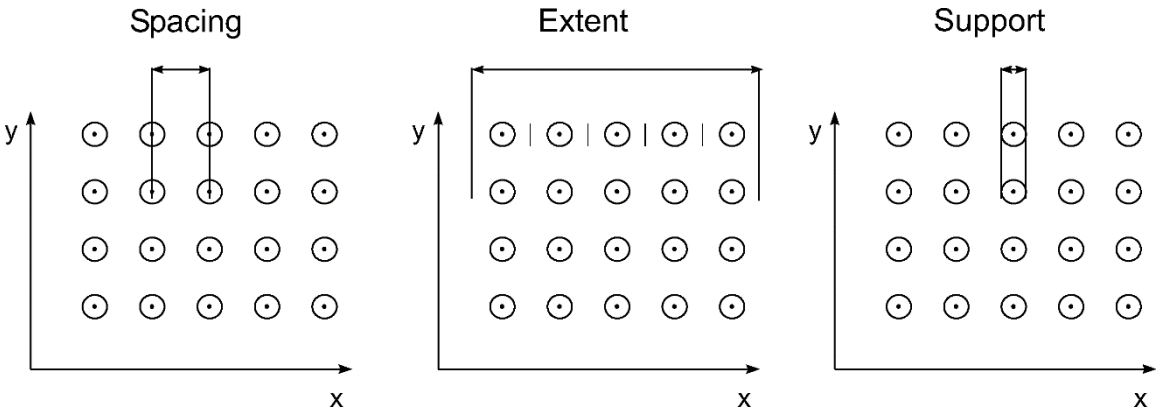


Figure 2. Representation of the scale triplet showing the spacing, extent, and support (adapted from Bloschl (1999)).

(such as in gridded sampling layouts) or varying (such as in random sampling). The observation extent is a measure of the total distance the data are sampled (e.g. a small meadow or an entire mountain range) (Fig. 2). The observation support is the area or volume each sample represents (Bloschl, 1999) (Fig. 2). Support for measurements in snow avalanche studies at the slope scale range from <10 m^{-4} (SnowMicroPen) up to 3.0 m^2 (Rutschblock). The model scale is the spatial dimension of a model and also consists of a scale triplet.

Scaling refers to a change between any of the three scale types. The effects of scaling are the introduction of possible biases and uncertainty in the analyses. When designing a study, the scale triplet and scaling issues must be taken into account when determining a sampling scheme, conducting analyses, or comparing similar studies. Failure to account for this will result in biases and/or uncertainties in the results and misinterpretations (Skoien and Bloschl, 2006).

Surface hoar studies have used a variety of spatial scales. These studies have focused on surface hoar crystals (crystal size), directly on surface hoar layers (shear

frame test), or indirectly on surface hoar layers (stability test). Spatial scales for these studies include the slope scale (e.g. Landry, 2002; Birkeland et al., 2004a; Birkeland et al., 2004b; Logan, 2005; Lutz, 2009, Birkeland et al., 2010), basin scale (e.g. Hendrikx et al., 2012; Feick et al., 2007), range scale (e.g. Borish et al., 2012; Helbig and van Herwijnen, 2012; Colbeck et al., 2008), or multiple scales (e.g. Schweizer and Kronholm, 2007).

Slope-scale studies of surface hoar focus on the determination of slope-scale trends through examination of crystal size, buried layer thickness and associated shear strength, or stability tests whose failure is on a surface hoar layer. Landry (2002) found variations in shear strength on differing ages of buried surface hoar layers across 30 m x 30 m study sites. Logan (2005) observed very little spatial structure or evidence of autocorrelation at one of Landry's sites. Lutz (2009) found variations in both shear strength and weak layer thickness on a buried surface hoar layer on a northeast facing 30 m x 30 m site. Birkeland et al. (2010) used parts of Landry's, Logan's, and Lutz's datasets along with several other unpublished datasets to examine optimal stability test spacing. For surface hoar layers, optimal spacings ranged from 0 m to 50 m and varied between datasets and location.

Basin-scale studies mainly focus on the presence/absence of surface hoar formation and/or destruction. While no spatial analysis was conducted, Hendrikx et al. (2012) and Feick et al. (2007) found variations in surface hoar presence/absence in 3-9 km^2 areas. Aspect was not well correlated surface hoar formation, and smaller scale variability in meteorological conditions may have been the primary driver during

formation (Hendrikx et al., 2012). Destruction of crystals by wind is also noted for several spatial scales (Feick et al., 2007).

With difficulty in accurately measuring meteorological conditions at a large number of locations, range-scale surface hoar studies have investigated topographic effects on surface hoar formation. Borish et al. (2012) found higher elevations harbored larger surface hoar and hypothesized spatial patterns of surface hoar were linked to katabatic winds which are altered by topography. Others have also highlighted the importance of terrain parameters for formation in measured (e.g. Schweizer and Kronholm, 2007) and modeled (e.g. Helbig and van Herwijnen, 2012) surface hoar studies.

Spatial studies on the variability of surface hoar layers have focused on measurements taken after a layer is buried (e.g. Landry, 2002; Kronholm 2004; Lutz, 2009; Logan, 2005). Studies using buried layers have an advantage as the extraction of a usable metric (e.g. extended column test) can be related to stability. However, relating a stability metric to formation and destruction processes is difficult as conditions during each phase are usually unknown.

Few slope-scale studies examine the spatial distribution of surface hoar crystals on the surface (e.g. Schweizer and Kronholm, 2007; Shea, 2010b). Surface crystals are not considered a layer (or hazard) and stability metrics are difficult to attain (e.g. shear frame). Results based on surface layers are not easily related to future instability as crystals may be altered or destroyed before burial (Shea, 2010b). Surface layers can undergo further growth or destruction phases after sampling but before burial that

potentially invalidate results from a snapshot study. However, it is possible for winter storms to bury surface hoar crystals directly after overnight formation with a limited or non-existent destructive phase.

2.6 Hemispheric Photography

Hemispheric (fisheye) photography is the use of a camera with an attached lens in capturing an extremely wide angle image. Upwards looking hemispheric images are used in ecology for estimations of canopy characteristics (e.g. leaf area index, canopy cover), forest light environments, and radiation (Essery et al., 2008). Early estimates of forest canopy cover were produced with handheld devices that crudely estimated canopy characteristics, did not cover an entire 180° viewshed, and could not record a scene for later analysis (Lemmon, 1956). Film and digital photography allow for the capture of a hemispheric image for a later, more thorough processing and examination. Canopy images are captured using extreme wide-angle fisheye lenses or spherical mirrors (e.g. Solar Pathfinder^{TM}). After an image is recorded, computer programs allow for detailed calculations of canopy characteristics and radiation estimates.

An initial step in image analysis is conversion of a color image into binary classes of sky (white) and canopy (black) by a process termed thresholding (Frazer et al., 2001). While manual thresholding is possible, automatic methods produce more accurate and less biased results (Nobis and Hunziker, 2005). Threshholded images are then analyzed using image processing software. These programs produce environmental estimates such as sky visibility (or alternatively canopy cover) or leaf area index. They also allow for

estimations of shortwave radiation through sun tracking algorithms and basic radiation models. Relatively accurate estimations of total shortwave radiation (within ~ 1 MJ of measured radiation) have been calculated on a daily basis using an images geographic coordinates coupled with a sun tracking algorithm and known or estimated atmospheric properties (Hardy et al., 2004).

Snow studies have used hemispheric photography for estimations of canopy cover (or sky visibility) and short or longwave radiation (Holler, 2001; Essery et al., 2008; Lutz, 2009; Shea, 2010). While canopy estimations are relatively straightforward, estimations of incoming longwave radiation are difficult as several assumptions are made. Several snow studies conducted in forests estimated incoming longwave radiation using a modified Stefan-Boltzmann equation that accounts for areas of sky and areas of canopy (e.g. Bader and Weilenmann, 1992; Holler, 2001; Lutz, 2009). Estimates of total incoming longwave radiation at specific locations were made using temperatures and known emissivities for air parcels and canopy types. Canopy temperatures were set to measured air temperatures (measured at varying heights depending on the study) which is an assumption that may not always be met due to differential heating and cooling of forest canopy during the night (Adams et al., 2011; Pomeroy et al., 2009). This assumption is only occasionally valid and can lead to erroneous radiation estimates (Pomeroy et al., 2009).

2.7 Snow Crystal Sizing

The size of an individual snow crystal is the measurement of the crystal along the axis of greatest extension (Fierz et al., 2009). For an entire snow layer, the reported grain size is the average of all individual grains but may also include the average maximum size (Fierz et al., 2009). Snow studies have used differing methods of snow crystal sizing in their analysis. Baunach et al. (2001) used three methods to quantify crystal sizes for samples of faceted crystals. These methods include: sieving crystals through different sized sieves and finding the greatest weight fraction for a sample; using image analysis software to find the average and maximum crystal diameter; and sending macrophotographs of crystals on a 2 mm grid for sizing by avalanche experts. Surface hoar studies have used a number of approaches for characterizing surface hoar crystal size at a single sample point. Chalmers et al. (2001) tracked a layer of buried surface hoar and used the minimum and maximum crystal size along with the layer thickness (measured separately from surface hoar crystals) in their analysis. This same technique was employed by Jamieson and Johnston (1999) who found maximum crystal size was significantly correlated to strength changes over time. Feick et al. (2007) characterized point measurements of surface hoar crystals as a size range. The lower number represented the mean grain size while the upper represented the mean maximum grain size. Mean maximum grain size was ultimately chosen for their analysis. Stossel et al. (2010) used both *in-situ* and laboratory crystal sizing to arrive at summaries of average and maximum crystal size for a point. The maximum crystal size was chosen for their analysis. Analyses have used average surface hoar size which was determined by using

the mean crystal size of a sample (e.g. Borish et al., 2012) or by calculating a mean after determining the minimum and maximum crystal size at a sample point (e.g. Shea, 2010). The use of a variety of crystal sizing methods makes comparisons between studies difficult as sizing techniques and crystal size summary measures may be different.

For reference, Table 1 provides a summary of key findings from prior surface hoar research.

Table 1. Summary of surface hoar research which forms a basis for this study.

Reference	Location	Study Extent	Property	Relevant Observations
Gubler (1984)	n/a	n/a	Crystal Growth	Favorable conditions for surface hoar growth occur when relative humidity is between 10% and 100% and depends on air temperature.
Lang et al. (1984)	Big Sky, MT	Single Slope	Crystal Growth, Shear Strength	Surface hoar crystals formed with large temperature gradients between the air/snow on calm, clear nights. Primary crystals grew oriented to the parent grain but secondary crystal growth was oriented more randomly.
Breyfogle (1986)	Snoqualmie Pass, WA	Mountain Range	Crystal Growth	Prime conditions for surface hoar growth occur when the relative humidity is >70%.
Colbeck (1988)	n/a	n/a	Crystal Growth	Surface hoar crystals cannot grow from purely diffuse conditions and require air movement for the replenishment of moisture.
Gubler and Rychetnik (1991)	Unknown	Multiple Slopes	Crystal Growth	Surface hoar growth in forests is most effective in areas that are shaded but with large unobstructed views to the sky.
Davis et al. (1996)	Cariboo Mountains, BC	Single Slope	Crystal Size, Layer Thickness, Shear Strength	Wedge shaped crystals create an ‘umbrella effect’ for subsequent snowfall. Shear strength of buried layers increased over time while crystal size changed very little.
Hachikubo and Akitaya (1997)	Hokkaido, Japan	Single Slope	Crystal Growth	Optimum conditions for surface hoar growth occurred when wind speeds were 1-2 m/s at 0.1 m high, relative humidity was 90%, and the snow surface was 5° C lower than the air temperature. Crystal growth changed aerodynamic roughness which altered bulk transfer coefficients.
Holler (1998)	Innsbruck, Austria	Multiple Slopes	Effects of Forest	Radiation balances and snow surface temperatures are altered by forest canopy. Surface hoar growth is possible mainly in open terrain but may occur in forests if the relative humidity is >75% or >90% in dense canopy with moderate winds.

Table 1 Continued.

Reference	Location	Study Extent	Property	Relevant Observations
Hachikubo and Akitaya (1998)	Hokkaido, Japan	Slope	Crystal Growth	Surface hoar crystals survived on the snow surface for several days even when calculated evaporation rates were conducive to the disappearance of crystals.
Jamieson and Johnston (1999)	Columbia Mountains, BC	Multiple Slopes	Shear Strength	Gains in shear strength of surface hoar layers was noted over time and correlated best with maximum crystal length, snowpack depth, and slab thickness.
Jamieson and Schweizer (2000)	Columbia Mountains, BC	Multiple Slopes	Crystal Size, Layer Thickness, Density, Shear Strength	Once buried, larger surface hoar crystals tended to retain their size although shear strength gains occurred more slowly. Buried layers showed a decrease in layer thickness and increase in shear strength over several months.
Hachikubo (2001)	Hokkaido, Japan	Single Slope	Crystal Growth	Sublimation rates were linked with wind specific speeds when winds were 0-6 m/s and relative humidities were <80% but increased with higher wind speeds when relative humidity was >90%.
Holler (2001)	Tyrol, Austria	Multiple Slopes	Effects of Forest	Snow surface temperatures were strongly influenced by forest canopies and warmer in forested areas than open fields.
Feick et al. (2007)	Davos, Switzerland	Basin	Crystal Growth and Distribution	Latent heat fluxes were not correlated well with surface hoar growth. Surface hoar destruction was due to wind and shortwave radiation. Variability in basin scale distributions were noted due to formation and destructive mechanisms acting at different spatial scales.
Schweizer and Kronholm (2007)	Davos, Switzerland	Slope – Mountain Range	Crystal Growth and Distribution	Surface hoar destruction from wind and solar radiation was noted. Influences on the spatial distribution surface hoar varied and spatial autocorrelation lengths changed depending on the observation scale.

Table 1 continued.

Reference	Location	Study Extent	Property	Relevant Observations
Cooperstein (2008)	Big Sky, MT	Multiple Slopes	Crystal Growth	Surface hoar crystals grew larger on north facing slopes when compared to south facing slopes. Size differences were attributed to differences in vapor pressure gradients and incident solar radiation.
Shea (2010b)	Columbia Mountains, BC	Multiple Slopes	Crystal	Large variations in surface hoar crystal size were found in areas ~40 m^2. Reasonable estimations of crystal size are possible using satellite photography.
Slaughter (2010)	Big Sky, MT	Multiple Slopes	Crystal Growth	Incoming longwave radiation, snow surface temperature, and relative humidity were most strongly related to surface hoar presence/absence.
Stossel et al. (2010)	Davos, Switzerland	Slope	Crystal Growth	Surface hoar growth was best on cold clear nights with humid air and low to moderate winds. Surface hoar crystals tended to survive even when sublimation from the snow was occurring.
Lutz (2011)	West Yellowstone, MT	Slope	Layer Thickness, Shear Strength	Surface hoar weak layer heights were largest and shear strength was lowest in areas that exhibited larger unobstructed views of the sky and received lower amounts of radiation.
Shea (2011)	Columbia Mountains, BC	Slope	Crystal Size	Using sky visibility, positive correlations with crystal size and negative correlations with snow surface temperature were found.
Shea and Jamieson (2011)	Columbia Mountains, BC	Multiple Slopes	Crystal Size	Large amounts of solar radiation in the alpine were found to only cause a small decrease in crystal size.
Helbig and van Herwijnen (2012)	n/a	Mountain Range	Simulated Growth and Destruction	Using simulated topography, autocorrelation lengths for modeled surface hoar were on the order of several hundred meters. The distribution of surface hoar largely depended on solar elevation angles and topographic roughness.

Table 1 continued.

Reference	Location	Study Extent	Property	Relevant Observations
Borish (2012)	Chilkat and Takhinsha Mountains, AK	Mountain Range	Crystal Growth	Positive relationships with surface hoar size and elevation were found. Spatial autocorrelation ranges were similar in size to the study area basins.
Hendrikx et al. (2012)	Big Sky, MT	Mountain Range	Crystal Growth	Ideal surface hoar conditions were found with higher relative humidity and cooler temperatures. Aspect alone could not always explain the presence of surface hoar for a formation event.
Horton et al. (2014)	Columbia Mountains, BC	Mountain Range	Crystal Growth	Used numerical weather prediction models to predict surface hoar size. PSTs indicated that buried surface hoar layers showed the propensity to propagate for up to six weeks. Larger surface hoar crystals showed only weak correlations with instability.

3. METHODS

3.1 Study Area

This study was carried out at two study sites in the Taylor Fork area in southwest Montana, USA (Fig. 3). The Taylor Fork lies in the southern Madison Mountain Range approximately 50 km north of West Yellowstone, MT and 100 km south of Bozeman, MT. The area is located within the Custer Gallatin National Forest and includes portions of the Lee Metcalf Wilderness Unit. Access is by dirt road and singletrack trail during snow-free periods of the year. When the area is snow-covered, access is by snowshoes, cross-country skis, or snowmobile. The Taylor Fork is a popular winter snowmobile destination with motorized use prohibited from October 15 through December 1. A section of the Big Sky Snowmobile trail bisects the area and is groomed during the winter on a bi-weekly basis.

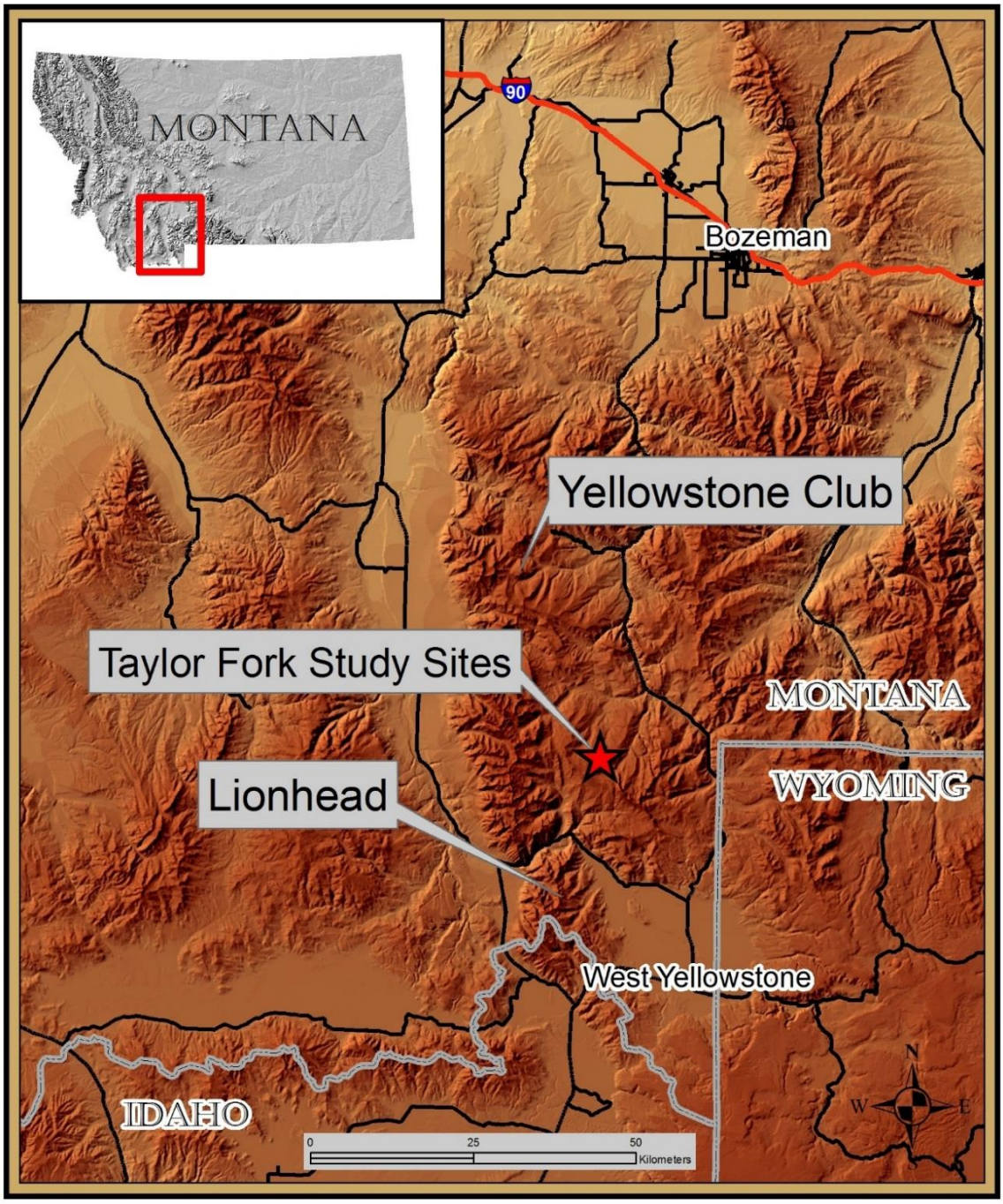


Figure 3. Southwestern Montana showing current and past surface hoar research locations including The Yellowstone Club (Adams et al., 2011; Slaughter, 2010, Hendrikx et al., 2012) and Lionhead (Landry, 2002; Logan, 2005; Lutz, 2009).

Low elevations (~2000 m) consist of mixed conifer forests with interspersed sagebrush and grassland meadows. Upper elevations (~2700 m) are mainly in the alpine and contain little forested area. The western portion is flanked by the Taylor-Hilgard Unit. The primary ridge of the Taylor-Hilgard Unit runs north-south and contains peaks in excess of 3000 m above sea level. These mountains form a large relief from the Madison Valley to the west and enhance orographic lifting for storms moving into the Taylor Fork from the west or north. The winter snow climate of the area is characterized as intermountain experiencing relatively cold winters (avg. temperature <7° C) with little rain (avg. rain <8 cm) and moderate snowfall (avg. snowfall >560 cm and avg. snow water equivalent (SWE) <100 cm) (Mock and Birkeland, 2000).

The Taylor Fork lies between two regions that have received extensive surface hoar research (Fig. 3). The Yellowstone Club, a private ski area situated on Pioneer Mountain near the town of Big Sky, MT, lies approximately 30 km to the north. Multiple sites on Pioneer Mountain have been the focus of surface hoar research (e.g. Adams et al., 2011; Cooperstein, 2008; Hendrikx et al., 2012). The Henry's Lake Mountains lie 25 km to the south. The area within this range to the north of Targhee Pass is commonly referred to as the Lionhead area and has been the focus of numerous studies regarding surface hoar (e.g. Landry, 2002; Birkeland et. al, 2004b; Logan, 2005; Lutz, 2009).

The Taylor Fork contains sparse automated meteorological instrumentation. Two Snow Telemetry (SNOTEL) sites provide hourly information on air temperature, snow depth, and SWE. These stations are the Carrot Basin SNOTEL (elevation of 2742 m and ~2 km west of the study sites) and the Beaver Creek SNOTEL (elevation of 2393 m and

~7 km west of the study sites). The stations have 30-year average median April 1 SWE amounts of 73 cm and 46 cm. The Taylor Fork weather station is an automated remote meteorological station measuring air temperature, relative humidity, wind speed, and wind direction and is erected each winter by the Gallatin National Forest Avalanche Center (GNFAC) near Pika Point at an elevation of 2883 m (Fig. 4). This automated station is accessible on GNFAC's website (www.mtavalanche.com) and provides hourly information updates. The next closest meteorological stations that measure temperature and relative humidity are the Hebgen Lake RAWS (~17 km to the south), Yellow Mule RAWS (~24 km to the north), and the Lionhead weather station (~25 km to the south).

3.2 Site Selection and Study Sites

I chose two study sites in the Taylor Fork for this study. The two sites, herein referred to as the North Site and South Site, are located in the western portion of the Taylor Fork (Fig. 4). Winter access to the sites is an 11-18 km journey via snowmobile along a groomed section of the Oil Well road after parking at either the Wapiti trailhead or, if the Taylor Fork road is impassable due to snow drifting, the Sage Creek parking lot near U.S. Highway 191. Each study site is further accessed by skiing down to the site or skinning through heavy timber.

I chose study sites that fit a number of criteria. Sites needed to be situated in an area that consistently produced surface hoar throughout the winter. A high likelihood of

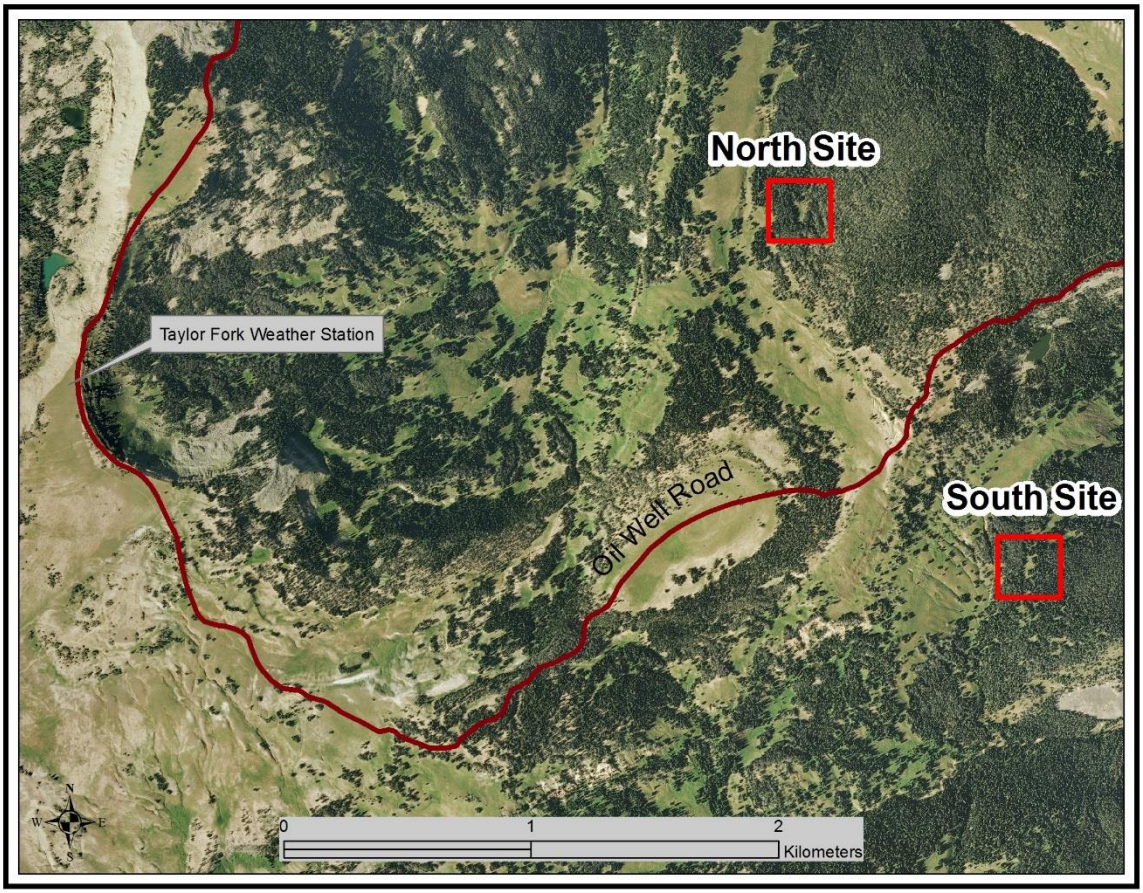


Figure 4. Study site and weather station locations in the Taylor Fork. The specific location of the Carrot Basin Snow Telemetry (SNOTEL) site is omitted to ensure the site remains undisturbed.

formation events was expected in this region as prior studies both to the north (e.g. Adams et al., 2011; Cooperstein, 2008; Hendrikx et al., 2012) and south (e.g. Landry, 2002; Birkeland et. al, 2004b; Lutz, 2009; Logan, 2005) achieved success studying surface hoar. Also, daily historical avalanche bulletins and conditions videos issued by the GNFAC for this region detail observations of surface hoar formation on the surface and numerous occurrences of problematic buried surface hoar layers.

I wanted to examine slopes with very different radiation balances and shading characteristics. As the largest difference in solar radiation occurs between north and south

aspects, I chose one northerly and one southerly facing slope to capture this disparity. Northerly aspects have seen spatial studies with buried surface hoar layers (e.g. Lutz, 2009) and surface crystals (e.g. Shea, 2010). While Cooperstein (2008) focused on northerly and southerly aspects with surface hoar that was not buried, no spatial analyses were conducted. A spatial study on a southern facing slope would help fill the limited knowledge on this aspect.

I also considered avalanching of the study slopes and potential avalanche hazard during access or sampling. Study sites were desired in areas free of potential avalanches that could alter site characteristics or produce an irregular surface from partial avalanching of the slope or avalanche debris running into the area. Avalanche hazard from surrounding areas was a concern as the field team would be exposed to hazards for upwards of 3 hours on each slope due lengthy sampling times. While slope angles conducive to avalanches are preferred for inferences to avalanche slopes, their use was not practical for this study. Minimizing exposure to avalanche hazard while accessing the sites was also needed. Site accessibility was required at all times during the winter regardless of avalanche hazard. Sites possessing safe ingress and egress routes were sought as a surface hoar event could occur with high or extreme avalanche danger.

Sheltered locations which receive ample snowfall to cover disturbances from prior field team visits were needed. This study planned to make multiple site visits during the winter and snowfall between visits reduces surface disturbances from field teams, animals, or winter recreationists. As most potential areas are very popular with snowmobiles and snowbikes, ideal locations would limit their access.

I chose planar slopes in an attempt to reduce the effects small undulations or disturbances have during surface hoar formation. Small differences in irregular slopes could lead to small, non-negligible differences in air temperatures, radiation, and wind patterns. A pooling of colder air in a depression or an increase in wind speed for small rise could potentially alter surface hoar growth.

I chose meadows of relatively similar sizes to reduce scaling effects when comparing meadows with different spatial extents. Similarly sized meadows also allow for sample sizes (discussed in section 3.3) to be similarly proportioned.

In December of 2013, I assessed multiple locations (including ones more easily accessed and closer to Bozeman) for their potential as study sites. While multiple areas north and south of the final study area harbored individual sites that were adequate for the study, very few areas exhibited two, close proximity meadows that fit all requirements. I ultimately chose two study sites in the Taylor Fork as they sufficiently met my criteria.

3.2.1 North Site

The North Site is a small meadow opening that lies near the head of Sunlight Basin to the north of the Oil Well Road (44° 58’ N, 111° 16’ W) (Fig. 5). The site is located on a small plateau which drains into Little Wapiti Creek. The site faces 358° grid bearing and lies at an elevation of 2690 m. It has a grass/rock groundcover and is surrounded by trees on all sides. The thick forest surrounding the site consists of living and standing dead subalpine fir and lodgepole pine. The average winter snow slope angle is 11°. The site is approximately 40 m cross-slope and 55 m down-slope with small

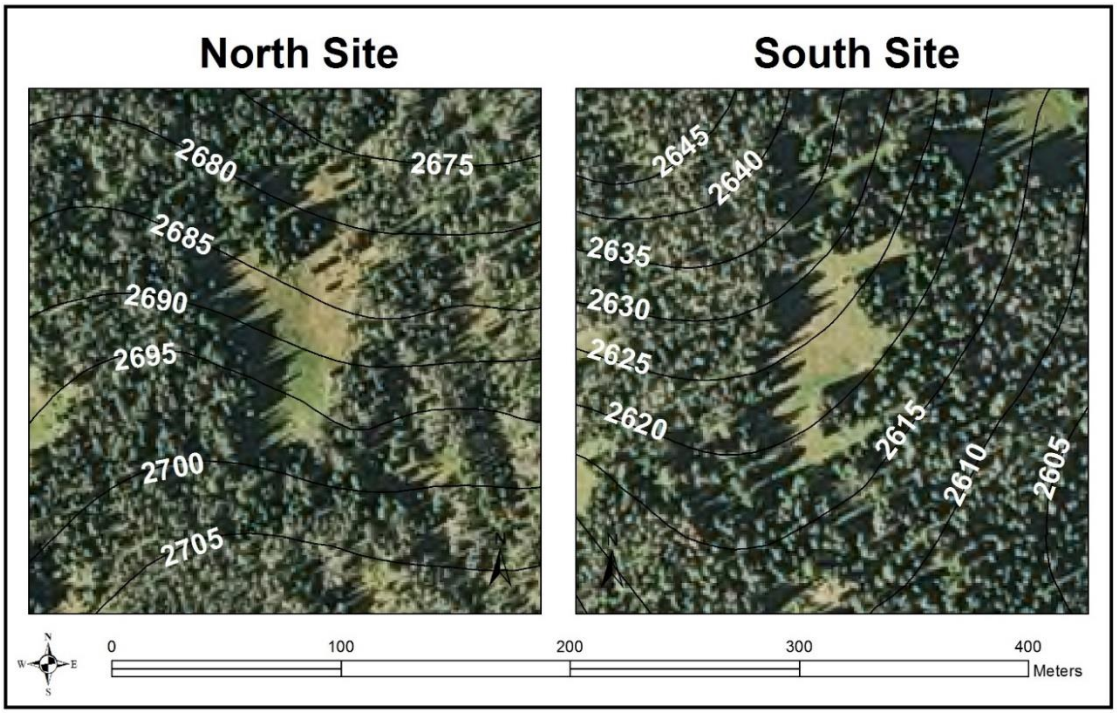


Figure 5. Aerial photograph of the two study sites with 5 m elevation contours.

openings extending slightly further on the northwest and northeast ends (Fig. 6). The site is located 1700 m to the northwest of the South Site.

I placed a HOBO Pro v2 datalogger connected to a temperature and relative humidity sensor in the center of the meadow in January of 2014 and December of 2015. The sensor is mounted inside a radiation shield and attached to a PVC pipe. I placed the sensor at a height of 1.6 m with an assumption that subsequent snowfall would change the sensor height closer to the 1.5 m standard prior to the next site visit.

3.2.2 South Site

The South Site is a small meadow opening in the Taylor Fork (Fig. 5). The site lies near the head of Sage Basin south of the Oil Well Road. The site faces 130° grid bearing and has an average winter snow slope angle of 10°. The meadow is bordered by



Figure 6. Looking down-slope from the southwest corner of the North Site.

living and standing dead lodgepole pine and subalpine fir trees. The site measures 45 m cross slope and 50 m down-slope. A small clearing in the trees is found in the upper east and lower west ends. I placed meteorological equipment in the center of the site similarly to that of the North Site (Fig. 7).



Figure 7. Looking south at the South Site. PVC conduit with attached meteorological equipment is visible in the center.

3.3 Sampling Design

I wanted to explore relationships between surface hoar size and environmental determinants, and analyze spatial patterns of surface hoar size across the two small meadow openings when surface hoar was on the surface directly after a period of growth. I gave considerable thought to the sampling designs of similar point snow sampling schemes in field studies to choose a design which produces the most reliable estimates with the least amount of bias.

Traditional snow sampling designs use gridded sampling schemes to produce measurement data for analysis (Kronholm and Birkeland, 2007). For snow sampling at the slope scale, these methods involve evenly spaced gridded layouts or gridded layouts with nested evenly spaced grids. Limits to estimations from these designs in snow studies has been due to the relatively low sample size and inability to incorporate randomness. For any slope-scale snow studies, the introduction of some randomness is recommended (Kronholm and Birkeland, 2007). To limit slope destruction and incorporate randomness, Shea and Jamieson (2010) proposed a sampling design that used random sample distances along a linear path in a star pattern. This design allows for repeated measurements from multiple site visits as slope destruction is limited.

Sampling designs must consider the scale triplet (Bloschl, 1999). Measurement spacings should be smaller than the true correlation length and the measurement extent should be larger than the true correlation length (Skoien and Bloschl, 2006). While optimal in theory, the true correlation length may not be known and although it may be found from other studies, scaling issues may still arise. The best recommended method

for reducing scaling issues is to incorporate a sampling design that has the largest amount of samples possible (Skoien and Bloschl, 2006).

I chose a gridded point sampling scheme with additional random point samples (Fig. 8). I set the maximum number of observations for each study site at 100. I

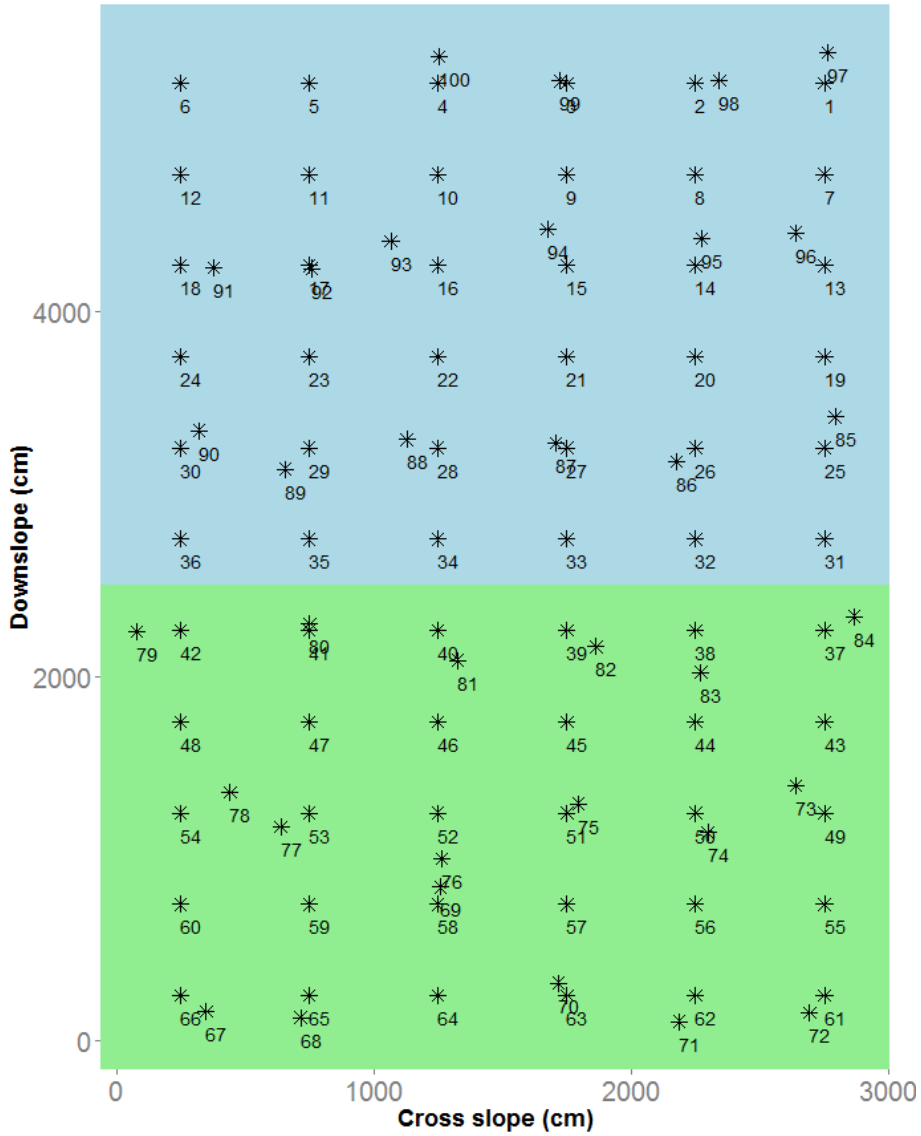


Figure 8. Example sampling layout. Observations are numbered in the order they were taken. Blue represents the north plot and green represents the south plot. Points numbered 1 through 66 are on a gridded layout and points 67 through 100 are based on random assignments.

considered this the largest practical number of observations that could be taken during a sampling day. Gridded sampling was conducted by sampling each meadow at 5 m spacings with the maximum sampling extent constrained by the bordering trees. I initiated gridded sampling by arbitrarily setting a starting point in the northeast corner of each meadow. I measured distances using metric reel tapes strung down-slope and cross-slope. Care was given to not disturb any surface hoar as the tapes were positioned. I sampled at each 5 m tape measure increment until reaching the maximum sampling extent. I then moved the cross-slope tape to the next 5 m increment on the down-slope tape and sampled using the same horizontal increments. In an attempt to achieve perpendicular measurement tapes for a consistent grid, I utilized a 3-4-5 right triangle each time the tape was moved. I continued this procedure until reaching the forest at the end of the down-slope tape.

I collected the remaining number of observations needed to achieve the maximum sample size using a random sampling scheme. I sampled points based on a random distance and random direction (from compass north) from selected original points (Fig. 9). A table made prior to sampling contained random distances ranging from 0 m to 2.5 m and random compass directions ranging from 0° to 360°. As the number of samples in the random sample portion was smaller than the gridded number of observations, I omitted full cross-slope rows.

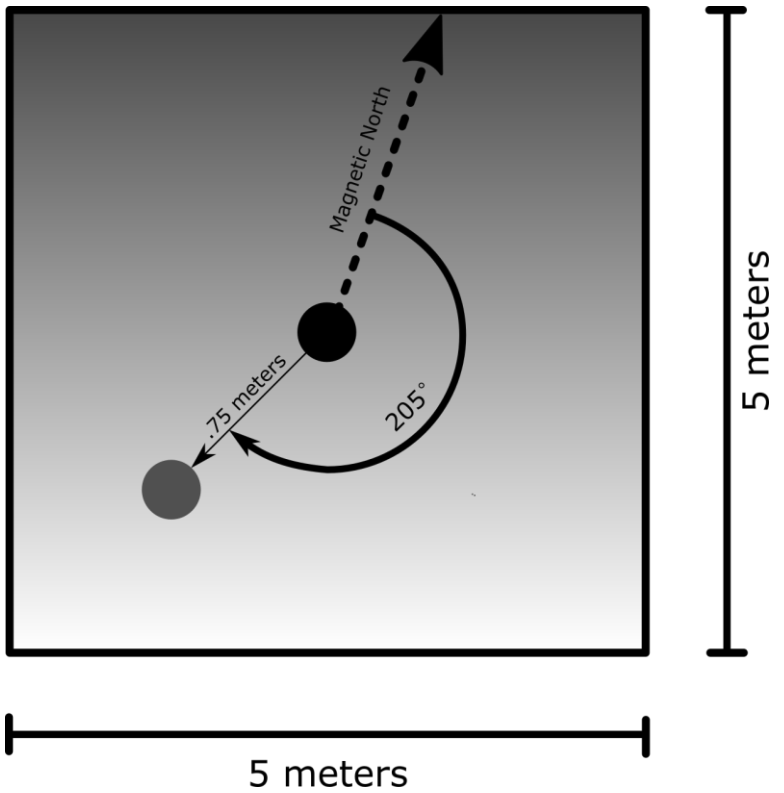


Figure 9. Diagram of the random sampling technique. The center black dot represents a gridded sample point and the lighter grey dot represents a randomly sampled point.

3.4 Data Collection

Field data collection occurred on January 25, 2014; April 04, 2014; and January 02, 2015 when surface hoar was noted on the surface at both study sites. These dates are referred to as Jan2014, April2014, and Jan2015.

I sampled the South Site first, followed by the North Site in an effort to reduce solar radiation influences on the surface hoar during a sampling day. At each sample point, I took an upward facing and level hemispheric fish-eye photograph with a Canon 8-15 mm fisheye lens set to an 8 mm focal length attached to a Canon EOS 5d Mark II full frame digital SLR camera. I positioned the camera height as low as possible without

capturing the field team in the photo. This distance varied between 40 cm and 50 cm. I leveled the camera using a camera mounted bubble-level and oriented the camera base to compass north. While optimally the camera's sensor orientation would be normal to the snow surface to allow for the most accurate sky visibility estimation, consistently achieving this was not practical. Also, a second image would be needed for any radiation estimations. I deemed the two image per point method too time intensive and chose not to utilize it.

At each sample point, I gathered surface hoar crystals onto a crystal card with a 1 mm and/or 2 mm grid spacing from a ~2 x 1 cm area and captured an image of the crystal card with crystals for later analysis (Fig. 10). I also measured slope angles at each point (over a 20 cm distance) with a Backcountry Access slope meter.



Figure 10. Digital camera and crystal card with a 2 mm grid used for crystal photography.

I followed synoptic weather charts during the two winter study seasons to forecast for a potential sampling day. Ideal weather conditions of below freezing temperatures, relatively high humidity (>60%), and clear or mostly clear nights were sought. I utilized several resources the night before and early morning of a potential sample day to examine a more detailed synopsis of forecasted and overnight conditions if ideal conditions were forecasted. These resources include:

- Referencing an online clear sky conditions forecast, based on data from the Canadian Meteorological Center and converted to graphical format by the website www.cleardarksky.com for the study area, in the evenings for an overnight sky conditions forecast.
- Examining a National Weather Service point forecast for temperature and relative humidity.
- Observing 04:00 sky conditions at several neighboring areas on a potential sample morning using observations in Bozeman and webcams in Big Sky and West Yellowstone.
- Assessing nearby remote weather stations at the Taylor Fork, The Yellowstone Club, Big Sky Resort, Lionhead, and Yellow Mule for ideal overnight meteorological conditions.

If a general consensus between observations showed the potential for overnight formation conditions (clear skies, below freezing temperatures, and relative humidity greater than 50%), I traveled to the sites for a conditions check.

A sampling day started with a 05:00 departure from Bozeman. I visited each site to check for surface hoar presence. After a confirmation of surface hoar at each site, I sampled the South Site starting at 07:30 and finished sampling the North Site around 15:30. Each study site required 2.5 to 3 hours to sample with additional time needed for access. On the April2014 sampling date, inclement weather during sampling of the South Site did not allow for crystal images due to breezy conditions. I measured crystal sizes manually with a 10x loupe and sized crystals to the nearest 0.5 mm following guidelines from *The International Classification of Seasonal Snow on the Ground* (Fierz et al., 2009). Also on this date, I abandoned sampling at the North Site due to snowfall that occurred at the site while sampling the South Site. New snowfall mixed with surface hoar crystals did not allow for useful interpretations of crystal size from crystal images.

3.5 Data Processing

3.5.1 Crystal Sizing

Once out of the field, I displayed crystal images on a computer monitor to examine and size crystals at an enhanced zoom. This process allowed for a more unbiased approach to crystal sizing as opposed to field sizing while allowing for faster sampling and therefore larger sample sizes. Crystals recovered from the field and preserved in an iso-octane mixture have used similar lab sizing approaches (e.g. Cooperstein, 2008). While this method allows for sizing crystals in a controlled environment, the use of subfreezing liquid iso-octane to transport crystals was not

feasible with my large sample sizes and probable crystal destruction during snowmobile transport.

I sized each crystal on a crystal card image to the nearest 0.5 mm measured at the crystal's longest extension (Colbeck et al., 2009) (Fig. 11). I only sized easily identifiable surface hoar crystals. Similar to Stossel et al. (2010), I found crystal sizes occasionally varying widely within a sample. Several crystal cards exhibited surface hoar crystal size ranges up to 10 mm.

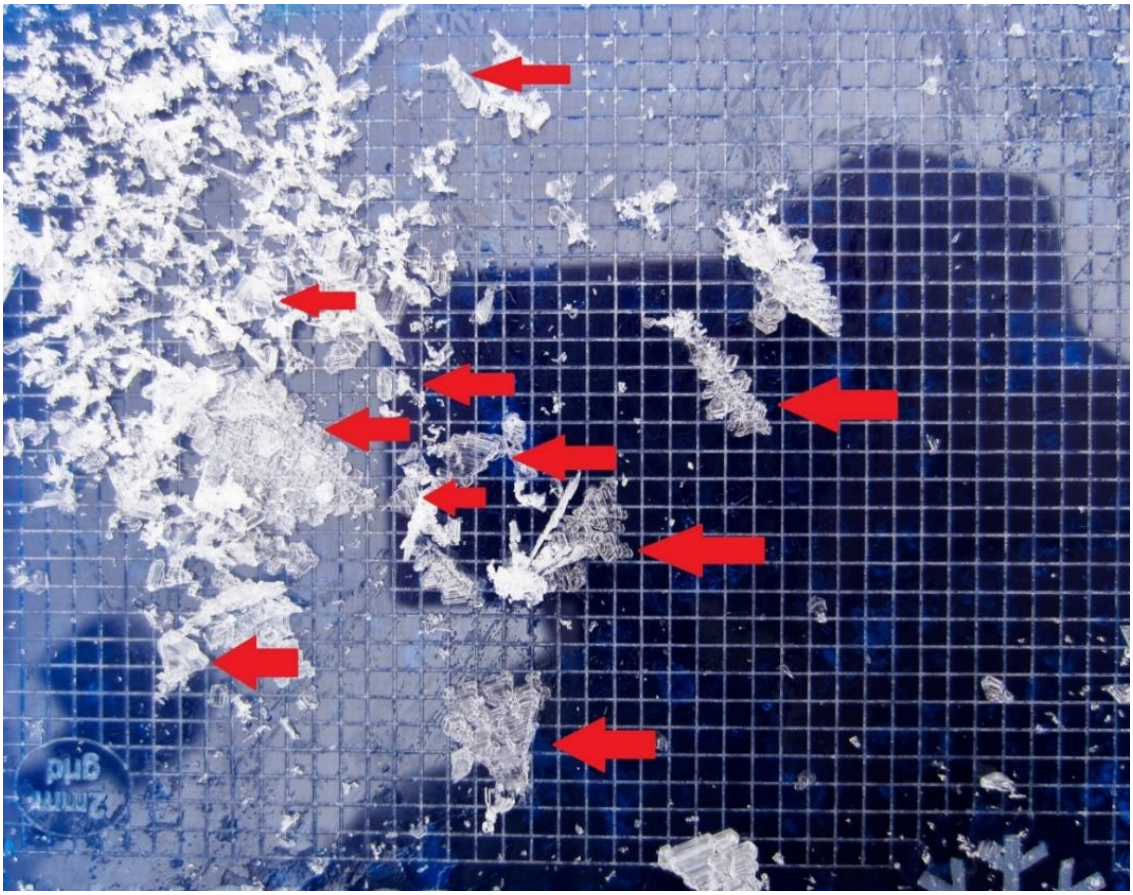


Figure 11. Example crystal card image with red arrows indicating sized surface hoar crystals.

3.5.2 Hemispheric Photography

I made preliminary hemispheric image adjustments in Adobe Lightroom to correct unsatisfactory exposures and remove any chromatic aberrations along defined edges. I exported RAW format images in JPEG format for thresholding. Upon inspection, I determined 38 images from the North Site from the Jan2014 event could not be used due to a small focal length shift and one image from the South Site was mistakenly not taken.

I thresholded images using the image processing program SideLook which allowed for automatic image thresholding (Nobis, 2005). This process required no manual interactive interpretation which allowed for a more straightforward and reproducible conversion to black and white than alternative methods (Nobis and Hunziker, 2005). Sidelook also permits the use of a single split RGB channel for thresholding. Under cloudy conditions, the distinction of white sky from green canopy is relatively easy. With a clear sky, the distinction between green canopy and blue sky is difficult. I used a single blue channel for thresholding which allowed for easier and more accurate image conversion. Images from all sampling dates benefitted from this technique due to variable cloud and sky conditions.

With the choice of leveling the sensor plane during image capture, a small sliver of snow is evident in all images (Fig. 12). I manually colored this small portion black and considered the area canopy (Fig. 12). This seems reasonable as the area would be considered mostly canopy had the image been taken slope normal and follows methods similar to Lutz (2009). I exported thresholded images in BMP format for further analysis.

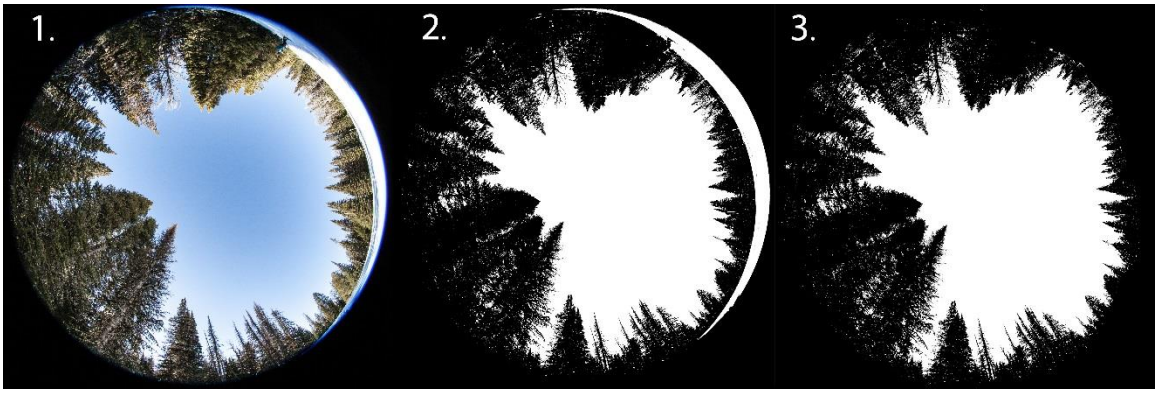


Figure 12. Example hemispherical images. (1) Image directly from camera with no processing. (2) Image that has been thresholded. (3) Image after thresholding and manual filling of the visible snow surface.

I encountered problems with thresholding when snow covered portions of the canopy from prior winter storms for the April2014 and Jan2015 sample dates. Automatic and manual thresholding tended to classify canopy snow as white which coded these as 'sky' and resulted in inaccurate canopy estimates. Manual filling of these snow (white) areas to a canopy (black) designation is possible but was not feasible due to the large amount of images and fine pixel detail of the snow. I chose an alternative method of thresholding for these images. Using Adobe Photoshop, I selected the sky region (excluding gaps in the canopy) and filled the area with solid green (r=0, g=255, b=0) (Fig. 13). This allowed for the separation of sky from canopy snow. I thresholded images using automatic methods in Sidelook and the green RGB channel. I subtracted the new estimates from the original thresholded image estimates and used these in analysis. While this method may slightly underestimate all values due to the exclusion of small canopy gaps in trees, I deemed this alternative more appropriate than allowing snow cover to be considered sky.

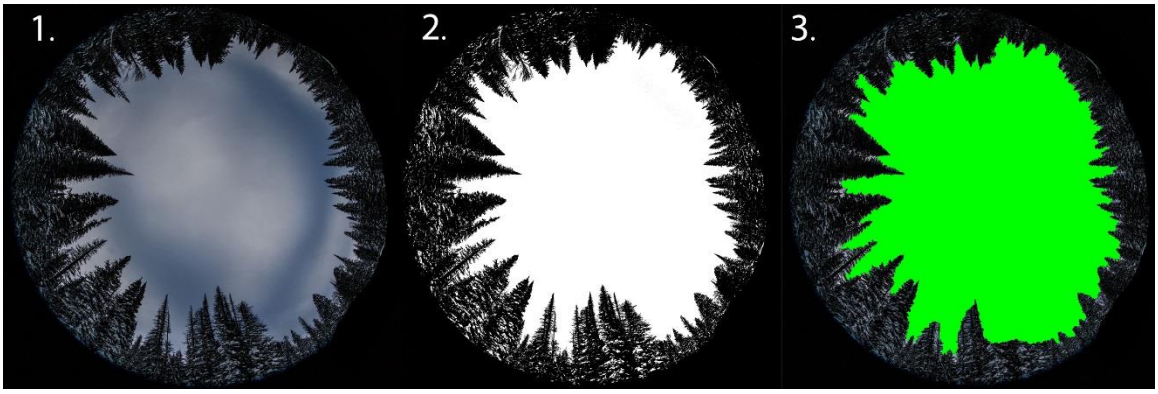


Figure 13. Example images for thresholding when snow is present in the canopy. (1) Preprocessed image showing snow covering trees. (2) Thresholded image showing portions of trees where snow is present counted as sky. (3) Alternate technique showing sky portions filled with solid green.

I calculated the sky visibility, shortwave radiation from the day prior to sampling, and sunfleck duration from the day prior to sampling for each sample point using the thresholded images and Gap Light Analyzer (GLA). These derived measures are referred to as ψ_{Sky}, $\Sigma_{Sunfleck}$, and $\Sigma_{Sunfleck}$. GLA is a hemispheric image analysis program (Frazer et al., 1999). It estimates ψ_{Sky}, $\Sigma_{Sunfleck}$, $\Sigma_{Sunfleck}$, and many other measures using thresholded hemispheric images.

Prior to processing images, I set an initial configuration for each sampled date. This configuration includes: a projection distortion file, magnetic correction information, site location information, solar time step setup, a radiation configuration, and a sky region setting. I set site location information, such as elevation and location, for each study site. The solar time step was set at the lowest possible increment of one minute. I divided sky regions into 50 azimuthal regions and 10 zenith regions which yielded 500 individual regions. After image import into GLA, I defined the circular image area and set the initial

cursor point to magnetic north. I set this configuration for an initial test image, saved the information for subsequent image analysis, and ran calculations on all images.

I estimated total shortwave solar radiation for the day prior to surface hoar formation using the internal solar radiation program in GLA as no meteorological devices measured radiation at the field sites. While these estimates of shortwave radiation should only be considered relative estimates across a site, care was given to the input parameters to produce reasonable estimates based on recommendations from Frazer et al. (1999). I set values for the radiation calculator as: solar constant of 1367 Wm^{-2}, spectral fraction of 1.0, cloudiness index of 0.85, and beam fraction of 0.9 (Frazer et al., 1999)

GLA uses a sun tracking algorithm that calculates the sun's movement across a hemispheric image (Fig. 14). The program uses the initial north point and image date to produce an estimate of the sun track across the sky. This information is used along with a thresholded image to compute when a specific point receives direct beam solar radiation. This track is used for the calculation of direct beam radiation at the sample point. Diffuse radiation is calculated and added to the direct beam radiation for an estimate of total radiation for the time step. Final values for total shortwave are the sum of the one minute time step solar radiation calculations for the full day prior to surface hoar formation with units of MJm^{-2}.

While computing direct beam radiation, total sunfleck duration is summed to determine the time a point on the ground receives direct beam radiation (Frazer et al., 1999). Total sunfleck duration can be thought of as shading. The lower the sunfleck duration, the more shaded the area.



Figure 14. Hemispheric image with GLA estimated sun track (yellow line).

3.5.3 Camera Calibration

To produce the most accurate environmental estimates with GLA, I performed several camera checks and calibrations. GLA processes images that are taken with focal lengths at or less than 8 mm and possess a full 180° field of view (FOV) (Frazer et al., 1999). I assessed the FOV for the study's fisheye lens using a total station to measure the total angular FOV. I measured several instances of a 180.5° FOV and deemed this sufficient for use in GLA.

The projection distortion of the lens used for image capture must be known for GLA calculations. Documentation for the Canon lens did not specify a radial lens distortion and research has shown that manufacturer specifications are not always accurate (Herbert, 1987). I used a combination of techniques outlined by Frazer et al.

(2001) and Lutz (2009) to quantify a user-based designation of radial distortion for this lens.

For indoor calibration, I marked successive equally spaced lines on a wall and captured an upward facing and level fisheye photograph (Fig. 15). Using measured distances from the camera to the ceiling and wall along with known spacings between the marked lines, I established radial angles using trigonometry. I measured distances (in pixels) between marks using Adobe Photoshop and tabulated all results.

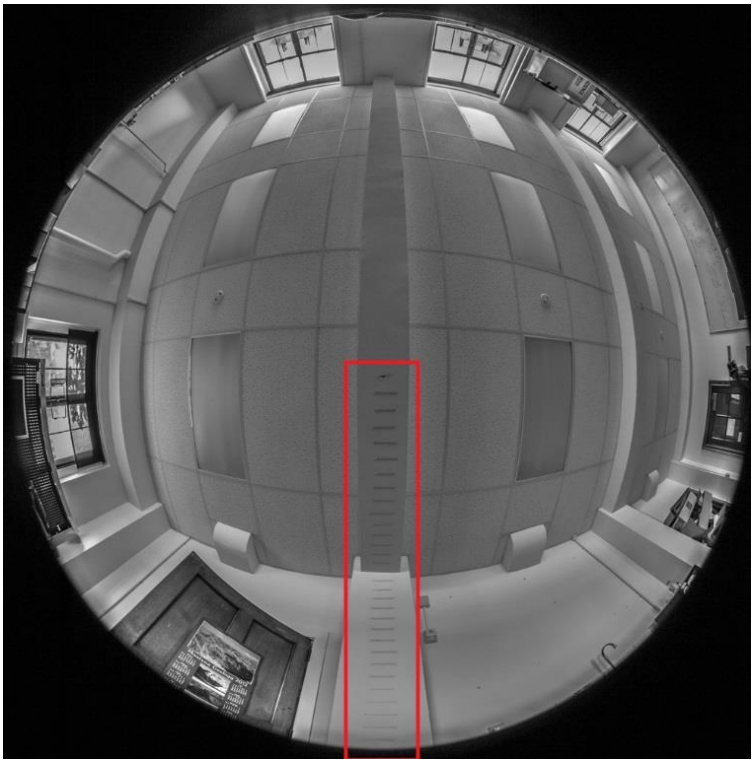


Figure 15. Office calibration of the fisheye lens. The red box outlines reference marks used for distance and angular measurements.

I completed a second calibration using a tall outdoor building with easily identifiable and regularly spaced features that could be measured by sighting (Fig. 16). I



Figure 16. Field calibration of the fisheye lens. Red arrow shows the position of a 44° and 54° radial angle at two horizontal distances from the building.

used a Suunto clinometer (accuracy +/- 1° (Suunto, 2015)) to measure radial angles from two camera positions near a building. I took ten angular measurements to known features with the camera placed 10 m and 15 m from the building. Pixel distances in images were counted similar to the last calibration. I combined radial angles and pixel distances from each calibration setup and placed this information into a camera calibration file to define a projection distortion in GLA (Appendix E).

3.6 Data Analysis

I placed field and derived image data into tabular format. All data was linked to a Cartesian coordinate system unique to each sampling date and site. I split each site into a subplot (e.g. north plot and south plot) to explore trends in up-slope and down-slope areas

in regression analyses (Fig. 8). Splitting the site into sub-plots also allows for the differentiation of results from areas near highly solar affected trees, and ones near shaded trees.

3.6.1 Response Variables

By counting each individually identifiable crystal for a sample, a suitable response variable or variables were needed to perform statistical analyses. The choosing of a response variable(s) was not straightforward as prior surface hoar studies have used differing methods of obtaining a crystal size and differing crystal size descriptive statistics to analyze their data (see section 2.7).

This study benefits from the ability to calculate a number of descriptive statistics to characterize surface hoar size at a point. With many possible summary measures to choose from, I chose sizing measures similar to ones used in prior surface hoar studies. These summary measures are the sample mean crystal size, the 90th percentile crystal size, and the maximum crystal size for each sample point. These are further referred to as $Size_{Mean}$, $Size_{90th}$, and $Size_{Max}$ for the Jan2014 and Jan2015 sampling dates. I chose the sample mean based on prior surface hoar studies (e.g. Shea, 2010; Borish et al., 2012) (Table 1) and its use in defining a buried layer's crystal size (Fierz, 2007). I derived a sample mean using all crystals sized from a single crystal card image. I chose the 90th percentile as an alternative to using the mean maximum crystal size. The 90th percentile is the number below which 90 percent of the observations may be found. This seems a reasonable measure as it removes any user bias from the estimation of a mean maximum size and was easily derived. I included maximum crystal size due to its prevalence in

prior studies and how well it has been shown to represent layer thickness once buried (Chalmers et al., 2001). During sampling, I observed multiple occurrences when the maximum crystal size would be noticeably larger than any other crystal from the sample. These large crystals were often sporadically observed throughout the sample area and may not have accurately represented any surrounding crystals. This finding further supported the choice of including the 90^{th} percentile size.

On the April2014 sample day, I was not able to take crystal images and no descriptive statistics were calculated. While in the field, I decided to manually size crystals using the average of the longest crystal extension at each sample point. This measure follows other studies and is comparable to the 90^{th} percentile used for other sample days. This measure is furthered referred to as $Size_{Actual}$.

The use of three crystal size summary measures in my analysis is unique. While prior studies simply chose a single sizing measure, I did not want to limit my analysis to a single crystal size measure such as maximum or mean size. I also wanted to reduce bias that may be present in other studies when crystals are sized solely in the field. To illustrate discrepancies in crystal sizing for field studies, I took a sample of convenience of individuals attending the 2014 International Snow Science Workshop poster session in Banff, AB. I asked 13 individuals to examine a crystal photograph that I used in this study and determine the size they would record in their field notebook. Summary crystal sizes given by the sampled individuals are recorded as a single number or a range (Table 2). Sizes range from 2 mm to 6 mm. Based on the same photograph, the size measures used in this study are: 3 mm for $Size_{Mean}$, 4.6 mm for $Size_{90th}$, and 6 mm for $Size_{Max}$.

Combining all observer's sizes yields size measures of: 4 mm for $Size_{Mean}$, 4.9 mm for $Size_{90th}$, and 5 mm for $Size_{Max}$. While no person is necessarily wrong, it does illustrate that using a single size measure for a study may produce differing results depending on the observer, how the crystals are sized, or how the measure is summarized. The use of crystal photography aids in crystal sizing as multiple observers can objectively size crystals and re-analyze crystal images at a later date.

Table 2. Surface hoar crystal size recorded by individuals at the International Snow Science Workshop.

Crystal Size (mm)
3-5
4
5
4-6
4
3
3
4
4-5
4-5
2-6
3-5
3-5

3.6.2 Data Exploration

Initial data exploration involved assessing relationships between surface hoar size measures and environmental determinants using scatterplots and correlation analysis in R statistical software (R Core Team, 2013). I created scatterplots for each summary measure and environmental determinant to assess for trends. I also conducted correlation analysis using the non-parametric Spearman's rank-order correlation test. This test is a

measure of statistical dependence between two variables. I tested for significance in the Spearman rank-order correlation test using a two tailed distribution from a studentized t-test based on sample size with $\alpha=0.05$ (Zar, 1972).

3.6.3 Linear Regression Analysis

To explore relationships between the chosen surface hoar size summary measures and the derived environmental determinants, I employed several regression approaches. Differing forms of regression analysis have been applied in surface hoar research (e.g. Lutz, 2009; Shea and Jamieson, 2010b, Schweizer and Kronholm, 2008; Borish et al., 2012). I chose ordinary least squares (OLS) regression for initial analysis as the prior studies have used linear type models for their analysis. Assumptions of OLS regression are: linearity in the model coefficients of the predictor with an error term; the error term is normally distributed; the model is exogenous, homoscedastic, and no serial correlation is present. If serial correlation is present in the data, other methods should be used to attempt to correct for this to produce unbiased estimates (Schabenberger and Gotway, 2005).

Serial correlation occurs across a distance or over time. Spatial autocorrelation is the effect that variables at locations are related to one another (Schabenberger and Gotway, 2005). OLS regression assumes all observations are independent and failing to account for spatial autocorrelation in a regression model may foster unprecise estimators. Predicted p-values and coefficient estimates may be in error resulting in incorrect inferences. Modelling a spatial correlation structure into a regression model with an error

term allows for more unbiased p-value and regression coefficient estimates along with a reduction in associated errors (Schabenberger and Gotway, 2005).

I created regression models using each surface hoar size measure ($Size_{Mean}$, $Size_{90th}$, and $Size_{Max}$) and each environmental determinant (ψ_{Sky}, $\Sigma_{Sunfleck}$, and $\Sigma_{Shortwave}$). Each model was visually and statistically checked for OLS assumptions. Using q-q plots, I assessed normality. I assessed for homoscedacity by examining plots of residuals against fitted values. If a model exhibited strong departures from assumptions, I deemed it unreliable and abandoned its use.

I tested the residuals from each OLS regression model for spatial autocorrelation using Moran's I (Moran, 1950). This test assesses for spatial autocorrelation within the residuals of a regression model. By testing the residuals for spatial autocorrelation, any spatial variations not accounted for in the model are found (Schabenberger and Gotway, 2005). If significant clustering was present in the residuals from the Moran's I test (p-value ≤ 0.05), I abandoned the OLS model and fit several spatial models to account for the autocorrelation.

I used two simultaneous autogressive (SAR) models in an attempt to account for any significant spatial autocorrelation in a model. The first SAR model is a spatial lag model. This model structure uses the assumption that the correlation process occurs only in the response variable (Dormann et al., 2007). Simply stated, this model takes into account the knowledge that surface hoar size at one location is associated with surface hoar size at other nearby locations. This association (based on distances or 'lags') is used in the regression equation for the controlling of autocorrelation effects. The second SAR

model is a spatial error model. This model assumes the autocorrelation is strictly in the error term of the model and not in the explanatory or predictor variables (Plant, 2012). This model uses the autocorrelation in the error term to introduce the correlation effects. The autocorrelation effect is introduced into both models using neighborhood matrices (Dormann et al., 2007). After accounting for any spatial autocorrelation, model coefficients were considered significant using p-value ≤ 0.05. More detailed explanations of the SAR models are found in Schabenberger and Gotway (2005) and Plant (2012).

I also conducted data exploration using multiple regression. I created initial OLS models using each derived response variable for surface hoar size with the derived environmental determinants. Due to $\Sigma_{Sunfleck}$ and $\Sigma_{Shortwave}$ exhibiting high correlation, I tested each variable separately within a model to explore individual effects. I examined and tested initial multiple OLS regression models for departures from assumptions similar to the other regression analysis. I fit spatial models if spatial autocorrelation was found with the Moran's I test. With multiple separate tests in a multiple regression model, alpha inflation may become problematic if effects are found when none are actually present. This inflation increases the Type I error rate (Salkind, 2010). I applied a Bonferonni correction to the alpha value for each multiple regression test to account for any alpha inflation.

3.6.4 Regression Trees

To offer alternative methods for data exploration, I applied a regression tree approach. This approach is used as assumptions for this type of analysis are less restrictive than those of linear regression and results are more easily interpreted.

Regression tree analysis does not assume a linear relationship between variables while also allowing the simultaneous use of parameters that exhibit multi-collinearity. They are robust to outliers in the data and allow for automatic stepwise selection. Regression trees have been used for snow and avalanche studies for both data exploration (e.g. Davis and Elder, 1994; Davis et al., 1999) and prediction (e.g. Rosenthal et al., 2002; Hendrikx et al., 2005). The use of regression trees for data exploration may produce models that examine relationships at the process level (Davis et al., 1999).

Regression trees are built through a process of recursive partitioning. Recursive partitioning (also referred to as classification and regression tree (CART)) analysis uses an algorithmic approach to split a homogenous dataset of independent variables into two smaller datasets based on a predictor variable (Breiman et al., 1984). The approach tests all explanatory variables in the dataset and determines the split which best separates the high response values from the low response values while minimizing the sum of squared deviations from the mean response of each smaller dataset. The sum of squared deviations in regression trees is referred to as the resubstitution estimate of the relative error. After splitting data into two subsets (nodes), the process continues until a stopping criterion is met. Once stopped, the subsets of data are referred to as terminal nodes.

While regression trees are typically used to handle large and complex datasets, their use with smaller datasets is limited. Larger datasets allow for sample sizes to remain relatively large after splitting whereas smaller datasets rapidly decrease in size. Hawkins (1999) suggests, “as a rough guide”, a minimum initial sample size of 100 should be used for regression trees.

Initial regression tree growth produces trees that are highly accurate but may be carried out beyond what the data warrant, are overly complex, and the lowest data splits may be based on very little information (Breiman et al., 1984). Trees that are initially grown too small may not use all the available information (Breiman et al., 1984). To produce an optimal tree, it is recommended to grow a tree that is much too large and prune the tree back towards the parent node. The pruning process uses the complexity parameter (cp) which is a measure of the resubstitution estimate and the complexity of the tree. A cp is reduced for trees that minimize the resubstitution estimate but is increased for trees that are overly complex (large number of terminal nodes). The cp value is computed by the process of 10-fold cross validation. The entire dataset is divided into 10 subsets of data and for each subset, a regression tree is grown and the error rates for each subset are combined. A 1-standard error rule is recommended for choosing the simplest tree whose error is no more than one standard error of the best model (Brieman et al., 1984). The best tree size is chosen by plotting the cp value vs. the x-val relative error and selecting the simplest tree that is within one standard error.

Overfit regression trees are typically used with data exploration and may uncover odd or rarely observed relationships (Davis et al., 1999). Pruning trees, using a stopping rule or cross-validation, is generally used for predictive purposes as the result is more statistically defensible (Davis et al., 1999). While my research focuses on data exploration, its goal is also in descriptive modeling which assists in driving a conceptual model.

Descriptive modeling is the capturing of associations between a dependent and independent variable (Shmueli, 1999). This modeling is different than explanatory modeling (finding causal relationships) or predictive modeling (predicting new observations) (Shmueli, 1999). While there are distinct differences between these model types, each model possesses qualities of the others. The use of overfit or pruned regression trees for descriptive modeling is not well defined. The complexity of an overfit tree does not lend well to providing easily understood relationships, but overfit trees may be extended to a point that is beyond what the data warrant (Breiman et al., 1984). Pruning a regression tree makes for a statistically defensible model that can be used for prediction but may not capture the complex underlying processes. While a middle ground, somewhere in between these two methods seems ideal, any basis for this is lacking. Therefore, in order to not extend the regression trees beyond what the data warrant, pruned regression trees using the 1-standard error rule are used in this study for explaining relationships and constructing a conceptual model.

I grew and pruned regression trees using the rpart package in R (Therneau and Atkinson, 2014). I grew initial ‘overfit’ regression trees using the surface hoar size measures and environmental determinants. Initial regression tree growth for avalanche studies have used a stopping criterion based on a minimum number of observations in the terminal node (e.g. Davis et al., 1999). However, the number used for that study is as large as my sample sizes. Without a more general guideline, I used a stopping criterion of five observations in a terminal node as recommended by Brieman et al. (1984). I pruned

each tree using a cp value that was within one standard error after 10-fold cross validation.

It is important to note that for all data analysis, my goal is on exploration of the data, capturing associations between the dependent and independent variables, and for the use of results in driving a conceptual model that is useful while in the field. My analysis is not intended for numerical prediction of surface hoar size for future events. Even if prediction of surface hoar size was the goal, its usefulness in the field is extremely limited due to complexities of gaining model input parameters and running the model for a given day. Also, as each event produces differing size ranges, only relative measures are appropriate. Thus, all analysis methods are used for data exploration, descriptive modeling, and driving a conceptual model and not for any future numerical predictions. Also, no single analysis method is relied upon to produce conclusions. Consistency across results utilizing differing analysis methods leads to stronger evidence for any inferences.

3.6.5 Spatial Analysis

Snow and avalanche studies are often concerned with snow properties over a given area and not just a single point (Schweizer et al., 2008). The variability of these snowpack properties is present at a large number of spatial scales ranging from individual snow crystal bonds to entire mountain ranges (Schweizer and Kronhom, 2007). Geostatistical analysis in avalanche research is a common tool to analyze the spatial properties of snow crystals, weak layers, and stability tests (Schweizer et al., 2008). Prior research focuses on a variety of scales which include the slope scale (e.g. Chernouss,

1995; Stewart, 2002; Kronholm, 2004a; Logan, 2005; Lutz, 2009) up to the range scale (e.g Helbig and van Herwijnen, 2012; Borish, 2012). A common tool for evaluating spatial properties in snow and avalanche studies are variograms.

A variogram is a plot of the average variance between points in a given field (Cressie, 1993). It is a useful measure in examining how spatial data is correlated over distances. A variogram is constructed using the equation:

$$2\gamma(h) = \frac{1}{N(h)}\sum_{N(h)}(Zs_i - Zs_j)^2 \quad (1)$$

where Zs_i and Zs_j are the values at two distinct points separated by a distance *h*. N(*h*) is the number of paired points at the distance *h* (Cressie, 1993).

A semi-variogram is typically used in place of the variogram and is a plot based on one half the average of the squared distances (Fig. 17). The semi-variogram is typically all that is needed for kriging or modeling (Cressie, 1993). The semi-variogram equation takes the form:

$$\gamma(h) = \frac{1}{2N(h)}\sum_{N(h)}(Zs_i - Zs_j)^2 \quad (2)$$

A robust method for semi-variogram calculations that better handles potential negative effects caused by the contamination of outliers is suggested by Cressie (1993) and takes the form:

$$\gamma(h) = \frac{\left\{\frac{1}{|2N(h)|}\sum_{N(h)}\left|Zs_i - Zs_j\right|^{\frac{1}{2}}\right\}^4}{2\left(0.457 + \frac{0.494}{|2N(h)|}\right)} \quad (3)$$

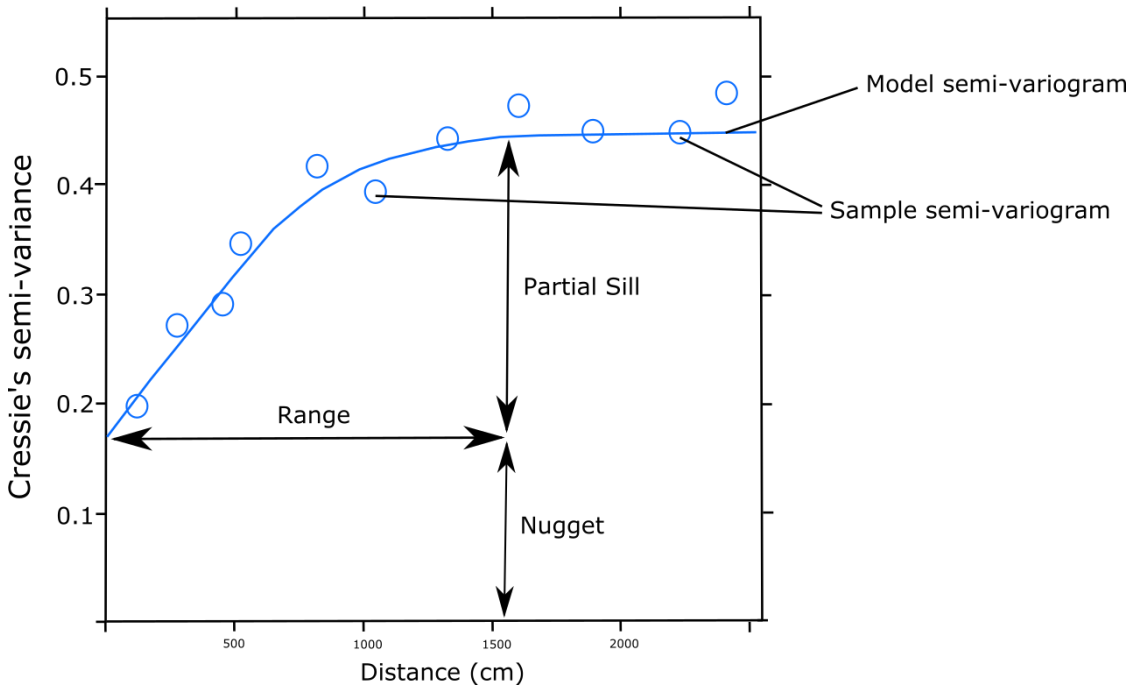


Figure 17. Example of a semi-variogram and a fitted semi-variogram model with descriptive parameters.

The terms variogram and semi-variogram have often been used interchangeably and inappropriately in many studies (Cressie, 1993). All calculations and references for this paper are to the semi-variogram and Cressie's robust semi-variogram in equation (3). I chose the robust semi-variogram due to the presence of outliers in my data.

As stationarity (the measured variables have a constant mean over the sample area) of the data is an assumption for semi-variogram creation, tests for trends in the data must be examined and corrected prior to semi-variogram creation. Webster and Oliver (2001) recommend testing for linear trends using geographic coordinates in a regression. If significant trends are found in the cross-slope (x-coordinate), up-slope/down-slope (y-coordinate), or both, these trends are removed to produce a detrended dataset for the semi-variogram estimation. Kronholm (2004) tested for linear trends using a robust

modified maximum likelihood regression method due to the presence of outliers in the data. I examined all datasets for significant trends in the up-slope and cross-slope directions using the lmRob function in the robust package in R (Wang et al., 2014). I chose this package as it more effectively handles outliers in the data. If a significant trend was found, I detrended the data for semi-variogram calculations.

When calculating a semi-variogram, distances between points are binned with individual bins being grouped based on the number of samples per bin or a length of observation (Schabenberger and Gotway, 2005). Bins with a minimum number of 30 point-pair combinations are recommended as the minimum needed in semi-variogram creation (Journel and Juijbregts, 1978). The choice of a bin length affects the semi-variogram cloud and bin lengths should be chosen based on fitting the data and not on the resulting semi-variogram fitting a chosen model (Schabenberger and Gotway, 2005).

Once a semi-variogram is plotted, a semi-variogram model is fit that allows for the comparison of spatial structures from the extraction of three relevant parameters (Fig. 17). Semi-variogram models attempt to fit a continuous function to the data to describe the data at unsampled locations (Webster and Oliver, 2001). There are a large number of semi-variogram models that may be fit to the data (e.g. Gaussian, Spherical, Nugget, Linear or Exponential). The goal is to “fit the simplest model that makes sense” (Webster and Olvier, 2001). Multiple models can be fit to a dataset and tested to determine the best model fit (smallest residual sum of squares). Similar to the goals of Kronholm (2004), I wanted to be able to compare the spatial structures from multiple datasets. I chose a spherical model due to its prevalence in surface hoar studies (e.g. Kronholm, 2004;

Borish et al., 2012; Shea, 2011), the bounded variation that is achieved, and this model was found to have the lowest residual sum of squares for many semi-variograms in preliminary analysis.

Once a semi-variogram model is fit, three values are often extracted. The first is the nugget effect or nugget when speaking of the actual value. There is evidence of a nugget effect when a semi-variogram does not pass through the plot origin (0,0) (Fig. 17). A nugget effect occurs when the sample design spacing is not small enough to adequately capture the underlying process or with the presence of measurement error (Schabenberger and Gotway, 2005; Bloschl, 1999). The second value is the sill and is measured on the y-axis. The sill is the upper bound of the semi-variogram and is measured from where the semi-variogram flattens. The partial sill is measured from the nugget to the point at which the semi-variogram flattens (Fig. 17). The semi-variogram range is the distance where the semi-variogram reaches the sill or in the asymptotic case, when the range achieves 95% of the sill (Schabenberger and Gotway, 2005) (Fig. 17). This distance is an estimate of where observations in the sampled area no longer show correlation with one another. The range is often referred to as the correlation length or integral scale and is of the most interest for this study (Bloschl, 1999).

I created sample omnidirectional semi-variograms and attempted to fit spherical models with the interest of finding correlation lengths. I created semi-variograms using the gstat package in R (Pebesma, 2004). I did not calculate semi-variograms at the subplot level as the minimum number of samples was below the recommended 100 samples needed for semi-variogram creation (Webster and Oliver, 2001). I used a lag

distance of one-half the maximum separation distance between points as recommended by Schabenberger and Gotway (2005). For most plots, this distance was near 25 m and was chosen for analysis. As this study uses 5 m grid spacing, the random point samples needed to fill a bin length that is less than 5 m to not create an overly large initial bin and also to capture any variability at distances less than 5 m. I examined multiple bin lengths that allowed for a common bin length which worked for all datasets. I chose a bin length of 0.25 m as this was the smallest number that created adequate bin sizes for most plots while still attempting to capture any smaller scale (<5 m) trends. I fit spherical models to semi-variograms that exhibited a reasonable spherical structure using a least squares method. I extracted and tabulated model measures of the nugget, sill, and range for fitted models.

4. RESULTS

I examine three surface hoar formation events that occurred during the winters of 2013-2014 and 2014-2015 at two study plots in southwest Montana. Data collected from these events is analyzed using the previously discussed methods and important results are presented and discussed in the following chapters. Conditions for attempted, but unsuccessful, sampling days are explored to illustrate the difficult nature of event prediction. A brief introduction and synopsis of the proceeding weather and avalanche conditions for each event is given to familiarize the reader with the conditions that precede each surface hoar formation event. Conditions during the probable formation period of each event are also qualitatively examined.

4.1 Attempted Sample Days

Over the course of two winters, I attempted thirteen study area visits when favorable meteorological conditions were forecasted. On many of these visits, I noted an absence of surface hoar at both study sites. Site visits for potential surface hoar days did not start until mid-January of 2014 as study sites were yet to be identified due to a lack of early season snow. After establishing study sites, eight potential surface hoar days were identified for the 2013-2014 season and five for the 2014-2015 season. Surface hoar was only found at the study sites for three of these potential days. Possibly more surface hoar days may have been found at the end of the 2014-2015 season but a site visit on February 27, 2015 for a potential day found both sites to be heavily tracked by snowmobilers and a

lone snowbiker. A lack of snowfall after this meadow ‘slayfest’ did not allow the snow surface at either site to recover to an acceptable condition for observation.

For events when no surface hoar was found, no single cause is determined although several factors may have led to the non-event. For several of the days, relative humidity measured at the sites was lower than what was found at any neighboring meteorological station. For other days, I observed a thin cirrus cloud layer above the sites that was not present to the north of the area or any webcam that morning and most likely inhibited formation. For another event, ideal nearby meteorological and clear sky conditions were found at the study area in the morning and a later analysis of the measured meteorological conditions at the sites showed cooler temperatures and a relative humidity greater than 85% for most of the overnight period. While this event demonstrates ideal meteorological conditions, the cause of the non-event is not known. While the goal of this study is not to predict surface hoar formation events, these trials illustrate the difficult nature of surface hoar prediction and a need for continued surface hoar forecasting research.

4.2 Preceding Weather and Avalanche Conditions

4.2.1 Jan2014 Event

January of 2014 began with snow, wind, and avalanches in the Taylor Fork and surrounding mountains. With an avalanche warning in place and an avalanche fatality 40 km north of the study plots, mountain riders were cautiously moving in avalanche terrain due to a basal instability. Snowmobilers near the study area experienced this first hand

and triggered avalanches on this weak layer. Small flurries of snow continued until January 13th when 8 cm of snow was recorded at the Carrot Basin SNOTEL. High pressure moved into the area bringing mostly sunny days and partly to mostly cloudy nights with moderate winds. Air temperature at the study plots was above freezing during the daytime with overnight lows barely below 0° C. On January 22nd, the dominating high pressure ridge briefly subsided, allowing for cooler temperatures and moist air to enter the region. The night of January 23rd brought one of the first clear nights for the month (observed at The Yellowstone Club) and cooler temperatures, yet relative humidity measured at the study plots and The Yellowstone Club was very low (~20-30%) and likely not conducive to surface hoar formation. A visit to both study sites the morning of January 24th confirmed this hypothesis with only small (.1-.3 mm) near surface facets (NSF) and decomposing crystals on the surface with a notable P- crust below the NSF at the South Site. Cloudless conditions continued in the area for the night of January 24th and higher, more favorable surface hoar formation humidities occurred at both sites. A visit on the morning of January 25th found surface hoar present at both study sites. This surface hoar event was widespread in the region with locations 60 km to the north exhibiting surface hoar. This layer was later buried in many locations and found to produce unstable test results two weeks later several kilometers from the study area.

4.2.1.1 North Site Weather conditions at the North Site exhibit temperatures and relative humidities consistent with prior research (e.g. Hachikubo, 2001). Plotted meteorological data shows a constant decrease of air temperature starting at 4°C during the day and falling to a low of -8° C at 07:00 on the morning of the 25th (Fig. 18).

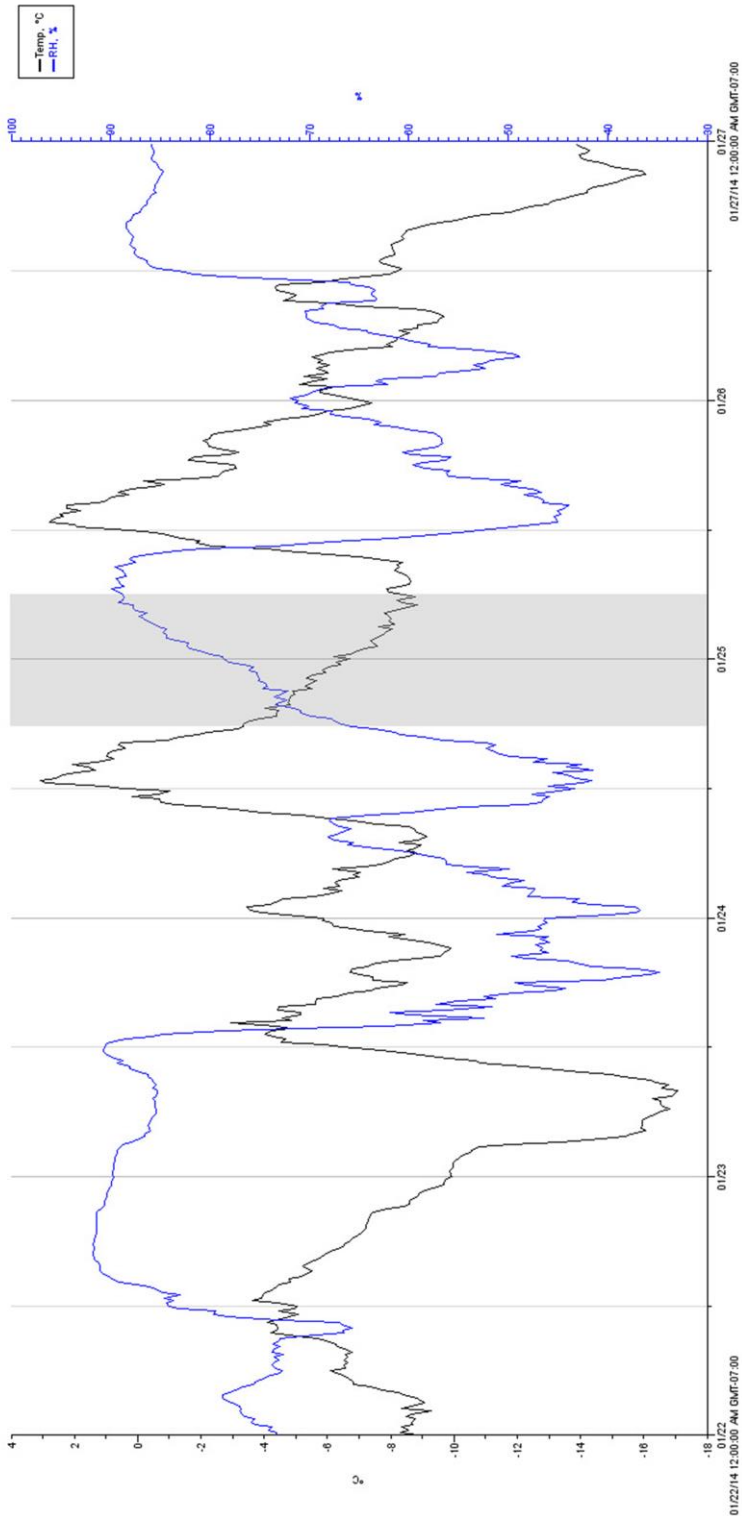


Figure 18. Temperature (black line; measured in °C) and relative humidity (blue line; measured in %) for the North Site recorded at 15 minute intervals from January 22, 2014 to January 27, 2014. The grey area indicates the probable overnight surface hoar formation period.

Overnight relative humidity increases from 40% to a maximum 90% at 07:00 the morning of the 25th. Temperatures and relative humidity were observed at 1.35 m above the snow surface.

Widespread surface hoar covered the North Site the morning of January 24, 2014. Sampling began at 13:00 and ended at 16:00. One hundred crystal and hemispheric images were taken at the site. Later inspection of the hemispheric images revealed a shift in the focal length of the lens that rendered 38 photos unusable for processing in GLA.

Surface hoar crystal sizes range from 0.5 mm to a single large 9 mm crystal (Table 3). Average crystal size for every observed crystal is 4.32 mm. Summary measures for each sample reveal medians within 2 mm but with smaller ranges (Fig. 19). $Size_{90th}$ and $Size_{Max}$ summary measures exhibit progressively larger means with decreasing ranges. All summary measures show evidence of outliers due to a few unusually large and small crystals.

Table 3. Summaries for observed surface hoar crystals, hemispheric sky visibility, total sunfleck duration, and total shortwave for the Jan2014 event for each site.

Jan2014												
Extent	Surface Hoar Size (mm)			ψ_{Sky} (%)			$\Sigma_{Sunfleck}$ (minutes)			$\Sigma_{Shortwave}$ (MJm^{-2}/d)		
	Min.	Max.	Mean	Min.	Max.	Mean	Min.	Max.	Mean	Min.	Max.	Mean
North Site	0.5	9	4.32	59.33	76.13	71.67	87	273	210	2.78	6.02	5.01
South Site	1	4	1.92	49.22	66.61	61.82	109	401	308	4.58	14.18	11.38

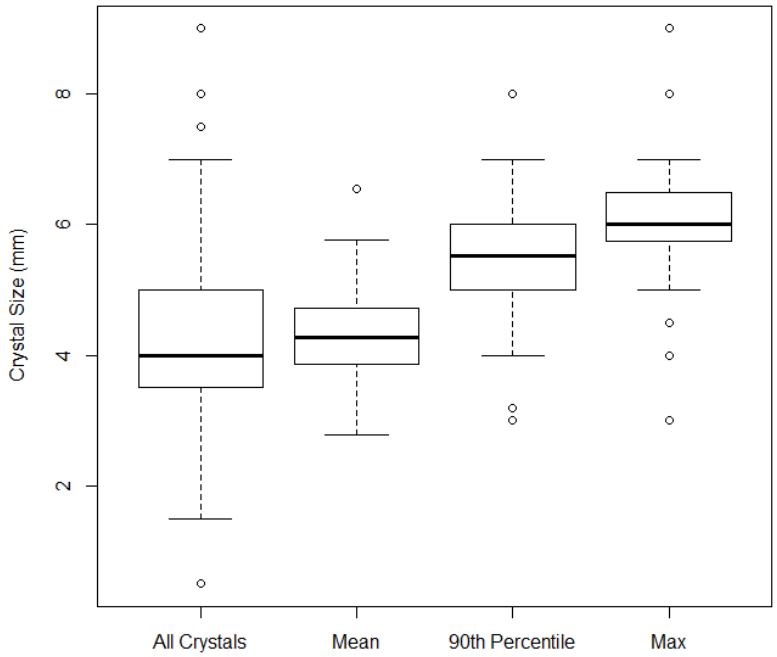


Figure 19. Boxplots for all sized crystals (n=1204) and crystal size summary measures (n=100) at the North Site for the Jan2014 event. The bold line represents the median, the box represents the interquartile range, and the whiskers 1.5x the interquartile range. Dots represent outlier values.

Tree canopy surrounding the site lacked snow cover, most likely due to warm air temperatures, sunny days, or small wind events that melted or transported any canopy snow. Derived ψ_{Sky} ranges from 59.33% to 76.13% though a mean ψ_{Sky} of 71.67% indicates few areas exhibited lower values (Table 3). Similar to Lutz (2009), surface hoar was found with ψ_{Sky} lower than the 65% threshold used by Helbig and van Herwijnen (2012). Derived $\Sigma_{Sunfleck}$ and $\Sigma_{Shortwave}$ indicate low radiation values with locations seeing between 1.45 and 4.55 hours of direct sunlight.

4.2.1.2 South Site Overnight meteorological conditions for the night of January 24th at the South Site exhibit trends that are mostly similar to the North Site (Fig. 20). A daily maximum temperature of 4.7° C at 15:15 was reached which then lowered,

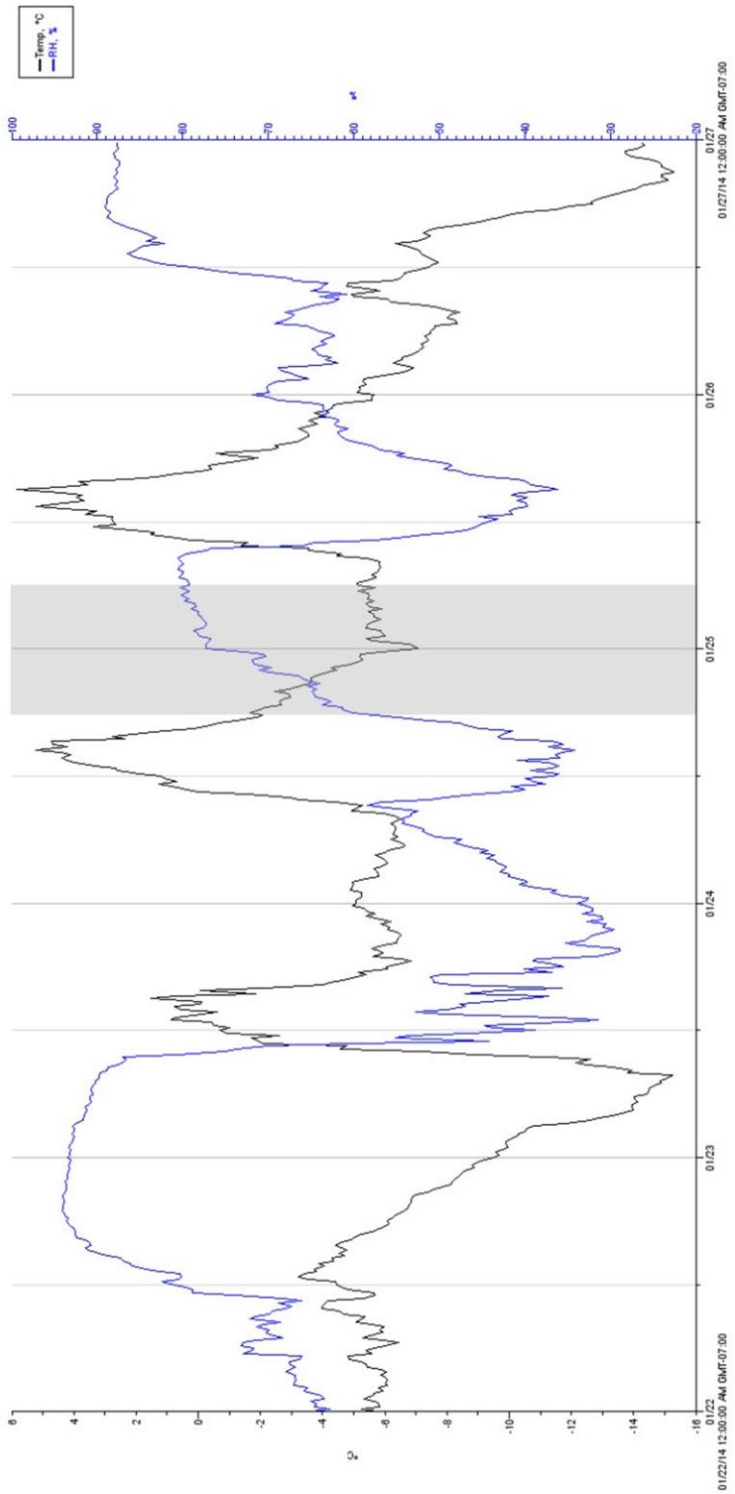


Figure 20. Temperature (black line; measured in °C) and relative humidity (blue line; measured in %) for the South Site recorded at 15 minute intervals from January 22, 2014 to January 27, 2014. The grey area indicates the probable overnight formation period prior to sampling.

eventually reaching a minimum of -7° C near 00:00. Slight warming occurred and temperatures remained constant until 08:00 the morning of January 25th. Relative humidity increased overnight from a low of 40%, reaching a maximum of only 80%; 10% lower than the North Site. Temperatures and relative humidity were measured at a height of 1.4 m above the snow surface.

Widespread surface hoar covered the South Site the morning of January 25, 2014. Sampling began at 07:00 and ended at 11:00. A total of 100 crystal and hemispheric images were taken at the site and all were useable.

Surface hoar crystals at the South Site are smaller than at the North Site. Surface hoar crystals range from 1.0 mm to 4.0 mm with a mean of 1.62 mm (Table 3). Median size for summary measures varies little and like the North Site, outliers are present (Fig. 21).

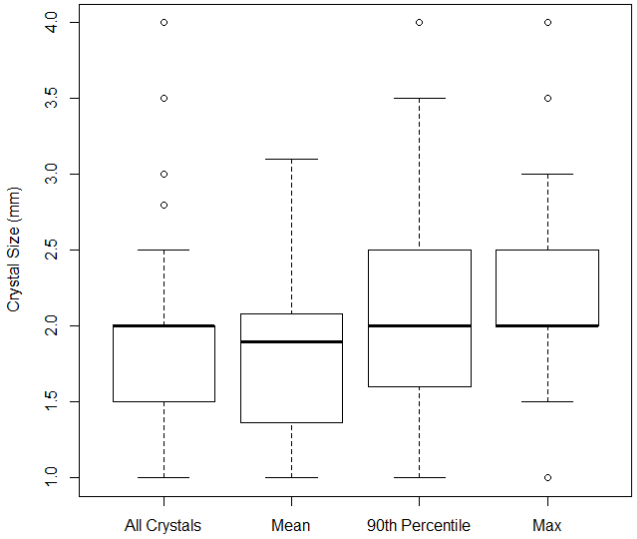


Figure 21. Boxplots for all sized crystals (n=917) crystal size summary measures (n=100) at the South Site for the Jan2014 event. The bold lines represent the median, the box represents the interquartile range, and the whiskers represent 1.5x the interquartile range. Dots represent outlier values.

The tree canopy at the South Site was free of snow, similar to the North Site. Derived ψ_{Sky} ranges from 49.22% to a maximum of 66.61%. A mean ψ_{Sky} of 61.82% indicates most measurements were taken in areas with larger ψ_{Sky} (Table 3). While the range of ψ_{Sky} is similar to North Site, most values are 10% lower, indicating a slightly more enclosed site due to tree canopy. Derived $\Sigma_{Sunfleck}$ and $\Sigma_{Shortwave}$ indicate relatively low amounts of direct sunlight and radiation but greater (up to 2x) than the North Site.

4.2.2 April2014 Event

A very late season surface hoar event occurred overnight between April 3rd and April 4th of 2014. While late season weak layer formation events such as these rarely become an avalanche problem, I examined this event as I was interested strictly in overnight surface hoar events prior to burial. This also allows for examination of a surface hoar event with a larger solar elevation angle and greater shortwave radiation than is seen for other events.

Winter did not take any breaks in March and the beginning of April of 2014. Air temperatures remained below freezing for all but two days and multiple 25+ cm snow storms (measured at the Carrot Basin SNOTEL) occurred. A final 7 cm of snow fell on April 2nd which became the snow surface on which this event grew. Storm systems briefly moved out of the area which allowed for optimal surface hoar formation conditions the night of April 3rd.

4.2.2.1 North Site Due to windy conditions and snowfall on April 4th, the North Site was unable to be sampled. Samples of surface hoar crystals were not useable and hemispheric photography was hindered with snow covering the lens.

4.2.2.2 South Site Weather conditions at the South Site on April 3rd indicate daytime warming to near 0° C at midday with a cooling trend beginning at 16:00 (Fig. 22). This trend continued until reaching a minimum temperature of -9° C near midnight which held until daytime warming began at 07:00 the morning of April 4th. The minimum temperature for this event was colder than the Jan2014 event. As temperatures dropped, relative humidity increased from ~60% to a maximum of ~90% at 20:00 on April 3rd and remained steady until the morning of April 4th. Temperatures and relative humidities were measured at a height of 1.35 m above the snow surface.

Unlike the prior event, surface hoar was not widespread over the site. Areas near up-slope trees contained no surface hoar. Sampling began at 07:00 and ended at 11:30 on April 4, 2014. A total of 100 hemispheric images were thought to be taken, but upon later inspection only 99 were captured.

With windy conditions at the study site, crystal photography was not possible due to snow crystals blowing off the crystal card during photography. I used an alternative method of sizing that utilized the same crystal card and a 10x magnifying loupe. I sized crystals for each sample using the mean maximum crystal size and was able to take one hundred measurements. This is the only event where surface hoar was not found at several sample locations. Seventeen locations clustered at the up-slope area of the study site exhibited no surface hoar. Crystal sizes are small and range from 0 mm to 4 mm with

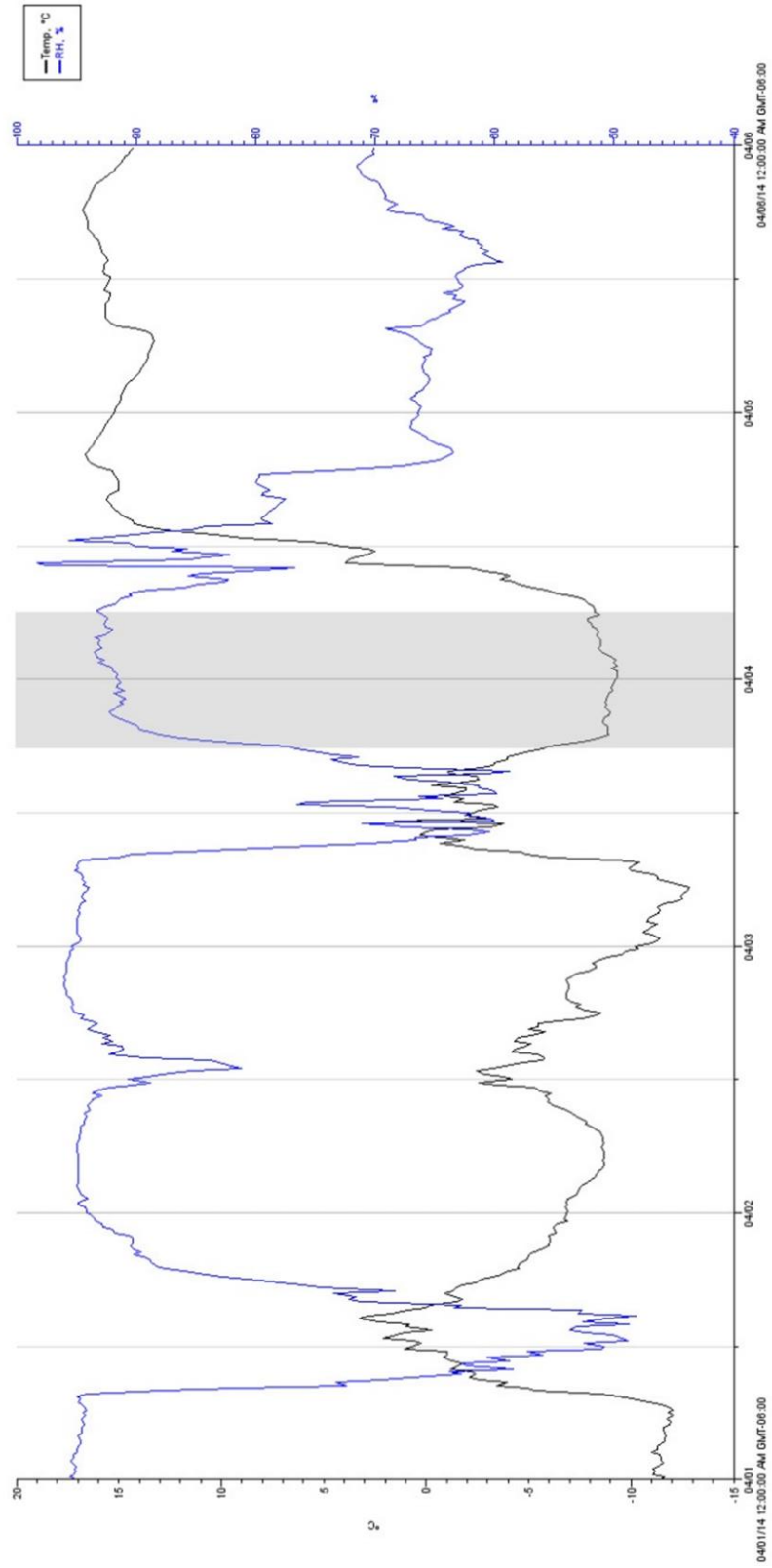


Figure 22. Temperature (black line; measured in °C) and relative humidity (blue line; measured in %) for the South Site recorded at 15 minute intervals from April 01, 2014 to April 06, 2014. The grey area indicates the probably overnight formation period prior to sampling.

a mean size of 1.25mm (Table 4). This event exhibits little variability in crystal sizes (Fig. 23).

Table 4. Summaries for surface hoar size, hemispheric sky visibility, total sunfleck duration, and total shortwave for the April2014 event at each site.

April2014												
Extent	Surface Hoar Size (mm)			ψ_{Sky} (%)			$\Sigma_{Sunfleck}$ (minutes)			$\Sigma_{Shortwave}$ (MJm^{-2}/d)		
	Min.	Max.	Mean	Min.	Max.	Mean	Min.	Max.	Mean	Min.	Max.	Mean
South Site	0	4	1.25	27.58	64.86	57.18	222	573	446	8.18	26.77	22.66

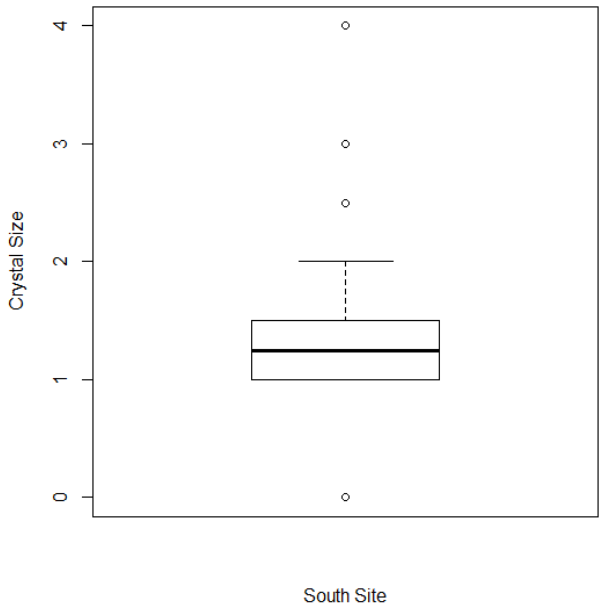


Figure 23. Boxplot for all sized crystals (n=100) at the South Site for the April2014 event. The bold line represents the median, the box represents the interquartile range, and the whiskers represent 1.5x the interquartile range. Dots represent outlier values.

The tree canopy was partially covered in snow from the most recent storm (Fig. 24). Derived ψ_{Sky} exhibits a large range from 27.58% to 64.86% due to a single sample near a very large tree (Table 4). Derived $\Sigma_{Sunfleck}$ and $\Sigma_{Shortwave}$ are larger than the Jan2014

event as is expected with increasing solar elevation angles near the end of the winter season.



Figure 24. Looking north-east after sampling the gridded layout at the South Site for the April2014 event. Snow is visible in the tree canopy.

4.2.3 Jan2015 Event

Multiple storm events starting in mid-December of 2014 stressed faceted snow near the ground that formed during extremely cold temperatures earlier in the season. While the snowpack was relatively thin in most areas for this time of year, strong winds created stiff slabs, producing avalanches. A 4-6 mm surface hoar layer buried 15 cm from the surface was found on December 20th in Sage Basin, 4 km east of the study area. A

substantial storm led to an avalanche warning issued for the area on December 25th and was the last significant snowfall leading into January. An arctic air mass moved into the area before the new year bringing extremely cold temperatures to the region. A temperature inversion was observed at nearby Lone Peak the morning of January 1st, 2015 with cloud levels filling the surrounding low valleys near the study area to the south. Surface hoar was observed at multiple elevations and aspects in the Big Sky area and sky conditions for the day of the 1st remained clear. Similar cloudless conditions and an inversion were again present the night of January 1st, 2015. Relative humidity measured at The Yellowstone Club was relatively high and temperatures remained below 0° C. A visit to the study area on January 2nd found surface hoar present at both study sites.

4.2.3.1 North Site For the overnight period between January 1st and January 2nd, weather conditions at the North Site were not measured due to a datalogging equipment malfunction. I examined weather station data gathered at both study sites from the prior season to determine if using the South Site data would be appropriate to fill in this missing data. I used a regression analysis to determine the relationship between temperature and relative humidity between the sites (Fig. 25). A linear function was deemed a reasonable fit (R^2 of .99 for temperature and .92 for relative humidity) and used to fill the missing data at the North Site. While good regression fits were found, the sites do not always exhibit similarities in these measurements, especially relative humidity (Fig. 25). This may be the case during this event and any weather data from the North Site should be viewed cautiously.

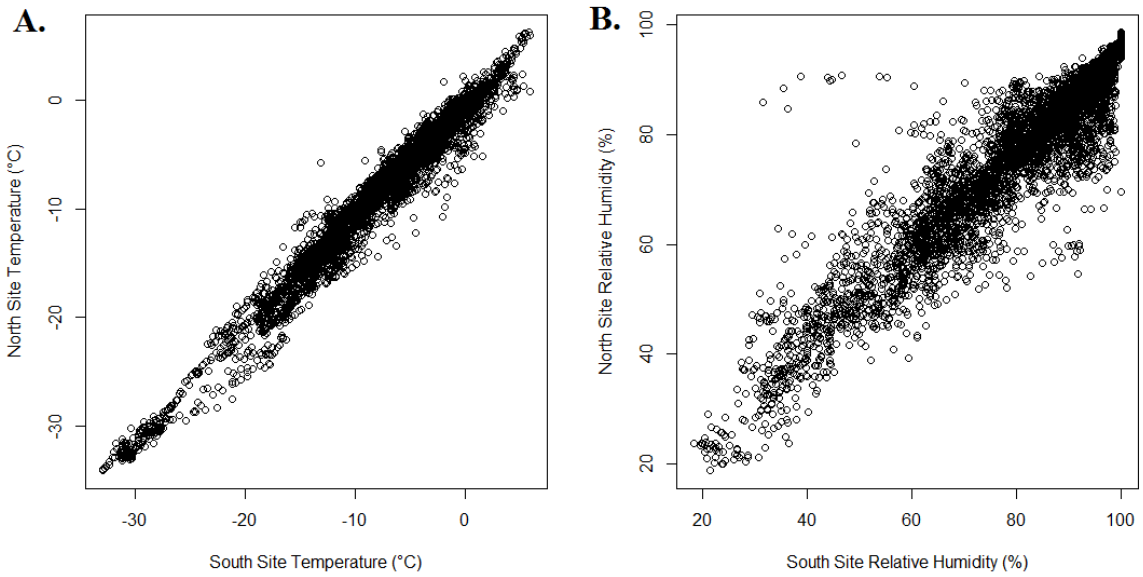


Figure 25. Plots of the North Site vs. (A) South Site temperature and (B) relative humidity.

As temperatures began to fall at 13:45 on January 1st, a drastic increase in relatively humidity occurred (Fig. 26). This increase from ~60% to ~90% occurred over 2 hours and held relatively steady until the next morning. Temperatures continued to fall overnight reaching a low of -5° C the morning of the 1st.

Widespread surface hoar covered the entire study site and even grew in thickly forested areas surrounding the site. Trees bordering the site were covered with the largest amount of snow observed during this study (Fig. 27). Surface hoar, equivalent to the size of many samples later taken at the site, covered snow patches on many trees. Sampling began at 12:30 and ended at 14:45. One hundred crystal and hemispheric images were taken at the site and all were deemed useable.

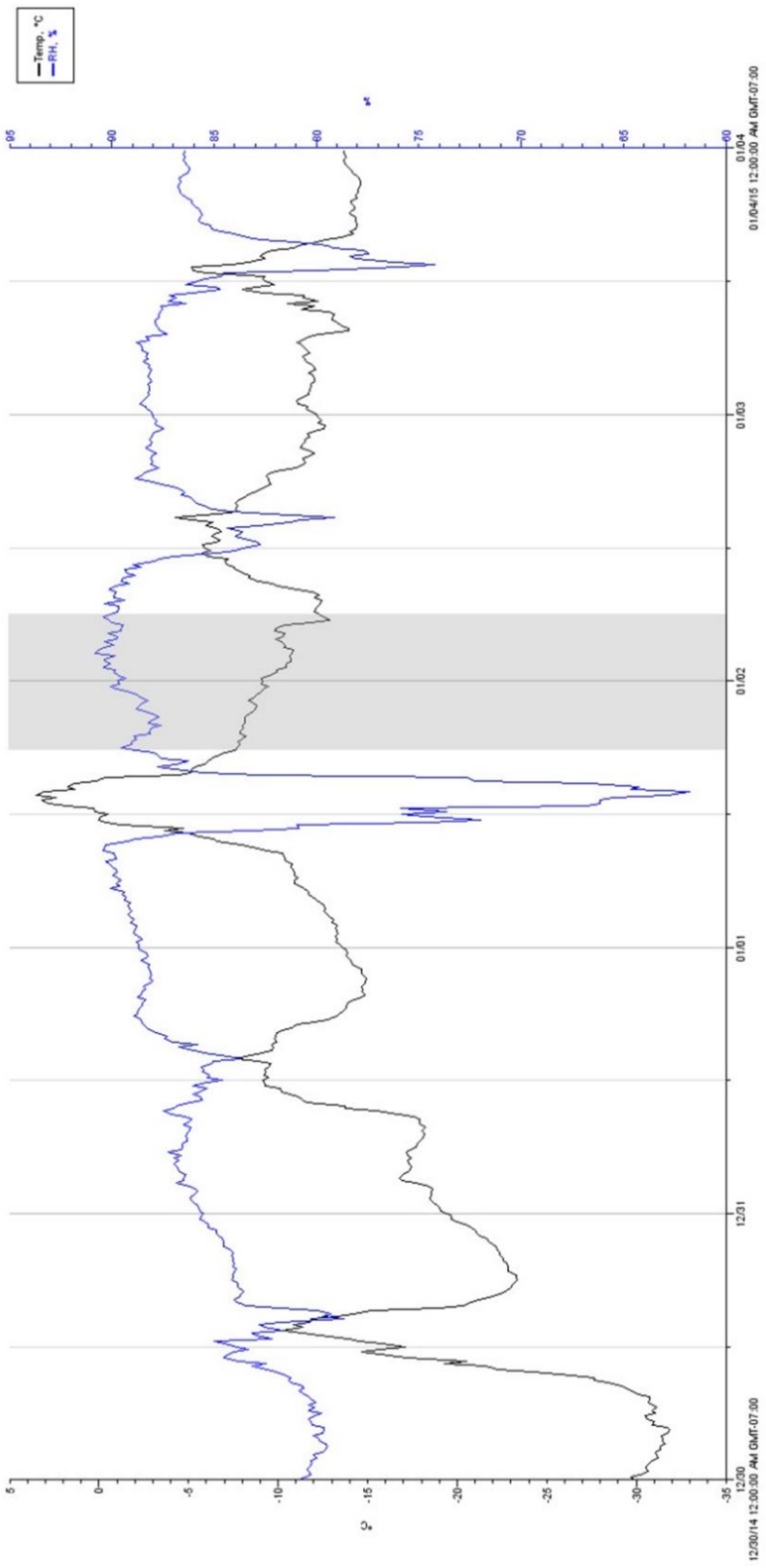


Figure 26. Estimated temperature (black line; measured in °C) and relative humidity (blue line; measured in %) for the North Site based on data from the South Site for the period of December 30, 2014 to January 04, 2015. The grey area indicates the probably overnight formation period prior to sampling.



Figure 27. A fisheye photograph viewing north (left side) to south (right side) after sampling the gridded layout at the North Site for the Jan2015 event.

Surface hoar crystal sizes are the largest observed for the three sampling dates. Sizes range from 1 mm to a very large 20 mm crystal (Table 5). The mean crystal size for every observed crystal is 7.45 mm. Summary measures have medians very similar to all sized crystals with increasing medians for $Size_{90th}$ and $Size_{Max}$ (Fig. 28). Outliers are present in the lower bounds for all summary statistics due to small crystals found at the south-west corner of the study site.

Table 5. Summaries for surface hoar size, hemispheric sky visibility, total sunfleck duration, and total shortwave for the Jan2015 event at each site.

Jan2015												
Extent	Surface Hoar Size (mm)			ψ_{Sky} (%)			$\Sigma_{Sunfleck}$ (minutes)			$\Sigma_{Shortwave}$ (MJm^{-2}/d)		
	Min.	Max.	Mean	Min.	Max.	Mean	Min.	Max.	Mean	Min.	Max.	Mean
North Site	1	20	7.45	27.27	72.9	64.01	0	182	69	0.21	3.65	2.08
South Site	1	28	5.61	21.08	66.16	52.72	0	322	178	0.49	11.62	6.87

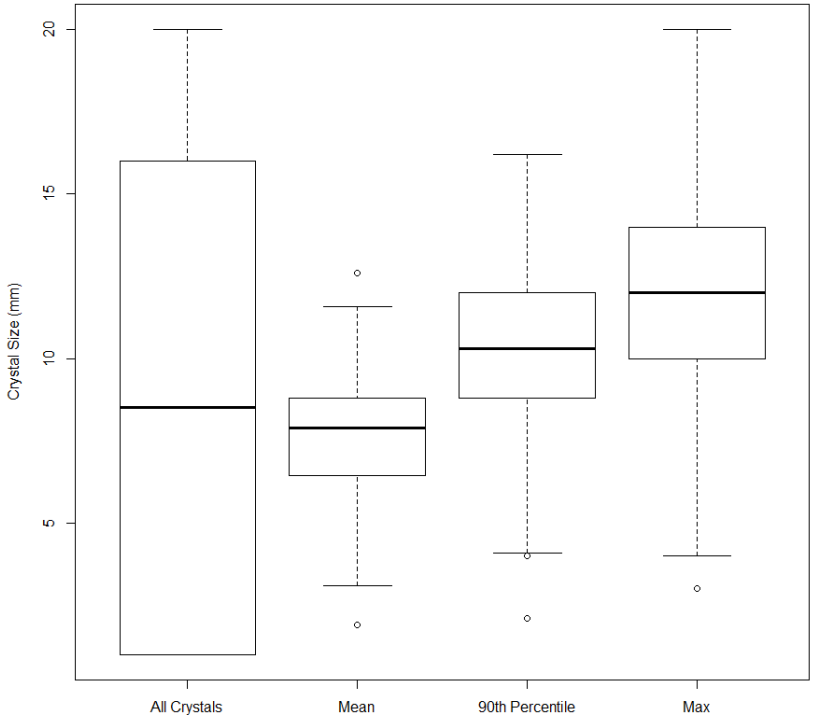


Figure 28. Boxplots for all sized crystals (n=815) and crystal size summary measures (n=100) at the North Site for the Jan2015 event. The bold line represents the median, the box represents the interquartile range, and the whiskers represent 1.5x the interquartile range. Dots represent outlier values.

The area received no significant warming or strong winds after the last snowfall and the forest canopy was snow covered in most areas except for the upper portions of trees at the northern end. Derived ψ_{Sky} values range from 27.27% to 72.9% with a mean

value of 64.01% (Table 5). Minimum ψ_{Sky} is affected by a sample near a small tree on the eastern portion of the meadow. Derived $\Sigma_{Sunfleck}$ and $\Sigma_{Shortwave}$ indicate low radiation values with the site receiving 0 to ~3 hours of direct sunlight which is lower than the Jan2014 event at this site. This difference can partially be attributed to the event occurring nearer to the winter solstice and having a lower solar elevation angle. Derived $\Sigma_{Shortwave}$ is again lower at this site than the South Site. While portions of the North Site do not receive any direct solar radiation, these areas do receive small amounts of diffuse radiation (Table 5).

4.2.3.2 South Site Similarities in the timing of a drop in air temperature and rise in relative humidity at the South Site are present as North Site weather data is based on the recorded data from the South Site. Air temperatures lower on the evening of the 1st and reach a minimum the morning of the 2nd (Fig. 29). As air temperature lowers, relative humidity increases to a maximum of ~96%. Relative humidity reaches 90% at 15:45 on the 1st and never falls below this threshold leading into the morning of the 2nd.

Surface hoar was widespread across the entire South Site. Sampling began at 07:00 and was completed at 10:30. One hundred crystal and hemispheric images were taken and all were sufficient for analysis.

Surface hoar crystals on the South Site are generally smaller than those on the North Site and range from 2 mm to 26 mm (Table 5). Several large crystals were sporadically found throughout the site and slightly tilted, possibly due to a small breeze (Fig. 30). Mean crystal size is 5.61 mm for every recorded crystal and is heavily right skewed due to the sporadic large crystals. Distributions for the summary measures are more normal yet still contain outliers (Fig. 31).

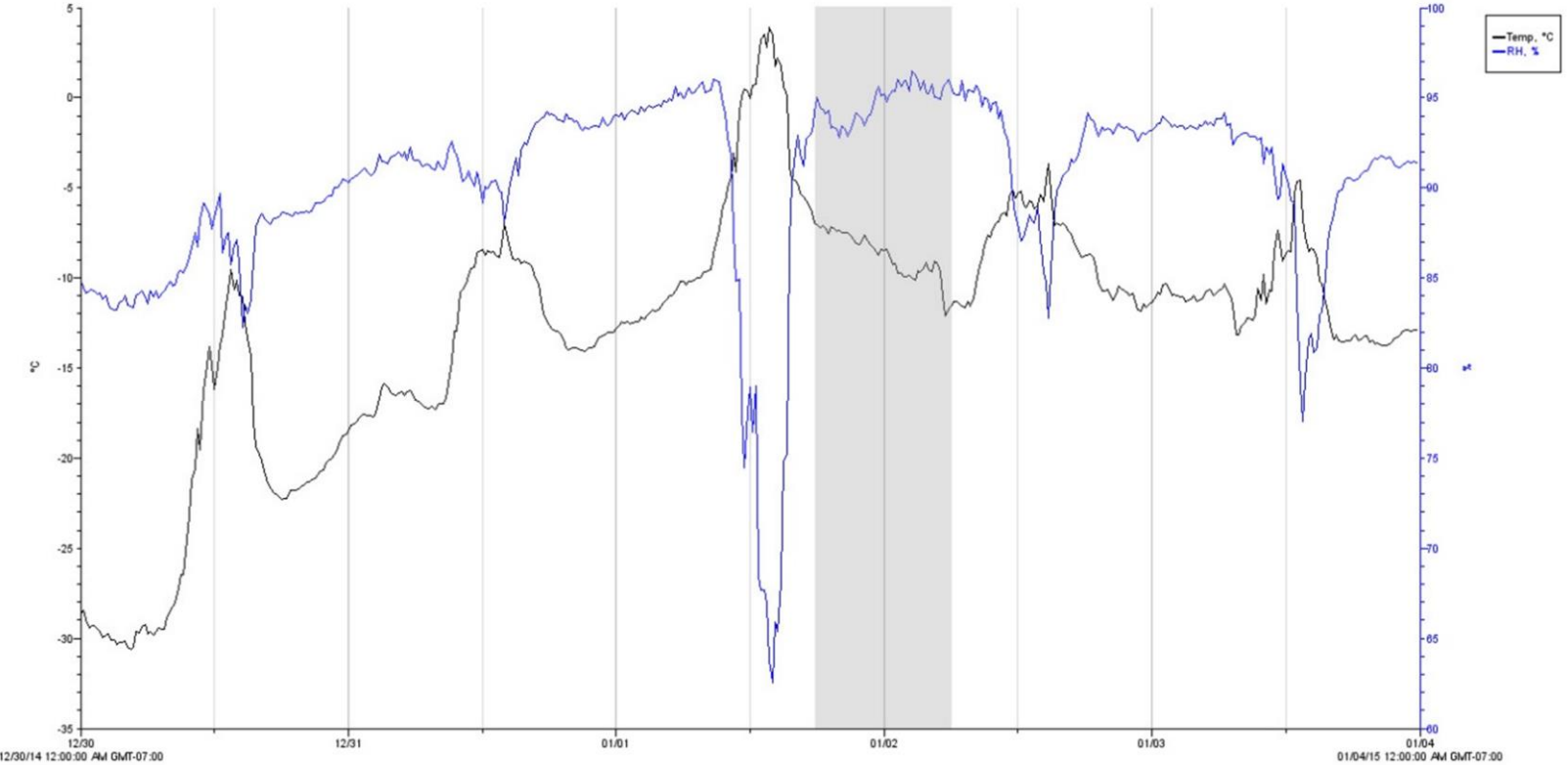


Figure 29. Temperature (black line; measured in °C) and relative humidity (blue line; measured in %) for the South Site recorded at 15 minute intervals from December 30, 2014 to January 4, 2015. The grey area indicates the probably overnight formation period prior to sampling.



Figure 30. Surface hoar crystals at the South Site for the Jan2015 event. Note the unusually large crystals (>20 mm) just left and right of center.

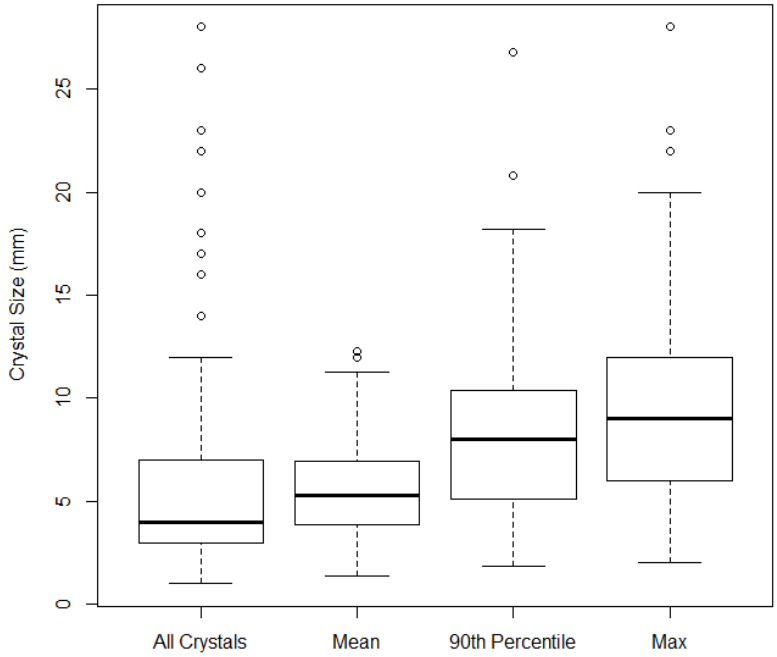


Figure 31. Boxplots for all sized crystals (n=883) and crystal size summary measures (n=100) at the South Site for the Jan2015 event. The bold line represents the median, the box represents the interquartile range, and the whiskers represent 1.5x the interquartile range. Dots represent outlier values.

Similar to the North Site, trees were snow covered although no surface hoar grew in any elevated snow patches. Derived ψ_{Sky} values range from 21.08% to 66.16%, similar to the Jan2014 event (Table 5). Like the North Site, minimum ψ_{Sky} is influenced by a lone measurement near a large tree. Derived $\Sigma_{Sunfleck}$ and $\Sigma_{Shortwave}$ values are relatively low but generally larger than values from the North Site. Even though the site is south facing, areas near the bottom of the site receive no direct sunlight during this time of the year.

4.3 Regression Analysis: Single Explanatory Variable

Scatterplots and Spearman rank-order correlation coefficients indicate several trends and significant correlations. Scatterplots show weak trends at the South Site for the Jan2014 and Jan2015 events (Fig. 32). All sizing measures for the Jan2014 event at the South Site are negatively correlated with $\Sigma_{Sunfleck}$ or $\Sigma_{Shortwave}$ (Table 6). Significant positive correlations with ψ_{Sky} and all sizing measures are found for the Jan2015 event at the South Site. There are no significant correlations at the North Site for all events or South Site for the April2014 event. Scatterplots for non-significant correlations lack any identifiable trends. Scatterplot trends for significant correlations are more easily discerned but still display a high amount of variability (Fig. 33). Major differences in scatterplots are evident when comparing low correlations and high correlations (Fig. 33).

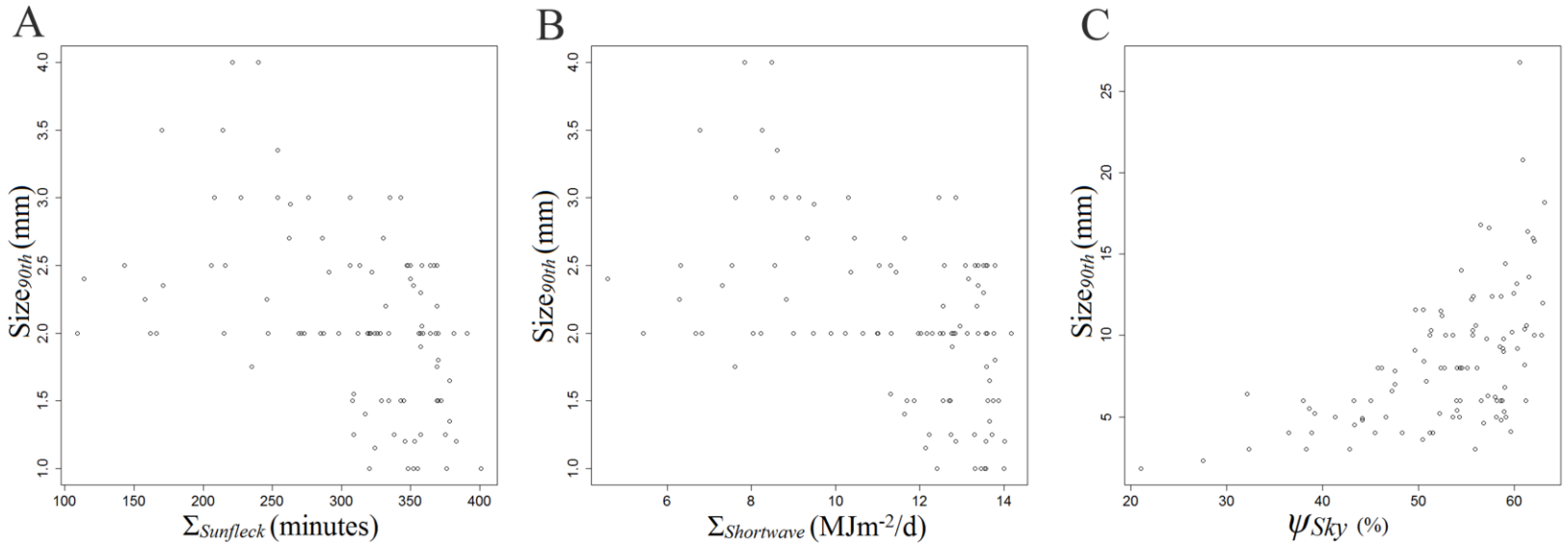


Figure 32. Scatterplots of $Size_{90th}$ vs. $\Sigma_{Sunfleck}$ (A) and $\Sigma_{Shortwave}$ (B) for the Jan2014 event at the South Site and $Size_{90th}$ vs. ψ_{Sky} (C) for the Jan2015 event at the South Site.

Table 5. Spearman rank-order correlation coefficients for derived environmental variables and sizing measures at each study site and date. Bold represents a significant (p-value ≤ 0.05) result.

	Jan2014 – North Site			Jan2014 – South Site			April2014	Jan2015 – North Site			Jan2015 – South Site		
Variable	$Size_{Mean}$	$Size_{90th}$	$Size_{Max}$	$Size_{Mean}$	$Size_{90th}$	$Size_{Max}$	$Size_{Actual}$	$Size_{Mean}$	$Size_{90th}$	$Size_{Max}$	$Size_{Mean}$	$Size_{90th}$	$Size_{Max}$
ψ_{Sky}	0.08	0.13	0.08	0.03	0.02	0.03	0.12	0.11	0.02	0.03	**0.59**	**0.57**	**0.59**
$\Sigma_{Sunfleck}$	-0.07	-0.09	-0.19	**-0.43**	**-0.43**	**-0.41**	0.13	-0.18	-0.07	-0.01	0.02	0.02	0.06
$\Sigma_{Shortwave}$	-0.01	-0.02	-0.11	**-0.47**	**-0.45**	**-0.43**	0.06	-0.13	-0.03	0.02	-0.02	-0.02	0.04

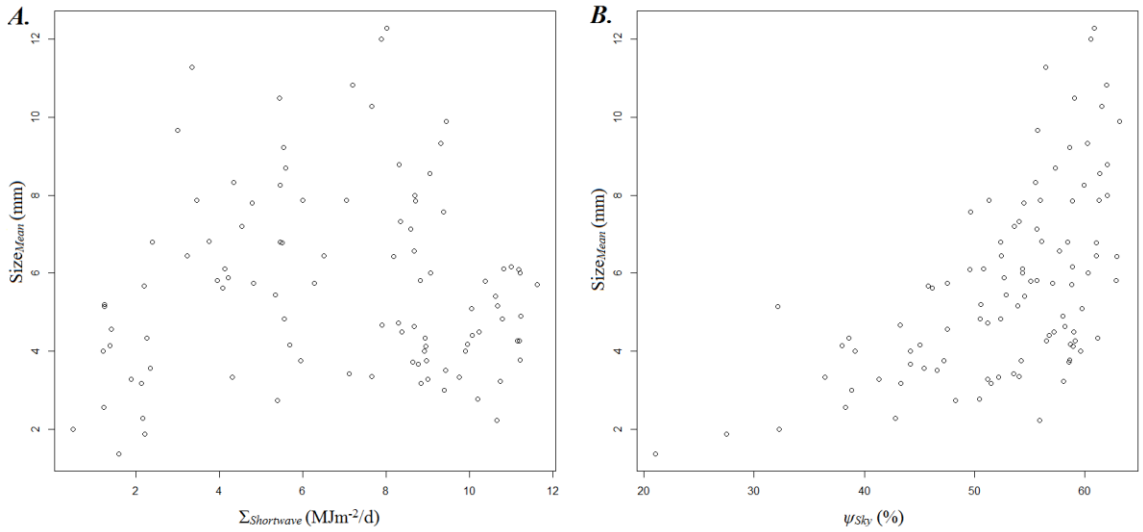


Figure 33. Plots of $\Sigma_{Shortwave}$ (A) and ψ_{Sky} (B) vs. Size$_{Mean}$ for the Jan2015 event at the South Site.

4.3.1 Linear Regressions

I explored the individual effects and influences of the chosen environmental determinants on the three sizing measures using linear regression. For each initial OLS regression model, I examined diagnostic plots to assess for linearity, homoscedacity, and normality. While some models show small departures from one or both assumptions, attempts at corrections with log-transformations provided little to no improvement. With no drastic departures from these assumptions, all regressions use the original, non-transformed data. The Moran's I test indicated a significant amount of spatial autocorrelation in the residuals of all OLS models. I fit spatial regression models to account for this autocorrelation.

4.3.1.1 Jan2014 North Site There are no significant relationships at the site or south plot level. A significant relationship exists at the north plot between Size$_{90th}$ and ψ_{Sky} (Table 7). This relationship is only found in the spatial error model.

Table 7. Significant regression fits for each spatial regression model between sizing measures and derived environmental variables for the Jan2014 event at the North Site.

Jan2014 – North Site			
Variables	Extent	Lag Model	Error Model
$Size_{90th} \sim \psi_{Sky}$	*North Plot*	x	(+)

x = not significant; (+) = positive relationship; (-) = negative relationship

4.3.1.2 Jan2014 South Site No significant relationships are identified in either spatial model.

4.3.1.3 April2014 South Site Spatial regression models indicate a significant positive relationship between ψ_{Sky} and $Size_{Actual}$ at the south plot (Table 8). This may indicate areas at the South Site that are furthest from the warm up-slope trees, snow surface cooling is controlled by ψ_{Sky}, yielding larger surface hoar.

Table 8. Significant regression fits for each spatial regression model between sizing measures and derived environmental variables for the April2014 event at the South Site.

April2014 – South Site			
Variable	Extent	Lag Model	Error Model
$Size_{actual} \sim \psi_{Sky}$	*South Plot*	**(+)**	**(+)**

x = not significant; (+) = positive relationship; (-) = negative relationship

4.3.1.4 Jan2015 North Site Spatial regression models show similar results and find significant positive relationships between ψ_{Sky} and $Size_{Max}$ at the entire site and between ψ_{Sky} and $Size_{Mean}$ at the south plot (Table 9).

Table 9. Significant regression fits for each spatial regression model between sizing measures and derived environmental variables for the Jan2014 event at the North Site.

Jan2015 – North Site			
Variables	Extent	Lag Model	Error Model
$Size_{Mean} \sim \psi_{Sky}$	*South Plot*	**(+)**	**(+)**
$Size_{Max} \sim \psi_{Sky}$	Site	**(+)**	**(+)**

x = not significant; (+) = positive relationship; (-) = negative relationship

4.3.1.5 Jan2015 South Site Spatial regression models show similar results in all but two models (Table 10). At the entire site and both sub-plots, $Size_{90th}$ and $Size_{Max}$ are significantly associated with ψ_{Sky}. $Size_{Max}$ is also significantly associated with $\Sigma_{Sunfleck}$ at the site level and south plot while $Size_{90th}$ is only associated with $\Sigma_{Sunfleck}$ at the south plot. All significant relationships with ψ_{Sky} are positively associated. While ψ_{Sky} is expected to be positively associated with size measures, positive associations with $\Sigma_{Sunfleck}$ and $\Sigma_{Shortwave}$ are not. Though found mostly on the south plot, causes for this relationship are not known.

Table 10. Significant regression fits for each spatial regression model between sizing measures and derived environmental variables for the Jan2015 event at the South Site.

Jan2015 – South Site			
Variable	Extent	Lag Model	Error Model
$Size_{90th} \sim \psi_{Sky}$	Site	(+)	(+)
	North Plot	(+)	(+)
	South Plot	(+)	x
$Size_{Max} \sim \psi_{Sky}$	Site	(+)	(+)
	North Plot	(+)	(+)
	South Plot	(+)	(+)
$Size_{90th} \sim \Sigma_{Sunfleck}$	*South Plot*	(+)	(+)
$Size_{Max} \sim \Sigma_{Sunfleck}$	Site	x	(+)
	South Plot	(+)	(+)
$Size_{Max} \sim \Sigma_{Shortwave}$	*South Plot*	(+)	(+)

x = not significant; (+) = positive relationship; (-) = negative relationship

4.4 Regression Analysis: Multiple Explanatory Variables

4.4.1 Multiple Regression

Multiple regression analysis is used to assess for the combined effects of ψ_{Sky} with $\Sigma_{Sunfleck}$ or $\Sigma_{Shortwave}$ on surface hoar size. As $\Sigma_{Sunfleck}$ and $\Sigma_{Shortwave}$ are highly collinear, they are tested separately. Similar to the prior regression analysis, I assessed each OLS model for departures from model assumptions. I observed small departures in one or both

diagnostic plots and data transformations helped little to change the plotted characteristics. With no major departures, I created models using non-transformed data. The Moran's I test indicated a significant amount of spatial autocorrelation in the residuals of all OLS models. I fit spatial regression models to account for this autocorrelation.

4.4.1.1 Jan2014 North Site Spatial regression models show generally similar results except for three instances where ψ_{Sky} is not significant in the error model (Table 11). Generally, when a significant relationship is found with ψ_{Sky}, the relationship is positive and larger surface hoar is found in areas with the largest ψ_{Sky}. When $\Sigma_{Sunfleck}$ or $\Sigma_{Shortwave}$ are significant, the relationship is negative. Areas with larger $\Sigma_{Sunfleck}$ or $\Sigma_{Shortwave}$ have the smallest surface hoar. Only some agreement between significant parameters is found between the models. Models show significant relationships at both the site and sub-plot levels but these results vary depending on the summary measure.

4.4.1.2 Jan2014 South Site Spatial models are in agreement for significant coefficients in all but two models (Table 12). For significant parameters, coefficients are positive for ψ_{Sky} and negative for $\Sigma_{Sunfleck}$ or $\Sigma_{Shortwave}$. All spatial lag models show both coefficients as significant and all but three error models show a similar result. Most significant assocations are found at the site level with only two error models showing significant parameters at the south plot.

Table 11. Significant regression fits for each spatial regression model between sizing measures and derived environmental variables for the Jan2014 event at the North Site.

Jan2014 – North Site					
Variable	Extent	Lag Model		Error Model	
		ß$_1$	ß$_2$	ß$_1$	ß$_2$
$Size_{Mean} \sim \psi_{Sky} + \Sigma_{Sunfleck}$	Site	**(+)**	x	x	x
	South Plot	**(+)**	x	**(+)**	**(-)**
$Size_{Mean} \sim \psi_{Sky} + \Sigma_{Shortwave}$	*South Plot*	**(+)**	x	**(+)**	**(-)**
$Size_{90th} \sim \psi_{Sky} + \Sigma_{Sunfleck}$	Site	**(+)**	x	x	x
	North Plot	**(+)**	**(-)**	**(+)**	(-)
	South Plot	x	x	**(+)**	(-)
$Size_{90th} \sim \psi_{Sky} + \Sigma_{Shortwave}$	*North Plot*	**(+)**	x	x	x
	South Plot	**(+)**	x	**(+)**	**(-)**
$Size_{Max} \sim \psi_{Sky} + \Sigma_{Sunfleck}$	Site	**(+)**	**(-)**	**(+)**	**(-)**
	North Plot	**(+)**	**(-)**	**(+)**	**(-)**
	South Plot	(+)	x	(+)	(-)
$Size_{Max} \sim \psi_{Sky} + \Sigma_{Shortwave}$	Site	(+)	x	(+)	(-)
	North Plot	(+)	x	(+)	(-)
	South Plot	(+)	x	(+)	(-)

x = not significant; (+) = positive relationship; (-) = negative relationship

Table 12. Significant regression fits for each spatial regression model between sizing measures and the derived environmental variables for the Jan2014 event at the South Site.

Jan2014 – South Site					
Variable	Extent	Lag Model		Error Model	
		ß$_1$	ß$_2$	ß$_1$	ß$_2$
$Size_{Mean} \sim \psi_{Sky} + \Sigma_{Sunfleck}$	Site	x	(-)	(+)	x
	South Plot	x	x	(+)	(-)
$Size_{Mean} \sim \psi_{Sky} + \Sigma_{Shortwave}$	Site	x	(-)	(+)	x
	South Plot	x	x	(+)	x
$Size_{90th} \sim \psi_{Sky} + \Sigma_{Sunfleck}$	Site	(+)	(-)	(+)	(-)
$Size_{90th} \sim \psi_{Sky} + \Sigma_{Shortwave}$	Site	(+)	(-)	(+)	(-)
$Size_{Max} \sim \psi_{Sky} + \Sigma_{Sunfleck}$	Site	(+)	(-)	(+)	(-)
$Size_{Max} \sim \psi_{Sky} + \Sigma_{Shortwave}$	Site	(+)	(-)	(+)	(-)

x = not significant; (+) = positive relationship; (-) = negative relationship

4.4.1.3 April2014 South Site Spatial regression models do not exhibit similar significant parameters (Table 13). While spatial error models do show significant relationships, spatial lag models indicate there are none. Significant relationships are found only at sub-plots and not at the site extent. All significant models indicate positive relationships with ψ_{Sky} and negative relationships with $\Sigma_{Sunfleck}$ or $\Sigma_{Shortwave}$.

Table 13. Significant regression fits for each spatial regression model between sizing measures and derived environmental variables for the April2014 event at the South Site.

April2014 – South Site					
Variable	Extent	Lag Model		Error Model	
		ß$_1$	ß$_2$	ß$_1$	ß$_2$
$Size_{actual} \sim \psi_{Sky} + \Sigma_{Sunfleck}$	*North Plot*	x	x	(+)	x
	South Plot	x	x	(+)	(-)
$Size_{actual} \sim \psi_{Sky} + \Sigma_{Shortwave}$	*South Plot*	x	x	(+)	(-)

x = not significant; **(+)** = positive relationship; **(-)** = negative relationship

4.4.1.4 Jan2015 North Site Spatial regression models show positive relationships with ψ_{Sky} and negative relationships with $\Sigma_{Sunfleck}$ or $\Sigma_{Shortwave}$ (Table 14). Significant relationships are found at both the site and south plot levels, with no significant parameters found on any north plot.

Table 14. Significant regression fits for each spatial regression model between sizing measures and derived environmental variables for the Jan2015 event at the North Site.

Jan2015 –North Site					
Variable	Extent	Lag Model		Error Model	
		ß$_1$	ß$_2$	ß$_1$	ß$_2$
$Size_{Mean} \sim \psi_{Sky} + \Sigma_{Sunfleck}$	Site	(+)	(-)	(+)	(-)
	South Plot	(+)	(-)	(+)	x
$Size_{Mean} \sim \psi_{Sky} + \Sigma_{Shortwave}$	Site	(+)	(-)	(+)	(-)
	South Plot	(+)	(-)	(+)	(-)
$Size_{90th} \sim \psi_{Sky} + \Sigma_{Sunfleck}$	Site	(+)	(-)	(+)	(-)
	South Plot	(+)	x	(+)	x
$Size_{90th} \sim \psi_{Sky} + \Sigma_{Shortwave}$	Site	(+)	(-)	(+)	(-)
	South Plot	(+)	x	(+)	(-)
$Size_{Max} \sim \psi_{Sky} + \Sigma_{Sunfleck}$	Site	(+)	(-)	(+)	x
	South Plot	(+)	x	(+)	x
$Size_{Max} \sim \psi_{Sky} + \Sigma_{Shortwave}$	Site	(+)	(-)	(+)	x
	South Plot	(+)	x	(+)	x

x = not significant; (+) = positive relationship; (-) = negative relationship

4.4.1.5 Jan2015 South Site Spatial regression models with significant relationships are found at the site and sub-plot levels (Table 15). Significant positive relationships are found for ψ_{Sky} and significant negative relationships for $\Sigma_{Sunfleck}$ or

$\Sigma_{Shortwave}$. While most models find a significant relationship with ψ_{Sky}, very few find both coefficients as significant.

Table 15. Significant regression fits for each spatial regression model between sizing measures and derived environmental variables for the Jan2015 event at the South Site.

Jan2015 – South Site					
Variable	Extent	Lag Model		Error Model	
		ß₁	**ß₂**	**ß₁**	**ß₂**
$Size_{Mean} \sim \psi_{Sky} + \Sigma_{Sunfleck}$	Site	(+)	x	(+)	x
	South Plot	(+)	x	x	(-)
$Size_{Mean} \sim \psi_{Sky} + \Sigma_{Shortwave}$	Site	(+)	x	(+)	x
	South Plot	(+)	x	(+)	x
$Size_{90th} \sim \psi_{Sky} + \Sigma_{Sunfleck}$	Site	(+)	(-)	(+)	(-)
	North Plot	(+)	x	(+)	x
	South Plot	(+)	x	(+)	x
$Size_{90th} \sim \psi_{Sky} + \Sigma_{Shortwave}$	Site	(+)	(-)	(+)	(-)
	North Plot	(+)	(-)	(+)	x
	South Plot	(+)	x	(+)	(-)
$Size_{Max} \sim \psi_{Sky} + \Sigma_{Sunfleck}$	Site	(+)	x	(+)	(-)
	North Plot	(+)	x	(+)	x
	South Plot	(+)	x	(+)	x
$Size_{Max} \sim \psi_{Sky} + \Sigma_{Shortwave}$	Site	(+)	(-)	(+)	(-)
	North Plot	(+)	(-)	(+)	x
	South Plot	(+)	x	(+)	x

x = not significant; (+) = positive relationship; (-) = negative relationship

4.4.2 Regression Trees

I grew regression trees using sizing measures and derived environmental determinants for each site on each sampling date. I grew initial trees with a minimum terminal node size of five observations to ensure trees were grown to a substantial extent to allow for initial exploration and subsequent pruning. I pruned each tree using 10-fold cross validation and the 1-standard error rule (Breiman et al., 1984). Four trees, the Jan2015 trees and the April2014 tree, have no splits that fall within the 1-standard error rule. I discuss regression tree results in the following section and include one overfit regression tree to illustrate a result prior to pruning.

4.4.2.1 Jan2014 North Site Regression trees grown for $Size_{Mean}$, $Size_{90th}$, and $Size_{Max}$ do not contain any splits that are within 1-standard error of the best tree. The $Size_{90th}$ overfit regression tree contains six terminal nodes and explains 27% of the variance (Fig. 34). The primary split for $Size_{90th}$ occurs on $\Sigma_{Sunfleck}$ while secondary splits are on ψ_{Sky}. The $Size_{Mean}$ overfit regression tree has a primary split on ψ_{Sky} while the overfit regression tree for $Size_{Max}$ splits on $\Sigma_{Sunfleck}$ (Appendix D). $Size_{Mean}$ and $Size_{90th}$ regression trees suggest that larger surface hoar is found in areas that receive lower amounts of direct sunlight and have larger ψ_{Sky}. The $Size_{Max}$ tree suggests radiation is the primary determinant of surface hoar size. However, the low R^2 values and lack of any cross-validated trees indicate there are no reasonable splitting thresholds for determining surface hoar size using environmental determinants. Associations are lacking for this site and event which is similar to findings in regression analyses.

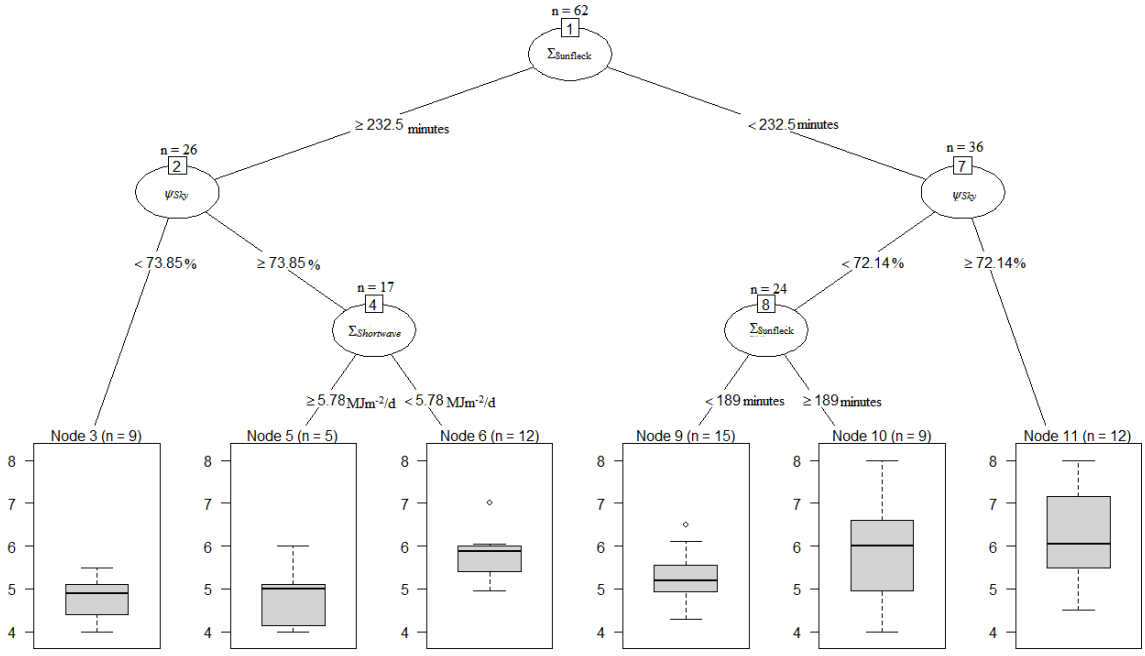


Figure 34. Overfit regression tree for $Size_{90th}$ for Jan2014 at the North Site with boxplots showing terminal node distributions. For each boxplot, the bold line represents the median, the box represents the interquartile range, and the whiskers represent 1.5x the interquartile range. Dots represent outlier values.

4.4.2.2 Jan2014 South Site After pruning, three similar regression trees are created (Figs. 35-37). These trees explain between 24% and 29% of the variance for sizing measures (Table 16). The $Size_{Mean}$, $Size_{90th}$, and $Size_{Max}$ trees each contain a single split which occurs on $\Sigma_{Shortwave}$. The singular split on $\Sigma_{Shortwave}$ uses splitting thresholds between 10.54-11.30 MJm^{-2}/d which are very close to the mean $\Sigma_{Shortwave}$ of 11.38 MJm^{-2}/d. These trees suggest larger surface hoar is found in areas that receive lower amounts of solar radiation and ψ_{Sky} may not be a controlling factor at this site for this event. It is important to note that in the overfit trees, ψ_{Sky} is the next splitting criterion with larger ψ_{Sky} associated with larger surface hoar (Appendix D).

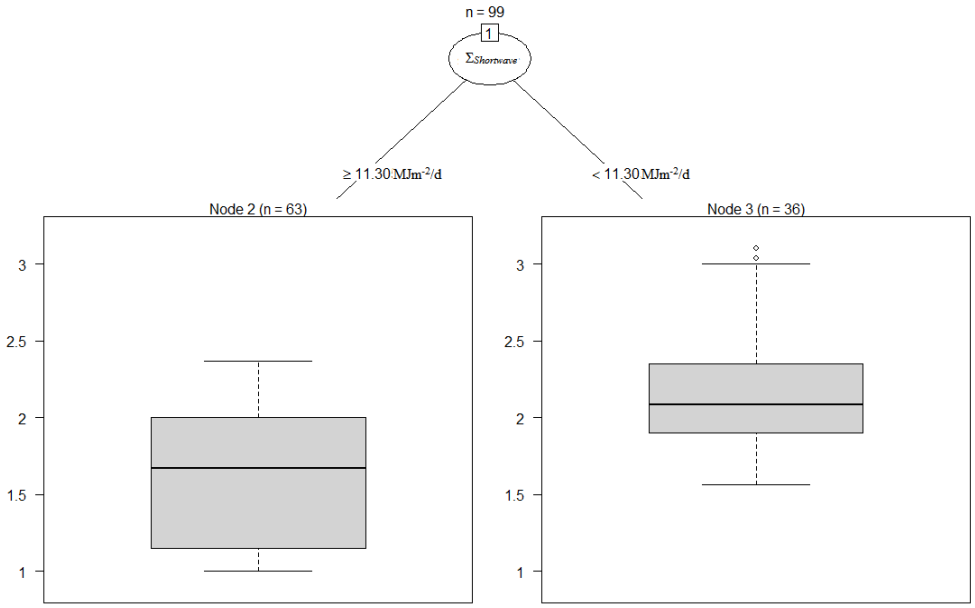


Figure 35. Pruned regression tree for Size$_{Mean}$ for Jan2014 at the South site with boxplots showing terminal node distributions. For each boxplot the bold line represents the median, the box represents the interquartile range, and the whiskers represent 1.5x the interquartile range. Dots represent outlier values.

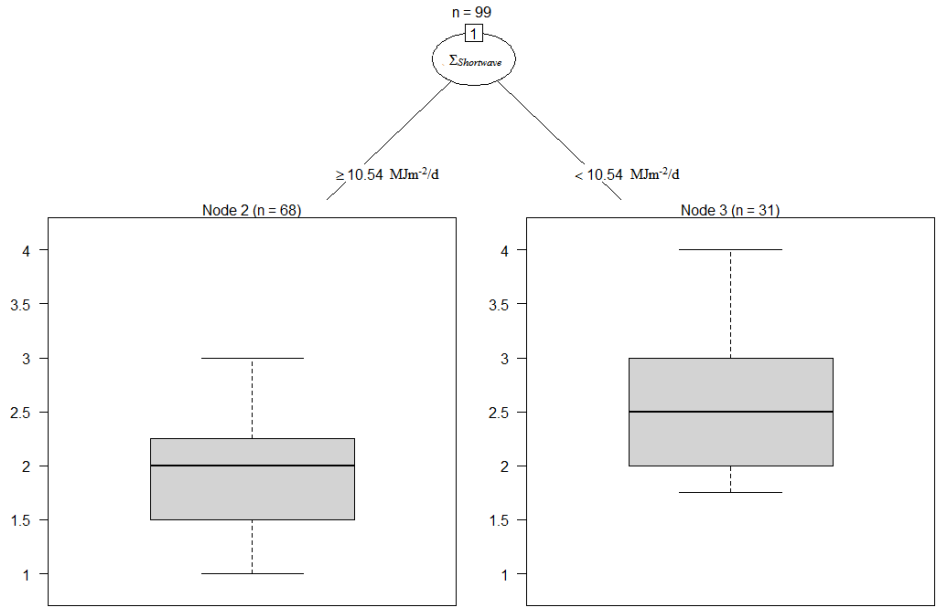


Figure 36. Pruned regression tree for Size$_{90th}$ for Jan2014 at the South Site with boxplots showing terminal node distributions. For each boxplot the bold line represents the median, the box represents the interquartile range, and the whiskers represent 1.5x the interquartile range. Dots represent outlier values.

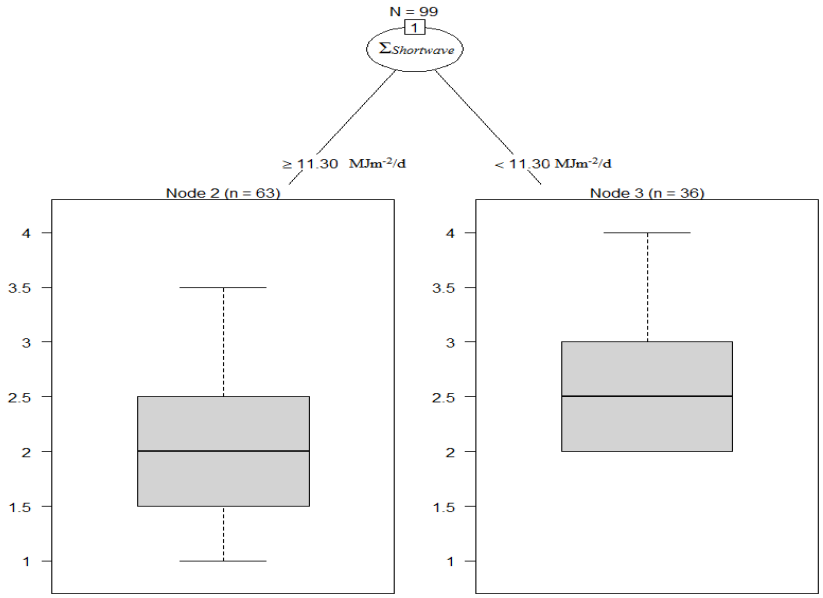


Figure 37. Pruned regression tree for Size$_{Max}$ for Jan2014 at the South Site with boxplots showing terminal node distributions. For each boxplot the bold line represents the median, the box represents the interquartile range, and the whiskers represent 1.5x the interquartile range. Dots represent outlier values.

4.4.2.3 April2014 South Site No regression trees splits are found when using the 1-standard error rule for this event.

4.4.2.4 Jan2015 North Site After pruning, three different regression trees for this event are grown (Figs. 38-40). These regression trees explain 15% to 38% of the variation for the sizing measures (Table 16). The Size$_{Mean}$ tree contains six terminal nodes and has an initial split on ψ_{Sky}. Larger ψ_{Sky} values are then split using $\Sigma_{Sunfleck}$ and ψ_{Sky} (Fig. 38). The Size$_{90th}$ tree has three terminal nodes and contains the same splitting threshold on ψ_{Sky} as the other two trees, but with a slightly lower secondary splitting threshold for $\Sigma_{Sunfleck}$ (Fig. 39). The Size$_{Max}$ tree, with the lowest R^2 of .15, splits solely on ψ_{Sky}. This single split creates very uneven terminal node sample sizes with a majority

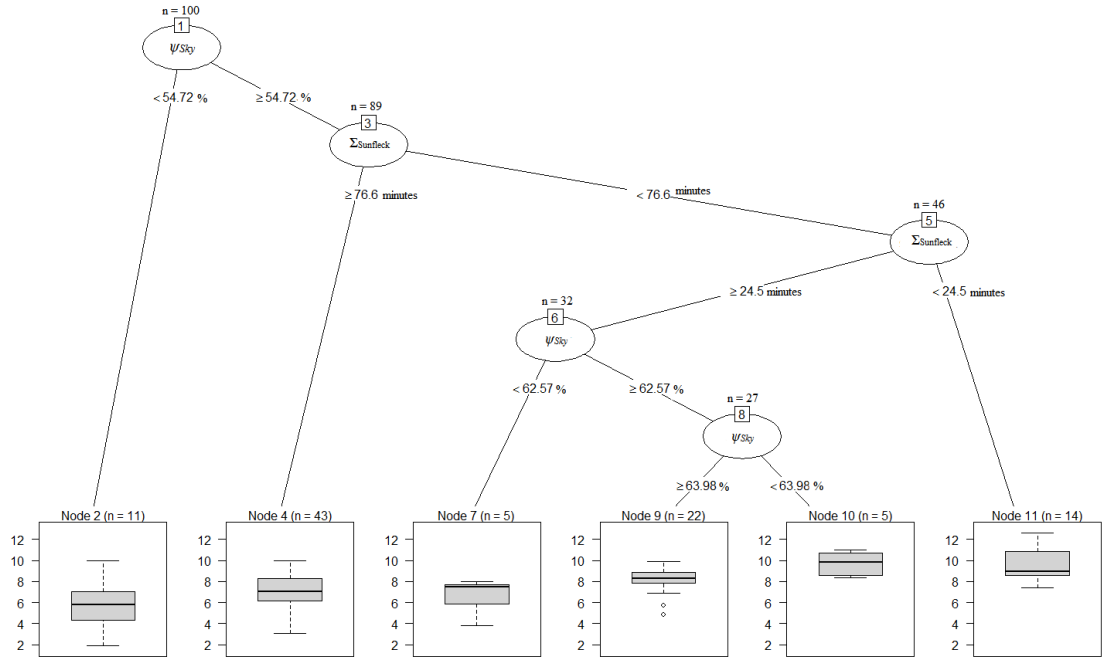


Figure 38. Pruned regression tree for Size$_{Mean}$ for Jan2015 at the North Site with boxplots showing terminal node distributions. For each boxplot the bold line represents the median, the box represents the interquartile range, and the whiskers represent 1.5x the interquartile range. Dots represent outlier values.

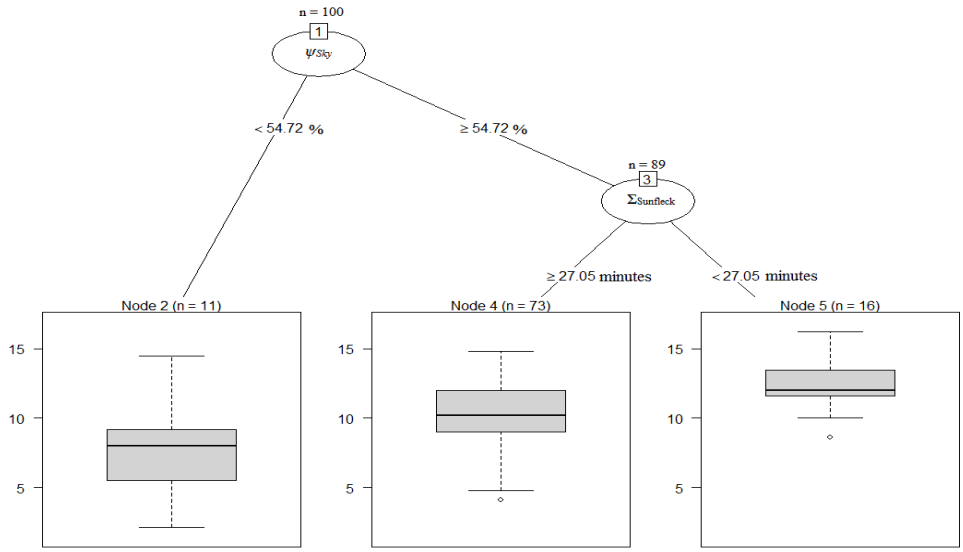


Figure 39. Pruned regression tree for Size$_{90th}$ for Jan2015 at the North Site with boxplots showing terminal node distributions. For each boxplot the bold line represents the median, the box represents the interquartile range, and the whiskers represent 1.5x the interquartile range. Dots represent outlier values.

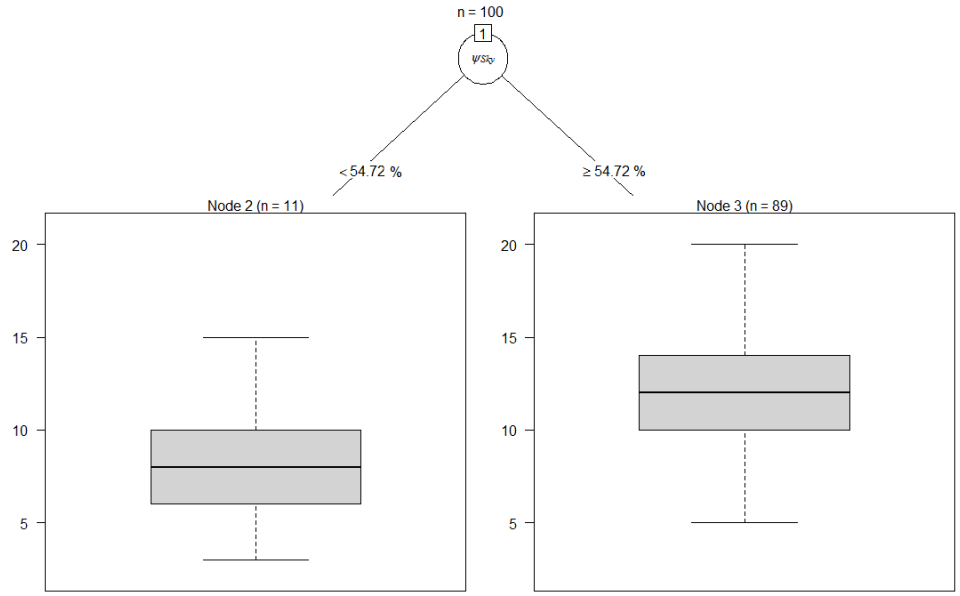


Figure 40. Pruned regression tree for $Size_{Max}$ for Jan2015 at the North Site with boxplots showing terminal node distributions. For each boxplot the bold line represents the median, the box represents the interquartile range, and the whiskers represent 1.5x the interquartile range. Dots represent outlier values.

of observations having values above the splitting threshold. This split does indicate larger ψ_{Sky} is associated with larger surface hoar (Fig. 39).

4.4.2.5 Jan2015 South Site Pruned regression trees for Jan2015 at the South Site contain the most splits for any event (Figs. 41-43). Between 51% and 61% of the variation is explained by these trees which rivals any other pruned regression trees (Table 16). All trees produce an initial split on ψ_{Sky} with larger ψ_{Sky} associated with larger surface hoar. Subsequent splits are made on ψ_{Sky} and $\Sigma_{Shortwave}$. Smaller ψ_{Sky} values are associated with smaller surface hoar. When ψ_{Sky} is between ~45% and 60%, surface hoar size is then determined by $\Sigma_{Shortwave}$. Larger surface hoar is associated with lower $\Sigma_{Shortwave}$ for this ψ_{Sky} range.

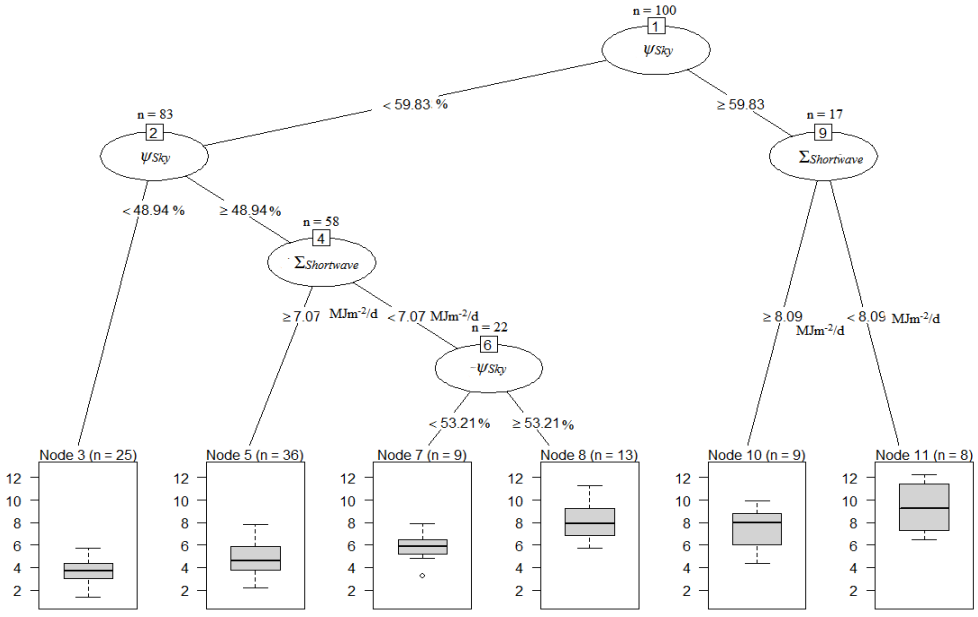


Figure 41. Pruned regression tree for Size$_{Mean}$ for Jan2015 at the South Site with boxplots showing terminal node distributions. For each boxplot the bold line represents the median, the box represents the interquartile range, and the whiskers represent 1.5x the interquartile range. Dots represent outlier values.

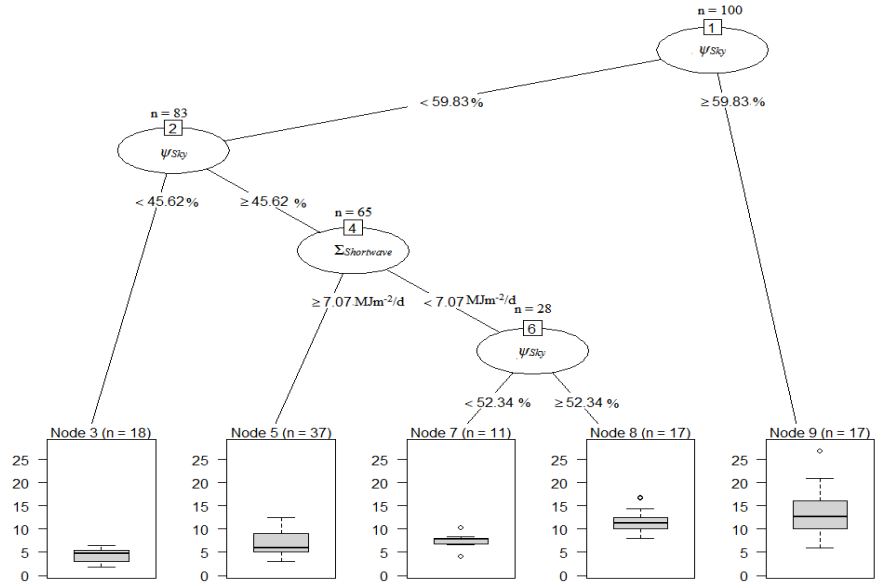


Figure 42. Pruned regression tree for Size$_{90th}$ for Jan2015 at the South Site with boxplots showing terminal node distributions. For each boxplot the bold line represents the median, the box represents the interquartile range, and the whiskers represent 1.5x the interquartile range. Dots represent outlier values.

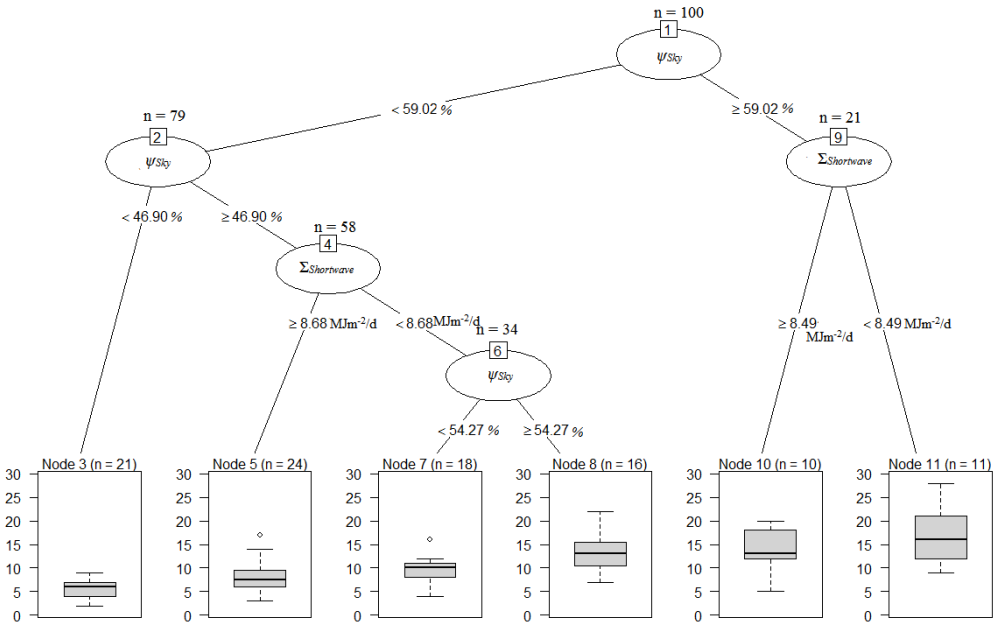


Figure 43. Pruned regression tree for $Size_{Max}$ for Jan2015 at the South Site with boxplots showing terminal node distributions. For each boxplot the bold line represents the median, the box represents the interquartile range, and the whiskers represent 1.5x the interquartile range. Dots represent outlier values.

4.4.2.6 Regression Tree Summary Pruned regression trees for each date and each sizing measure have a wide range of explanatory power. Overfit regression trees exhibit R^2 values ranging from .27 to .66. Pruned trees exhibit R^2 values between .15 and .61 depending on location, event, and sizing measure (Table 16). Several instances are found to have no splits using the 1-standard error rule after cross-validation. For trees that produce splits, split criteria and/or thresholds vary between events at the same plot, between sizing measures for a single event at a single plot, and between plots for the same event. However, trees generally split on ψ_{Sky}, $\Sigma_{Shortwave}$, or both parameters. For most instances, larger surface hoar is associated with higher ψ_{Sky} and lower $\Sigma_{Sunfleck}$ or $\Sigma_{Shortwave}$. Smaller surface hoar is associated with lower ψ_{Sky} and higher $\Sigma_{Sunfleck}$ or $\Sigma_{Shortwave}$.

Table 16. Summary of cross-validated regression tree results with R^2 values and splitting parameters.

Event-Site	Location	R^2	Split Parameters
Jan2014-North Site	$Size_{Mean}$	No split	n/a
	$Size_{90th}$	No split	n/a
	$Size_{Max}$	No split	n/a
Jan2014-South Site	$Size_{Mean}$	.29	$\Sigma_{Shortwave}$
	$Size_{90th}$	.27	$\Sigma_{Shortwave}$
	$Size_{Max}$	.24	$\Sigma_{Shortwave}$
April2014-South Site	$Size_{Actual}$	No split	n/a
Jan2015-North Site	$Size_{Mean}$	.38	ψ_{Sky} , $\Sigma_{Sunfleck}$
	$Size_{90th}$	.22	ψ_{Sky} , $\Sigma_{Sunfleck}$
	$Size_{Max}$	.15	ψ_{Sky}
Jan2015-South Site	$Size_{Mean}$	.61	ψ_{Sky} , $\Sigma_{Shortwave}$
	$Size_{90th}$	.55	ψ_{Sky} , $\Sigma_{Shortwave}$
	$Size_{Max}$	.51	ψ_{Sky} , $\Sigma_{Shortwave}$

4.5 Spatial Analysis

To examine the spatial structure of surface hoar size for each event, I created robust sample semi-variograms. Prior to creation, I created kriging surfaces of each sizing measure to qualitatively examine for evident trends. Sample days with missing observations provide little use as a large portion of the interpolated areas are based on distant values. I assessed stationarity by testing for linear trends in a regression analysis. If significant linear trends were found, I detrended the dataset. I then created robust semi-variograms for each sizing measure, location, and date. I attempted to fit spherical semi-variogram model structures each semi-variogram to extract lag distances.

I tested for linear trends to assess the assumption of stationarity in the data. For each separate event and each sizing measure, I ran a robust linear regression on the spatial coordinates to access cross-slope and up-slope linear trends. Origins of the x- and y- axes are in the south-west corner of each plot and are positive moving north and east

from this point. The x-axis corresponds with cross-slope trends and the y-axis corresponds with up-slope trends at the South Site and down-slope trends at the North Site.

No significant linear trends are found at the North Site for the Jan2014 event (Table 17). At the South Site, significant positive linear trends are found in the up-slope and cross-slope directions for all sizing measures. Trend coefficients imply surface hoar becomes larger moving up-slope and to the east. Linear trends account for 31% to 41% of the variation at the site. A significant negative linear trend is found for the Jan2015 event in the cross-slope direction. This implies surface hoar was largest at the western side and decreased moving east. Significant trends are found for the Jan2015 event, but only at the North Site. These trends explain a very small amount of the variability. A significant positive down-slope trend is found for $Size_{Mean}$ and significant cross-slope trends are found for $Size_{90th}$ and $Size_{Max}$. No significant trends are found for the Jan2015 event at the South Site.

Table 17. Regression coefficients from linear trend analysis. Bold represents a significant (p-value ≤ 0.05) result.

Event-Site	SH Size	$ß_0$ (X coordinate)	$ß_1$ (Y coordinate)	R^2
Jan2014-North	$Size_{Mean}$	0.00	0.00	0.05
	$Size_{90th}$	0.00	0.00	0.06
	$Size_{Max}$	0.00	0.00	0.04
Jan2014-South	$Size_{Mean}$	**0.01**	**0.03**	0.41
	$Size_{90th}$	**0.01**	**0.03**	0.31
	$Size_{Max}$	**0.01**	**0.03**	0.31
April2014-South	$Size_{Actual}$	**-0.01**	0.00	0.33
Jan2015-North	$Size_{Mean}$	0.00	**0.03**	0.07
	$Size_{90th}$	**0.01**	0.03	0.07
	$Size_{Max}$	**0.01**	0.00	0.07
Jan2015-South	$Size_{Mean}$	0.00	0.00	0.01
	$Size_{90th}$	0.00	0.00	0.04
	$Size_{Max}$	0.00	0.00	0.00

I created robust sample semi-variograms from either the sampled data, or detrended data if a significant trend was present. I fit spherical models to the semi-variograms if the models appeared to be an appropriate fit. Only seven out of thirteen semi-variograms indicate that a spherical model would be an appropriate fit. Of those semi-variograms that did not exhibit a spherical structure, other un-bounded models (e.g. Linear, Exponential) appear to be a better fit. The semi-variograms not fit by spherical models indicate ranges may be longer than the examined range of 25 meters or the process was not stationary (Kronholm, 2004).

Only two semi-variograms for the Jan2014 event are fit with spherical models (Figs. 44 and 45). Both instances are at the South Site using the $Size_{Mean}$ and $Size_{Max}$ sizing measures. Both models exhibit a range of 21 m.

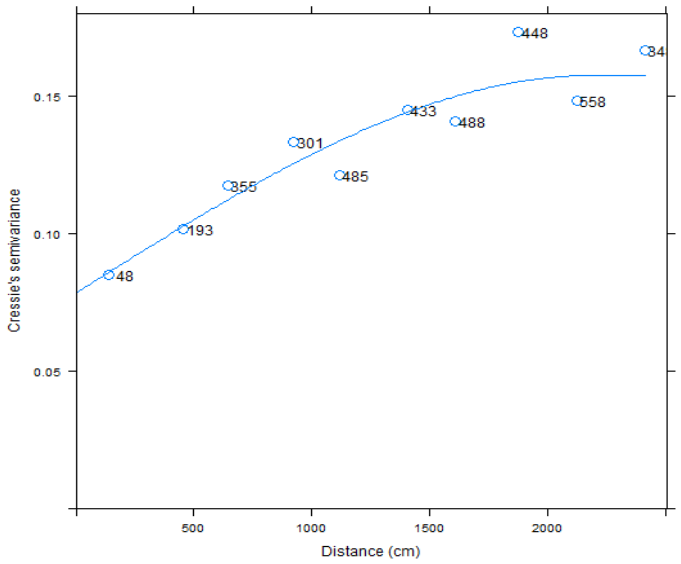


Figure 44. Sample and model semi-variograms for $Size_{Mean}$ for the Jan2014 event at the South Site.

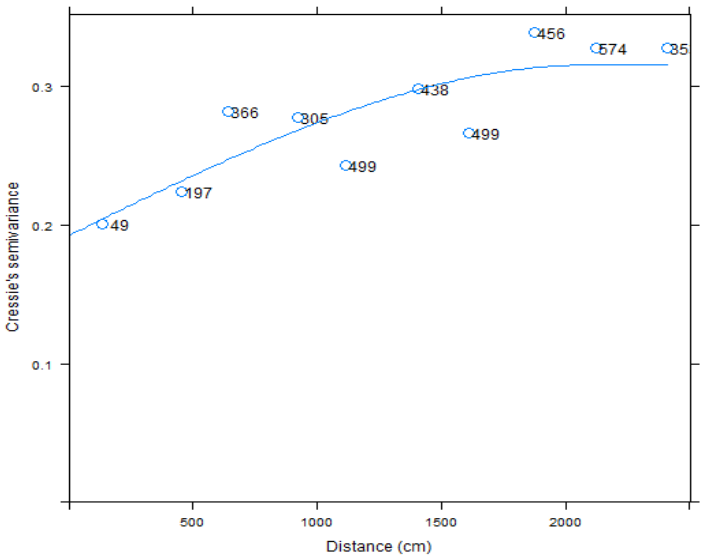


Figure 45. Sample and model semi-variograms for Size$_{Max}$ for the Jan2014 event at the South Site.

All sizing measures for the Jan2015 event at the North Site are fit with a spherical semi-variogram model. The Size$_{Mean}$ and Size$_{90th}$ semi-variograms exhibit ranges of 23 m and 24 m respectively, which are close to the Jan2014 event distances (Figs. 46 and 47). The Size$_{Max}$ semi-variogram exhibits a range of 7.8 m, the smallest range found in analysis (Fig. 48). While visually this semi-variogram may be fit with a better model, the least-squares algorithm I used for semi-variogram creation did not allow for this. Spherical models fit to the South Site size measures of Size$_{90th}$ and Size$_{Max}$ exhibit similar ranges of 22 m (Figs. 49 and 50).

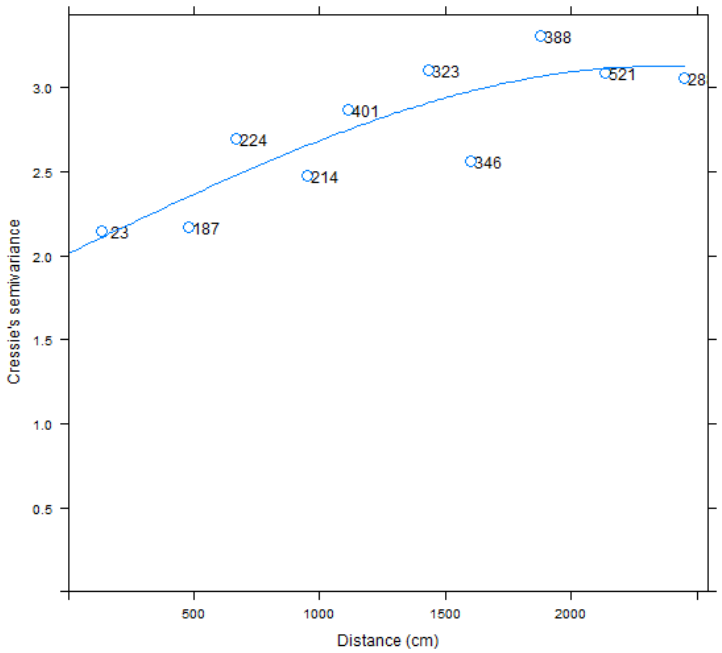


Figure 46. Sample and model semi-variograms for Size$_{Mean}$ for the Jan2015 event at the North Site.

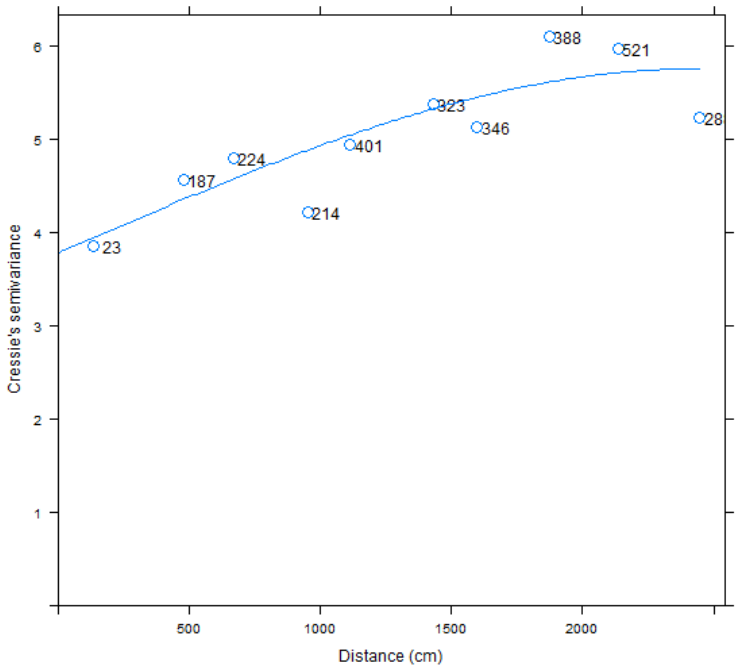


Figure 47. Sample and model semi-variograms for Size$_{90th}$ crystal size for the Jan2015 event at the North Site.

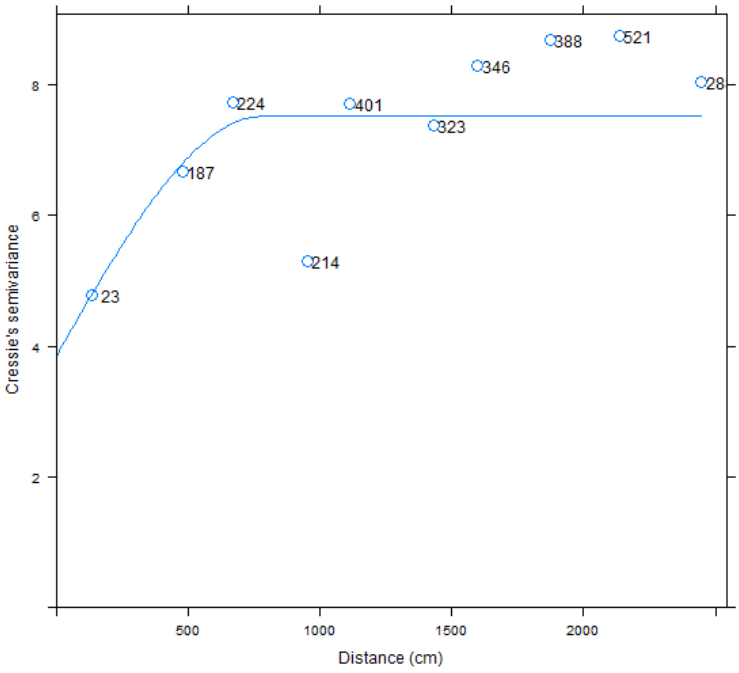


Figure 48. Sample and model semi-variograms for $Size_{Max}$ crystal size for the Jan2015 event at the North Site.

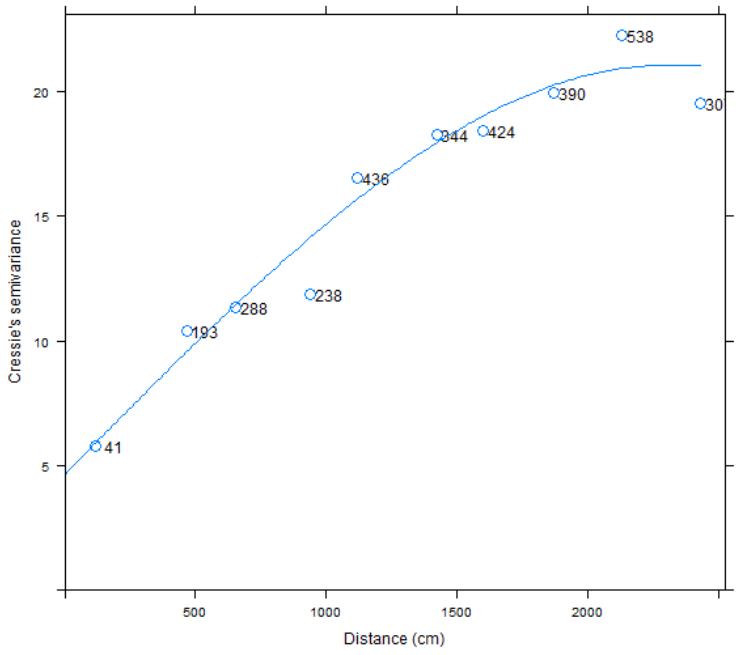


Figure 49. Sample and model semi-variograms for $Size_{90th}$ for the Jan2015 event at the South Site.

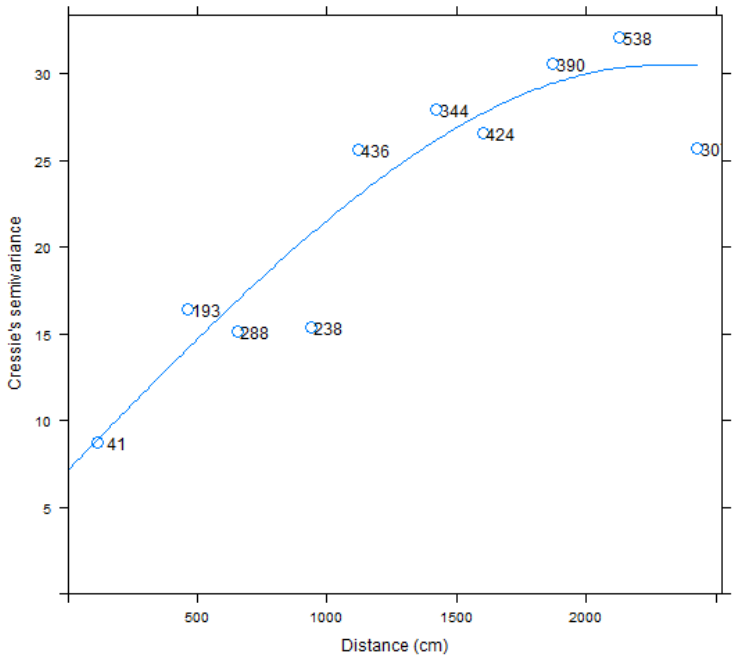


Figure 50. Sample and model semi-variograms for $Size_{Max}$ for the Jan2015 event at the South Site.

Overall, ranges from all but one spherically fit model are similar and fall between 21 m and 24 m (Table 18). An anomaly is found for the Jan2015 north event for $Size_{Max}$ and may be present due to a poor model fit. When appropriate, semi-variograms models in gstat are fit using a least-squares reduction method and initial starting values. While the initial starting value for the range estimate was set much higher for this semi-variogram, the least-squares method 'fit' this model to the one shown. A visual model fit places the range at 15 m which is closer to other model ranges but increases the sum of squares error. Visual model fitting in other R packages did not work. Any interpretations from this result should be done with caution and noted that the range may not be well defined.

Table 18. Extracted semi-variogram model measures for spherical model fits.

Event-Site	Summary	Model	Nugget	Sill	Range (m)
Jan2014-South	$Size_{Mean}$	Spherical	0.06	0.15	21
	$Size_{Max}$	Spherical	0.19	0.31	21
Jan2015-North	$Size_{Mean}$	Spherical	2.0	3.0	23
	$Size_{90th}$	Spherical	3.8	5.6	24
	$Size_{Max}$	Spherical	3.9	7.3	7.8
Jan2015-South	$Size_{90th}$	Spherical	5	20	22
	$Size_{Max}$	Spherical	7	30	22

5. DISCUSSION

This study investigates environmental associations and spatial patterns of surface hoar crystals for multiple formation events across two small, approximately north and south aspect meadow openings. These events are analyzed using multiple statistical methodologies to examine several known environmental influences on surface hoar formation and to explore the spatial patterns of surface hoar size. For an understanding of buried surface hoar patterns, crystal formation and subsequent destruction mechanisms must be known (Feick et al., 2007). As each factor may have considerable effects on the distribution of a layer, this study focuses on surface hoar layers directly after formation and before potential destruction in an attempt to separate the two periods.

Snow cover in forested areas is strongly affected by the surrounding tree canopy and the altered meteorological conditions that forests influence. A complex radiation balance is created in forests with reduced longwave emissions to the atmosphere, increased longwave emissions from trees, and decreased absorbed shortwave radiation from shading. Snow surface cooling is strongly affected by these altered radiation balances and subsequent surface hoar formation may be altered depending on the magnitude and duration of each on the snow surface. Determination of these complex radiation balances are difficult for field observers and proxies, based on physical processes, are used to assist in the delineation of areas that harbor larger surface hoar. This study examines how the amount of area open to the sky (as a proxy for longwave emission) and shading (as a proxy for absorbed solar radiation) influence surface hoar size.

Snowpack layers vary throughout space since the mechanisms responsible for formation and further metamorphism are different and continuously changing. Processes that are responsible for the formation of weak layers such as surface hoar vary depending on the observed scale. For slope-scale surface hoar observations, a quantification of this variability allows for insight into how surface hoar layers change over space and if the variability is random or exhibits spatial structure. Through the use of semi-variograms, I examine the spatial patterns of surface hoar for multiple events in two meadow openings.

5.1 Environmental Determinants of Surface Hoar Size

In this section, I discuss initial data exploration using scatterplots and correlation analyses. I then discuss the results of the regression analyses specific to each study site and date.

Several environmental determinants are significantly correlated with the surface hoar size measures (Table 6). Significant correlations are found only at the South Site for two events and change from radiation measures to ψ_{Sky} between the two dates. Both $\Sigma_{Sunfleck}$ and $\Sigma_{Shortwave}$ are negatively correlated for all size measures for the Jan2014 event (Table 6). Surface hoar size decreases with increasing $\Sigma_{Sunfleck}$ or $\Sigma_{Shortwave}$. These significant, weak correlations could be expected for a south facing site with forest shading. Surfaces that are shaded or receive less radiation are initially cooler going into the night and foster longer and more substantial growth periods. This supports work by Holler (2001) and Cooperstein (2008) who found warmer snow surface temperatures on southern aspects and decreased surface hoar crystal size when compared with northerly

slopes. These findings are attributed to differing radiation balances between the two aspects. For a south facing slope surrounded by forest, radiation differences will also be found across a site as shaded areas receive decreased amounts of shortwave radiation.

Significant positive correlations with ψ_{Sky} and all size measures are found at the South Site for the Jan2015 event. These correlations are similar in magnitude to correlations found by Shea (2011), but on an opposing aspect. For the North Site, ψ_{Sky} is not significantly associated with surface hoar size (Table 6). This is contrary to the significant associations Lutz (2009) found on a northeast aspect and Shea (2011) found on a north aspect. This can be partially attributed to the different slope angles these studies used. While Lutz (2009) used a site with slope angles ranging from 25-29°, my slopes are less inclined. A decreased slope angle on a northern aspect has a lower angle of incidence and more direct radiation. Forested north slopes at lower inclines also receive radiation over a greater area than slopes at steeper angles due to shading. Decreased slope angles also change ψ_{Sky} at the upper and lower portions of the meadow. For steeper slope angles and similar forest canopy, ψ_{Sky} will be smaller at the bottom of the slope when compared to the top. For lower angled slopes, a determination of the influence of ψ_{Sky} and $\Sigma_{Sunfleck}$ or $\Sigma_{Shortwave}$ on surface hoar size may be needed. The coupling of a shaded area with a large sky visibility for effective surface hoar growth is suggested by Gubler and Rychetnik (1991).

The lack of significant associations with ψ_{Sky} may be due to the heavily skewed distribution of ψ_{Sky} values. Although surface hoar sizes varied throughout each meadow, ψ_{Sky} values change very little throughout the open meadows. While ψ_{Sky} ranges from 27-

72%, both meadows exhibit most ψ_{Sky} values clustered near the maximum for each site (Tables 3, 4, and 5). Field observations indicated both meadows had large differences in ψ_{Sky} when moving throughout the sites. Only after hemispheric image analysis did it become apparent that ψ_{Sky} varied significantly less than what was thought to be observed. A similar clustering of values at the upper was also found for a similar sized meadow by Lutz (2009).

5.1.1 Jan2014 North Site

Derived ψ_{Sky} is not a significant determinant of surface hoar size for any size measure. Only one instance, at the north plot with the spatial error model, is this relationship found (Table 7). When accounting for $\Sigma_{Sunfleck}$ or $\Sigma_{Shortwave}$ and ψ_{Sky}, models moderately agree that at the site and south plot levels, an increase in ψ_{Sky} and a decrease in $\Sigma_{Sunfleck}$ or $\Sigma_{Shortwave}$ is associated with larger surface hoar (Table 11). At the site level, overfit regression trees also tend to agree with this result and show larger surface hoar is found with lower $\Sigma_{Sunfleck}$ and larger ψ_{Sky} (Appendix D). The absence of any regression tree splits within 1-standard error further emphasizes the lack of significant associations. The general absence of significant results, mainly for ψ_{Sky}, and inconsistency between analysis results is reason to believe that for this event, surface hoar size was controlled by other unmeasured factors such as incoming longwave radiation. The sunny day prior to formation and lack of snow on the tree canopy may have created varying amounts of emitted longwave radiation from differential heating of tree needles and trunks that could not be sufficiently modeled for the site. This hypothesis is weakly supported by the few significant multiple regression results at the south plot for all regressions and north plot.

These findings are not consistent with the somewhat similar work of Lutz (2009) and Shea (2011). This study site is at a relatively low slope angle and while it is north facing, the radiation differences between this and a much steeper north facing site are different. A few multiple regression results do support the hypothesis of Gubler and Rychetnik (1991) of a relationship of between ψ_{Sky} and $\Sigma_{Sunfleck}$ or $\Sigma_{Shortwave}$ with surface hoar crystal size. The inconclusive nature of these results warrants further study.

5.1.2 Jan2014 South Site

No single environmental measure is related to surface hoar size at the South Site. These results contrast the significant findings from the correlation analysis (ψ_{Sky} for the Jan2015 event; $\Sigma_{Sunfleck}$ and $\Sigma_{Shortwave}$ for the Jan2014 event) and may be a function of accounting for spatial autocorrelation in regression models. However, for $Size_{90th}$ and $Size_{Max}$, most multiple regression models show larger surface hoar is found in areas with greater ψ_{Sky} and lower $\Sigma_{Sunfleck}$ or $\Sigma_{Shortwave}$ at the site level (Table 12). Regression trees paint a different picture and indicate surface hoar size is mainly a function of $\Sigma_{Shortwave}$ (Figs. 35-37). However, in the overfit trees, ψ_{Sky} is the next splitting criterion (Appendix E). Regression tree R^2 values are quite low and indicate other factors may be contributing to the size differences. These results do follow the idea that snow surfaces that are shaded may be colder at the start of a formation period and overnight cooling is maximized by a larger sky visibility resulting in longer and more pronounced formation period where these factors coincide (Lutz, 2009; Cooperstein, 2008).

5.1.3 April2014 South Site

The environmental measure ψ_{Sky}, at the south plot, is the only single measure related to surface hoar size for this event (Table 8). Accounting for all factors, multiple regression models and regression trees do not provide any reasonable evidence that size is related to any environmental measures (Tables 11 and 16). These findings may arise from the lack of surface hoar size differences found at the site during sampling or the method of sizing for that day. The range of surface hoar sizes (where surface hoar was present) was only 3.25 mm and the mean size of 1.25 mm is very small (Table 4). This, coupled with no significant associations or significant linear trends indicate sizes for this event are mostly spatially continuous. Even though crystal sizes for this event are small, smaller crystals sitting on crust layers at southern sites have been shown to produce similar results in stability tests (Horton et al., 2013). Buried crusts were found at this study site for this event and a crust was the formation surface for the Jan2014 event.

This is the only event where surface hoar was not found at all sample locations. Seventeen locations, mainly clustered in the northern portion of the meadow, exhibited very small near surface facets or decomposing surface forms. The lack of crystal growth in these areas may indicate the overnight cooling of the snow surface was severely inhibited by the warm, highly solar affected up-slope trees. As sampling occurred in late April, heating of tree trunks and canopy needles was near the maximum that would be seen for the winter season. However, snow covering the tree canopy should have hindered canopy warming. Up-slope sample areas also received the greatest amount of solar radiation for the entire site. One or both factors may have contributed to the lack of

surface hoar but does not completely explain the absences. Other areas at similar distances from upslope trees that received the same or greater incoming solar radiation contained surface hoar crystals.

5.1.4 Jan2015 North Site

A significant positive relationship with ψ_{Sky} is found at the south plot for $Size_{Mean}$ and at the site level for $Size_{Max}$ (Table 9). With the tree canopy mostly covered in snow, relationships at the north plot would seem plausible. Even with a major portion of the tree canopy covered by snow which likely resulted in lower total long wave emissions, relationships with ψ_{Sky} are lacking. However, when accounting for ψ_{Sky} with $\Sigma_{Sunfleck}$ or $\Sigma_{Shortwave}$, models generally agree that larger ψ_{Sky} and smaller $\Sigma_{Sunfleck}$ or $\Sigma_{Shortwave}$ were associated with larger surface hoar sizes. This relationship is evident at the site and south plot levels. Regression trees show similar results with larger ψ_{Sky} and lower $\Sigma_{Sunfleck}$ associated with larger surface hoar (Figs. 38-40). For all but the lowest ψ_{Sky}, lower $\Sigma_{Sunfleck}$ is associated with larger surface hoar. For the $Size_{Max}$ regression tree, this secondary split on $\Sigma_{Sunfleck}$ is subsequently pruned away after cross-validation. The lack of significant relationships from analyses with multiple explanatory variables at the north plot may be due to increased longwave emissions from increased tree canopy warming as the upper portions of trees were free of snow, likely from melting. This hypothesis is supported by the multiple significant relationships at the south plot while the north plot has none. With a lack of individual relationships and findings in the multiple regression analyses, support is further added for Gubler and Rychetnik's (1991) assertion.

5.1.5 Jan2015 South Site

Interestingly, several relationships are found at the South Site. Regression models for $Size_{90th}$ and $Size_{Max}$ generally show a positive relationship between ψ_{Sky} at all extents (Table 10). Multiple regression results also reveal a positive relationship with ψ_{Sky} although a relationship with $\Sigma_{Sunfleck}$ or $\Sigma_{Shortwave}$ is generally lacking (Table 15). The strong relationships with ψ_{Sky} may be caused by decreased canopy warming due to recent snow events covering canopy needles. However, with probable decreased longwave emissions from the canopy, this result should have been observed at the north plot. The high R^2 regression trees paint a different picture and indicate relationships for this event are complex and potentially non-linear (Figs. 41-43). Regression trees contain more splits and terminal nodes after cross-validation than any other event or site. These regression trees indicate that while larger surface hoar is found for larger ψ_{Sky} and vice-versa, between a threshold for ψ_{Sky}, the controlling factor is $\Sigma_{Shortwave}$. For large ψ_{Sky} areas, which are in the middle of the site and furthest from any trees, size may be mainly controlled by longwave losses. Areas with decreased ψ_{Sky} are found closer to warm trees in up-slope areas and shaded portions in downslope areas. In both areas, surface hoar size may be affected by absorbed radiation. This complex relationship cannot be modeled using linear regression and may be a reason that linear models did not find relationships with $\Sigma_{Sunfleck}$ or $\Sigma_{Shortwave}$.

5.2 Spatial Structure

I analyzed for linear trends in the size measures prior to semi-variogram creation. I used this process to identify linear trends and if present, correct for these trends to satisfy the assumption of stationarity. While initially considered an intermediate analysis, I noted several interesting trends. For the Jan2014 event at the North Site, April2014 event, and Jan2015 event at the South Site, I found weak to no trends which explain little of the site variation (Table 6). However, the Jan2014 event at the South Site exhibits significant trends for all three size measures. The positive trends (from the plot origin) explain between 31% and 41% of the variation at the site. Significant linear trends for studies measuring shear strength on buried surface hoar layers have been observed although the strength of these trends was considerably lower (e.g. Kronholm, 2004; Logan, 2005). Trends for this event indicate surface hoar is smallest in the southwest corner of the site and becomes increasingly larger moving to the north and east. The coefficient for the y-coordinate is larger than the x-coordinate indicating the surface hoar grew larger more rapidly moving up-slope than cross-slope. Changes in ψ_{Sky} over the site may partially explain this result in the lower portion of the slope but not in upper areas as ψ_{Sky} begins to lower after reaching the middle of the meadow when moving up-slope. A potential cause may be a small opening which connects the meadow with a neighboring meadow and is adjacent to the north-east corner of the site. This corridor may have altered wind or temperature patterns for nearby locations which would influence latent heat fluxes and/or mass deposition rates (Colbeck, 1998; Feick et al., 2007). The corridor may have led to accelerated surface winds when moving through this small opening,

altering near surface conditions. Prevailing west winds likely move from the southwest meadow opening to the northwest opening. As Feick (2007) suggests, reliably predicting surface hoar growth is difficult unless local winds speeds are known. Without any anemometers at the sites, I cannot determine if winds were present during formation periods.

Semi-variogram analysis after significant linear trend removal reveals a variety of spatial structures in the residuals. Spatial autocorrelation is evident in all semi-variograms but the nature of this autocorrelation changes based on event, site, and sizing measure (Appendix B). Semi-variograms that appear bounded and fit with spherical models display ranges between 21 m and 24 m except for the $Size_{Max}$ size measure at the North Site for the Jan2015 event (Table 18 and Figs. 44-50). This low range of 7.8 m is closer to autocorrelation ranges for weak layer heights that Lutz (2009) found. However, this range is substantially lower than other ranges found in this study. Excluding this single low finding, calculated ranges are mostly consistent between sites on the same event (Jan2015) and also between events at a site (South Site). While autocorrelation ranges are consistent, crystal size measures for these ranges vary. The $Size_{Max}$ measure is fit with a spherical model for three different events while $Size_{Mean}$ and $Size_{90th}$ are only fit with spherical models for two events. These differences are potentially due to the representativeness of the size measures which is discussed below in section 5.6. Shea and Jamieson (2010b) also noted widely varying semi-variograms that changed between sample days and postulate that the process scale varied between events at a single site

while also varying between sites. I too found similar results and varying process scales for events may help to explain these differences.

For several semi-variograms which are not well fit with a spherical model, unbounded linear models appear to be a potential fit (Appendix B). These semi-variograms show a continually increasing variance that increases beyond the chosen lag distance. These models indicate autocorrelation ranges may be larger than the meadow sizes. Also of note are four semi-variograms where the first lag bin contains a relatively high semi-variance as compared to the next bin size. Kronholm (2004) also found a similar structure for a buried layer of surface hoar but was unsure of the cause. For my study, no explanation is readily evident. Interestingly, for the lag bins where this occurred, the bin size is less than the 30 point-pair threshold that is suggested by Journel and Juijbregts (1978) and may not sufficiently represent shorter lag distances. Also, these short distances are mostly made from point-pairs combinations between gridded and random points. While durantions between sampling a gridded point and a random point were at most one hour, changes in size may have occurred which increased this short distance variance. Kronholm (2004) hypothesizes that spatially continuous, low variability surface hoar layers are deposited with an absence of wind when observed at spatial scales over 1 m, but for scales below 1 m, this may not be true. Again, wind conditions are unknown for any of my formation events but the large variance observed in the short point-pair distances adds support to Kronholm's (2004) hypothesis.

A lack of samples at distances under 1 m is also a potential cause for absences of spherical spatial structures in several semi-variograms (Appendix B). As the goal of my

sampling scheme was to sample an entire meadow with a gridded layout and collect any remaining points as random, this procedure affected semi-variogram analyses. As the South Site is smaller than the North Site, I was able to collect more random points at this site. A greater number of shorter distance point pairs was calculated due to random points falling within 2.5 m of a gridded point. This led to a greater sampling density of the smaller scale variability at the South Site which may have affected semi-variograms. This also resulted in lag bins that did not adequately meet the suggested 30 point-pair minimum. As others have found buried layer heights of surface hoar to exhibit autocorrelation ranges that are under 5 m (e.g. Lutz, 2009), a sampling plan that incorporates a greater amount of short distance (< 5 m) point-pairs would improve semi-variogram analysis. Sampling only a single meadow opening as opposed to two meadows during a sampling day allows for more sample points, more point-pairs combinations, and a greater distribution of point-pair distances. Careful attention to the measurement spacing should be one of the primary factors when considering future sampling plans.

5.3 Conceptual Model

Based on previous findings, I created a conceptual model with a goal of providing backcountry users and forecasters a tool to implement when targeting buried layers of surface hoar in the backcountry (Fig. 51). This simplified abstraction of reality aims to provide a starting point for slope assessment or guidance in travel around slopes with potential or known buried surface hoar layers. This model attempts to provide a basic

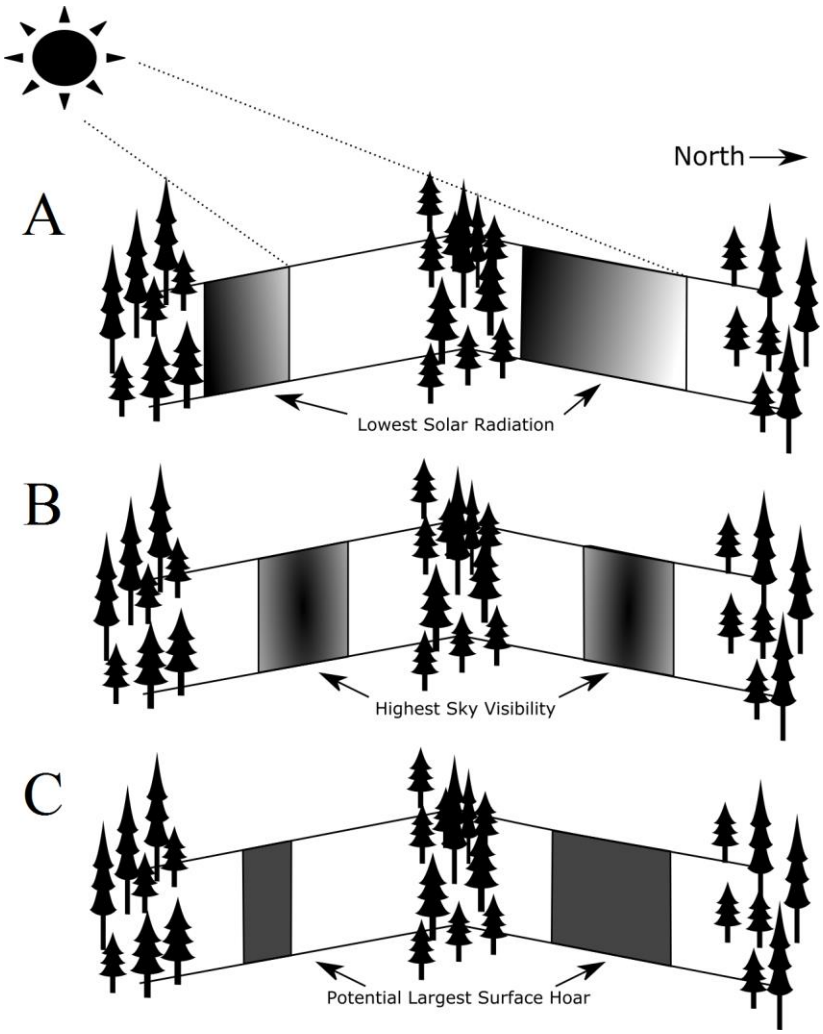


Figure 51. Conceptual model of north and south facing slopes showing differences in (A) solar radiation, (B) sky visibility, and (C) surface hoar size.

understanding of potential slope-scale surface hoar conditions at similar meadow openings.

For northerly and southerly facing slopes that receive some amount of direct solar radiation, the largest surface hoar may be found in areas that receive the lowest amount of radiation (more shaded) but also contain the largest unobstructed view to the sky (Fig. 51). For southerly aspects, this area coincides slightly down-slope of the middle of the

meadow. For northerly aspects, this area is may be more oriented in middle to up-slope areas. Lutz (2009) proposed a similar model for northeast and southern aspects. While the areas defined for higher and lower sky visibility and radiation are similar, Lutz (2009) attributes any solar radiation on a southern aspect as a destructive mechanism and does mention any potential inhibition of surface hoar growth. As this is certainly probable, a consideration of the effects of shading on the growth of crystals must also be considered. Any differences from the effects of radiation during growth will only be further increased with possible radiative destruction. Shaded portions of the slope will change depending on the time of year as solar elevation angles alter the radiation characteristics of a meadow.

While this study partially supports these ideas, the amount of unexplained variability at each study site and varying results indicate spatial patterns may be more complicated. Also, patterns of surface hoar may depend on parameters that were not investigated and varies between events, even at the same area. Factors that may lead to changing surface hoar patterns in meadow openings during formation are the presence of snow on the surrounding canopy (Adams et al., 2011), cloudy conditions prior or during formation (Lang et al., 1984; Cooperstein, 2008), or variable wind conditions (Feick et al., 2007).

5.4 Site Comparisons

While study sites were placed as close together as possible, I did not attempt comparisons between sites for an event as this is an observational study and differences

in meteorological conditions during formation or other site specific effects may be a cause of any differing results. It is still interesting to note that similar to Cooperstein (2008), I generally saw smaller surface hoar sizes at the South Site when compared to the North Site for an event. The Jan2014 median crystal size for all crystals from the North Site (median= 4 mm) is significantly larger than South Site (median= 2 mm) (Mann-Whitney U test, $p < 0.01$). Similar to the previous event, the Jan2015 median crystal size for all crystals from the North Site (median= 8 mm) is significantly larger than the South Site (median=4 mm) (Mann-Whitney U test, $p < 0.01$). While this follows previous research, the reasons for this finding are not easily discernable. As I only measured air temperature and relative humidity (measured at ~1.5 m height) during a formation period, these are the only comparable meteorological measurements. Air temperatures at the sites were within 1° C in the early afternoon of January 24th, 2014. In the early evening, temperatures began dropping with the North Site temperature lowering more rapidly than the South Site. Cooling at the North Site continued until reaching a minimum of -8° C at 02:45 the next morning. The South Site also continued cooling overnight and reached a minimum temperature of -7° C at midnight. This site warmed slightly to -5° C and held this temperature until the next morning. The relative humidity at the North Site started at ~70% and slowly increased into the morning hours to a maximum of ~90%. The southern site started lower (~60%) and plateaued early in the formation period at a maximum near 80%. Crystal size differences may be due to the colder and longer formation period with a higher relative humidity. Feick et al. (2007) found differing latent heat fluxes, due to differences in temperature, relative humidity, and wind speeds, were a cause of crystal

size differences. They mainly attributed this to wind and postulated that for complex areas, similar to my study sites, reliably predicting surface hoar is nearly impossible unless localized wind measurements at a scale smaller than 10 m is known. For this study, the differences in relative humidity and temperature may have been a controlling factor, but the unknown effect from winds may have also contributed. The unmeasured wind speeds at the sites during formation periods were potentially a driver of size differences. Incorporation and comparison of local winds speeds at a scale <10 m would allow a more detailed analysis. Measuring surface temperatures and calculating vapor pressure gradients would allow for better comparisons, similar to ones by Cooperstein (2008).

5.5 Event Comparisons

Differences between events are not quantitatively compared as site characteristics and meteorological conditions were different for each formation event. While it is tempting to use a proportional measure to compare the regression models from each event, the relationship between the independent and dependent variables in a proportional analysis is typically sigmoidal which is better modeled with a logistic regression (Ramsey and Schafer, 2013). I do observe qualitative differences between events at each site. Size differences are evident when viewing boxplots and sizing measures between the Jan2015 and Jan2014 events. At the South Site, the mean crystal size for the Jan2015 event is nearly three times the mean crystal size for the Jan2014 event (Tables 3 and 5; Figs. 21 and 31). The North Site is less than double the mean size between the two events (Tables

3 and 5; Figs. 19 and 28). While $Size_{Max}$ for the Jan2015 event at the South Site is heavily influenced by the sporadic large crystals found at the South Site, it does contain several crystals that are larger than any found at the North Site. These large crystals may have initially grown above any surrounding crystals. Hachikubo and Akitaya (1997) note that a change in aerodynamic roughness as crystals grow upward causes an increase in the bulk transfer coefficient and increased condensation rates. This creates a feedback mechanism where crystals higher above the surface are in more saturated air which allows for accelerated growth. These larger crystals also create turbulence which enhances mixing of moist and dry parcels of air. This process would help to explain the larger crystals found protruding above all other crystals. Roughness lengths are also altered as feathery crystals growth from a smoother snow surface. This growth alters the near surface boundary air layer and turbulent heat fluxes, further affecting crystal formation (Armstrong and Brun, 2008)

Size differences between events are also likely to be caused by the different meteorological conditions that were present during formation. The Jan2015 formation period was colder with higher relative humidities that were present for longer periods of time as compared to the Jan2014 event. This may have led to larger and longer deposition rates. Influences by winds may have altered moisture availability and rates of latent heat fluxes.

5.6 Summary Measures

The use of $Size_{Mean}$ and $Size_{Max}$ in this study may not always adequately represent the crystal size at a sampled location, nor be of use when the surface hoar size is related to the more commonly used weak layer height after burial. As I counted every crystal at a sample point, very small crystals that were potentially covered by two larger crystals were used in the calculation of the mean and may have heavily influenced this size measure (Fig. 52). The influence of a very large number of identifiable, but insignificant small crystals would also skew this measure.

As samples were taken at a single point with a 2 cm^2 support, the use of $Size_{Max}$ may produce misleading results as it did not adequately represent an area larger than the sampled area. A bias is evident for the Jan2015 event at the South Site as I included some of the sporadic large crystals during sizing. Once buried, these crystals would most likely be covered to a depth that was determined by a denser collection of crystals where an

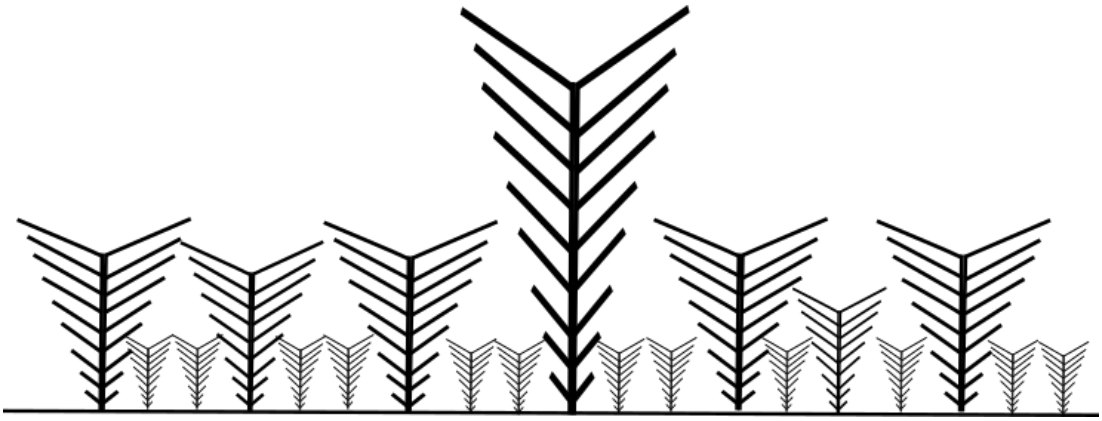


Figure 52. Hypothetical example of a sampled area. The large number of small crystals would skew the distribution of $Size_{Mean}$ and the lone large crystal would skew distribution of $Size_{Max}$.

'umbrella' effect is more evident (Davis et al., 1996). A better determination of $Size_{Max}$ would include taking multiple measurements surrounding a given sample point to better characterize the maximum crystal size and avoid any biases from unusually large and infrequent crystals. A focus on crystal size and density relations to weak layer height is recommended for future work. As sampling depends on a study's goal, there is no single correct method to characterize each sample point or area.

5.7 Inferences and Uncertainty

As this observational study did not have control over group assignments, no causal inferences between the environmental determinants can be made. One goal was to show that "A is associated with B" not "A causes B". Clearly ψ_{Sky} does not cause larger surface hoar growth, but a larger ψ_{Sky} allows for greater radiative cooling which in turn cools the surrounding air. This is not the only physical process that determines surface hoar growth and therefore the sole use of a causality relationship is incorrect. While I incorporated random sampling into the study, not all measurements are considered random and any inferences drawn from this research and applied to areas outside of these meadows should be done cautiously.

6. CONCLUSION

I investigated three surface hoar events over the course of two winter seasons at two meadow openings in southwestern Montana. For each event, I collected and examined surface hoar crystals in each meadow prior to any destructive influences. Relationships between several environmental influences on surface hoar formation and surface hoar size were examined using correlation, linear regression, and regression tree analysis. I examined the spatial structure at each meadow for each event using several size descriptions of surface hoar.

Photographic records enabled the identification of three commonly used size descriptors of snow crystals. These size descriptions allowed for thorough and varied investigations into the influences that sky visibility, shading, and radiation have on surface hoar crystal size. The sampling scheme and sizing measures allowed for the description of the spatial structure for each event.

Relationships between surface hoar size and environmental metrics for an event vary between sites, and these relationships change between events. For meadow openings that experience direct solar radiation during the winter, the sole use of sky visibility for the determination of crystal size may not always be adequate, regardless of the amount of snow covering the surrounding trees. A careful evaluation of areas that are shaded but possess a high sky visibility is needed to help determine surface hoar size. The influence of emitted longwave radiation, which is difficult to estimate in the field, should not be ruled out. Areas that are near solar affected trees may contain smaller surface hoar and must be given special consideration. The influence of solar radiation should not strictly

be constrained to examinations into the destruction of surface hoar. While persistence of surface hoar may be greater in shaded areas, this effect may be exaggerated as these areas initially grew larger crystals.

The spatial structure of surface hoar varied depending on the size measure, event, and location. Significant slope-scale linear trends that explain a large amount of variability were only found for one event at one location. Spatial autocorrelation lengths extracted from spherical semi-variogram models ranged from 7.8 m to 25 m. Several semi-variograms indicated spatial autocorrelation distances greater than 25 m. These varying spatial structures and autocorrelation lengths suggest that the processes responsible for the formation of surface hoar change between events at the same location and change depending on the location. These results may be influenced by the sampling scheme but do suggest conducting multiple weak layer investigations for slope evaluations in a meadow opening. These findings support prior research (e.g. Lutz 2009; Birkeland et al., 2010) that suggest any investigations into buried surface hoar layers should incorporate multiple measurements and avoid closely spaced tests. Choosing the placement for these investigations should incorporate a basic understanding of a slope's shading and skyview characteristics, but with an understanding that stochastic and unknown influences may have produced irregular spatial patterns.

Findings for this study are unique to the examined meadows and may differ depending on weather patterns, slope aspect, or other site specific conditions. Careful snowpack examinations in meadow openings when a buried surface hoar layer is present should take into account the site canopy characteristics along with slope aspect.

Seemingly uniform terrain may harbor large variations in surface hoar crystal sizes and point observations will likely not provide reliable information for the entire slope.

7. CHALLENGES AND FUTURE RESEARCH RECOMMENDATIONS

Throughout the course of this study and like many other *in-situ* snow studies, limitations and constraints were identified which should be addressed for future surface hoar research. Predictions and assessments of surface hoar days proved to be a difficult and costly endeavor. With limited nearby remote weather station access and potentially unknown overnight sky conditions, surface hoar event prediction was not easy. Assessing each potential surface hoar day become an expensive endeavor with the 1.5 hour drive and 20 minute snowmobile ride in. While this study attempted but did not find suitable sites closer to Bozeman, future studies should focus on areas that are more readily and easily accessed such as locations at local ski areas. Confidence in a forecasted day would be increased with a partial or full meteorological station placed at one of the sites and equipment malfunctions would be quickly noticed. Incorporation of a remotely accessed weather station at each site or by using sites that are within very short distances of weather stations that, at a minimum, measure temperature and relative humidity are needed.

While sizing surface hoar crystals on the surface provides a snapshot in time of the surface crystals, little was known about the specific surface conditions during formation. Differing crystal types will form with the probable differing temperature and supersaturation conditions across each slope and between events. While certain conditions favor needle type crystals, others produce the more classic ‘feathery’ crystals. Differing mass deposition rates may produce differing crystal shapes, sizes, and densities. Surface wind conditions likely played a role during all growth phases with changing

winds speeds and directions that were not measured. Incorporation of a high density meteorological measurement system across a slope is difficult, but would allow for better explorations into spatial patterns.

Sizing of surface hoar crystals may not always be analogous to the weak layer height which is typically used in analysis of buried layers. Future studies should attempt to measure both the crystal size and obtain a potential 'buried' height. Measurement support should be increased to better capture variations over small distances. Incorporation of crystal density measurements would give a better idea of deposited mass and how snowfall would cover this layer. Density measurements could also be coupled with rates of mass deposition in modelling studies (e.g. Adams et al., 2011). Field density measurements could be measured using 3-dimensional photogrammetry techniques and software such as Agisoft Photoscan (Agisoft LLC, 2015). Agisoft Photoscan creates a 3-dimensional model using a series of images taken of an object or area. Creating 3-dimensional crystal models similar to ones obtained from CT scans (Stanton et al., 2012) using field photography would allow for characterizations of crystal density, volume, and specific surface area.

REFERENCES CITED

Adams, E.E., Slaughter, A.E., McKittrick, L. and Miller, D.A., 2011. Local terrain-topography and thermal-properties influence on energy and mass balance of a snow cover. Annals of Glaciology, 52(58): 169-175.

Agisoft LLC, 2015. Agisoft Photoscan Professional edition, St. Petersburg, Russia. URL: http://www.agisoft.com/.

American Avalanche Institute, 2014. Level 2 course notebook. American Avalanche Institute, Victor, ID, pp. 43.

Armstrong, R.L. and Brun, E., 2008. Snow and climate : physical processes, surface energy exchange and modeling. Cambridge University Press, Cambridge, xxii, pp. 222.

Baunach, T., Fierz, C., Satyawali, P.K. and Schneebeli, M., 2001. A model for kinetic grain growth. Annals of Glaciology, Vol 32, 2001, 32: 1-6.

Birkeland, K.W., Chabot, D., 2006. Minimizing “false-stable” stability test results: why digging mor esnowpits is a good idea. Proceedings of the 2006 International Snow Science Workshop, Telluride, CO, USA, pp. 498-504.

Birkeland, K.W., Kronholm, K., and Logan, S., 2004a. A comparison of the spatial structure of the penetration resistance of snow layers in two different snow climates. Proceedings of the 2004 International Snow Science Workshop, Jackson Hole, WY, USA, pp. 216-222.

Birkeland, K.W., Kronholm, K., Schneebeli, M., and Pielmeier, C., 2004b. Changes in the shear strength and micro-penetration hardness of a buried surface-hoar layer. Annals of Glaciology, 38: 223-228.

Birkeland, K.W., Hendrikx, J. and Clark, M.P., 2010. On optimal stability-test spacing for assessing snow avalanche conditions. Journal of Glaciology, 56(199): 795-804.

Bloschl, G., 1999. Scaling issues in snow hydrology. Hydrological Processes, 13(14-15): 2149-2175.

Borish, M., Birkeland, K., Custer, S., Challender, S., Hendrikx, J., 2012. Surface hoar distribution at the scale of a helicopter skiing operation. Proceedings of the 2012 International Snow Science Workshop, Anchorage, AK, USA, pp. 1040-1046.

Breiman, L., Friedman, J.H., Olshen, R.A., Stone, C.J., 1984. Classification and regression trees. Chapman and Hall, New York, NY, pp. 358.

Breyfogle, S.R., 1986. Growth characteristics of hoarfrost with respect to avalanche occurrence. Proceedings of the 1986 International Snow Science Workshop, Lake Tahoe, CA, USA, pp. 216-222.

CAIC, 2014. Colorado Avalanche Information Center: Statistics and Reporting. Retrieved May, 2015. URL: http://avalanche.state.co.us/accidents/statistics-andreporting/.

Chalmers, T.S. and Jamieson, B., 2001. Extrapolating the skier stability of buried surface hoar layers from study plot measurements. Cold Regions Science and Technology, 33(2–3): 163-177.

Colbeck, S.C., 1988. On the micrometeorology of surface hoar growth on snow in mountainous area. Boundary-Layer Meteorology, 44(1-2): 1-12.

Colbeck, S., Jamieson, B. and Crowe, S., 2008. An attempt to describe the mechanism of surface hoar growth from valley clouds. Cold Regions Science and Technology, 54(2): 83-88.

Cressie, N.A.C., 1993. Statistics for Spatial Data. Revised edition. John Wiley and Sons, New York, pp. 900.

Cooperstein , M., 2008. The effects of slope aspect on the formation of surface hoar and diurnally recrystallized near-surface faceted crystals. M.S. thesis, Montana State University, Bozeman, MT, USA, pp. 169.

Davis, R., Jamieson, B., Hughes, J., Johnston, C.D., 1996. Observations of buried surface hoar - persistent failure planes in the Columbia Mountains of B.C.. Proceedings of the 1996 International Snow Science Workshop, Banff, AB, Canada, pp. 81-85.

Davis, R.R., Elder, K., 1994. Application of classification and regression trees: selection of avalanche indices at Mammoth Mountain. Proceedings of the 1986 International Snow Science Workshop, Snowbird, UT, USA, pp. 285-294.

Davis, R.E., Elder, K., Howlett, D. and Bouzaglou, E., 1999. Relating storm and weather factors to dry slab avalanche activity at Alta, Utah, and Mammoth Mountain, California, using classification and regression trees. Cold Regions Science and Technology, 30(1-3): 79-89.

Dormann, C.F., McPherson, J.M., Araujo, M.B., Bivand, R., Bolliger, J., Carl, G., Davies, R.G., Hirzel, A., Jetz, W., Kissling, W.D., Kuhn, I., Ohlemuller, R., Peres-Neto, P.R., Reineking, B., Schroder, B., Schurr, F.M. and Wilson, R., 2007. Methods to account for spatial autocorrelation in the analysis of species distributional data: a review. Ecography, 30(5): 609-628.

Essery, R., Pomeroy, J., Ellis, C. and Link, T., 2008. Modelling longwave radiation to snow beneath forest canopies using hemispherical photography or linear regression. Hydrological Processes, 22(15): 2788-2800.

Feick, S., Kronholm, K. and Schweizer, J., 2007. Field observations on spatial variability of surface hoar at the basin scale. Journal of Geophysical Research-Earth Surface, 112(F2).

Fierz, C., Armstrong, R.L., Durand, Y., Etchevers, P., Greene, E., McClung, D.M., Nishimura, K., Satyawali, P.K. and Sokratov, S.A. 2009. The International Classification for Seasonal Snow on the Ground. IHP-VII Technical Documents in Hydrology N°83, IACS Contribution N°1, UNESCO-IHP, Paris.

Frazer, G.W., Canham, C.D., and Lertzman, K.P., 1999. Gap Light Analyzer (GLA), Version 2.0: Imaging software to extract canopy structure and gap light transmission indices from true-color fisheye photographs. Copyright 1999: Simon Fraser University, Burnaby, B.C., and the Institute of Ecosystem Studies, Millbrook, New York.

Frazer, G.W., Fournier, R.A., Trofymow, J.A. and Hall, R.J., 2001. A comparison of digital and film fisheye photography for analysis of forest canopy structure and gap light transmission. Agricultural and Forest Meteorology, 109(4): 249-263.

Greene, E., Atkins, D., Birkeland, K., Elder, K., Landry, C., Lazar, B., McCammon, I., Moore, M., Scharaf, D., Sternenz, C., Tremper, B., and Williams, K., 2010. Snow, weather and avalanches: observation guidelines for avalanche programs in the United States. American Avalanche Association, Pagosa Springs, CO, USA, pp 152.

Gubler, H., 1984. Remote instrumentation for avalanche warning systems and snow cover monitoring. Proceedings of the 1984 International Snow Science Workshop, Aspen, CO, USA, pp. 137-142.

Gubler, H., 1998. A model to determine snow surface properties from remote measurements. Proceedings of the 1998 International Snow Science Workshop, Sunriver, OR, USA, pp. 35-48.

Gubler, H. and Rychetnik, J., 1991. Effects of forests near the timberline on avalanche formation. IAHS Publ. 205 (Symposium at Vienna 1991 – Snow, Hydrology and Forests in High Alpine Areas), pp. 19-38.

Hachikubo, A., 2001. Numerical modelling of sublimation on snow and comparison with field measurements. Annals of Glaciology, Vol 32, 2001, 32: 27-32.

Hachikubo, A. and Akitaya, E., 1997. Effect of wind on surface hoar growth on snow. Journal of Geophysical Research-Atmospheres, 102(D4): 4367-4373.

Hachikubo, A. and Akitaya, E., 1998. Daytime preservation of surface-hoar crystals. Annals of Glaciology, Vol 26, 1998, 26: 22-26.

Hardy, J.P., Melloh, R., Koenig, G., Marks, D., Winstral, A., Pomeroy, J.W., and Link, T., 2004. Solar radiation transmission through conifer canopies. Agricultural and Forest Meteorology, 126: 257-270.

Hawkins, D., 1999. Firm: formal inference-based recursive modeling. Department of Applied Statistics, University of Minnesota.

Helbig, N. and van Herwijnen, A., 2012. Modeling the spatial distribution of surface hoar in complex topography. Cold Regions Science and Technology, 82: 68-74.

Hendrikx, J., Leonard, T., Henninger, I. McCabe, D., Hoyer, I. 2012. Examining the drivers that control the spatial variability of surface hoar and near-surface facets. Proceedings of the 2012 International Snow Science Workshop, Anchorage, AK, USA, pp. 1005-1010.

Hendrikx, J., Owens, I., Carran, W. and Carran, A., 2005. Avalanche activity in an extreme maritime climate: The application of classification trees for forecasting. Cold Regions Science and Technology, 43(1-2): 104-116.

Hendrikx, J., Yokley, L., Leonoard, T., 2014. Understanding the spatial variability of surface hoar at the mountain range scale. Proceedings of the 2014 International Snow Science Workshop, Banff, AB, CA, pp. 538-540.

Herbert, T.J., 1987. Area Projections of Fisheye Photographic Lenses. Agricultural and Forest Meteorology, 39(2-3): 215-223.

Holler, P., 1998. Tentative investigations on surface hoar in mountain forests. Annals of Glaciology, Vol 26, 1998, 26: 31-34.

Holler, P., 2001. The influence of the forest on night-time snow surface temperature. Annals of Glaciology, Vol 32, 2001, 32: 217-222.

Horton, S., Bellaire, S. and Jamieson, B., 2014. Modelling the formation of surface hoar layers and tracking post-burial changes for avalanche forecasting. Cold Regions Science and Technology, 97: 81-89.

Jamieson, J.B. and Johnston, C.D., 1992. Snowpack Characteristics Associated with Avalanche Accidents. Canadian Geotechnical Journal, 29(5): 862-866.

Jamieson, B. and Johnston, C.D., 1999. Snowpack factors associated with strength changes of buried surface hoar layers. Cold Regions Science and Technology, 30(1–3): 19-34.

Jamieson, J.B. and Schweizer, J., 2000. Texture and strength changes of buried surface-hoar layers with implications for dry snow-slab avalanche release. Journal of Glaciology, 46(152): 151-160.

Journel, A.G. and Huijbregts, C.J., 1978. Mining geostatistics. Academic Press, London; New York, x, pp. 600.

Kronholm, K., 2004. Spatial variability of snow mechanical properties with regard to avalanche formation. Ph.D. Dissertation, University of Zurich, Zurich, CH, pp. 187.

Kronholm, K. and Birkeland, K.W., 2007. Reliability of sampling designs for spatial snow surveys. Computers & Geosciences, 33(9): 1097-1110.

Lang, R., Leo, B., and Brown, R. (1984). Observations on the growth process and strength characteristics of surface hoar. Proceedings of the 1984 International Snow Science Workshop, Aspen, CO, USA, pp. 188-195.

Landry, C., 2002. Spatial variations in snow stability on uniform slopes: Implications for extrapolation to surrounding terrain, M.S. thesis, Montana State University, Bozeman, MT, USA, pp. 194.

Lemmon, P.E., 1956. A new instrument for measuring forest overstory density. Journal of Forestry, 55: 667-669.

Logan, S., 2005. Temporal changes in the spatial patterns of weak layer shear strength and stability on uniform slopes. M.S. thesis, Montana State University, Bozeman, MT, USA, pp. 157.

Lutz, E., 2009. Spatial and temporal analysis of snowpack strength and stability and environmental determinants on an inclined, forest opening. Ph.D. Dissertation, Montana State University, Bozeman, MT, USA, pp. 364.

McClung, D. and Schaerer, P.A., 2006. The avalanche handbook. Mountaineers Books, Seattle, WA, USA, pp. 342.

Mock, C.J., and Birkeland, K.W., 2000. Snow avalanche climatology of the western United States mountain ranges. Bulletin of the American Meteorological Society. 81(10), 2367-2392.

Moran, P.A.P., 1950. Notes on Continuous Stochastic Phenomena. Biometrika, 37:17-23.

Nakaya, U., 1935. On the correspondence of snow and rime crystals. Journal of the Faculty of Science, 1(7): 201-206.

Nobis, M. (2005): SideLook 1.1 - Imaging software for the analysis of vegetation structure with true-colour photographs. URL: http://www.appleco.ch.

Nobis, M. and Hunziker, U., 2005. Automatic thresholding for hemispherical canopy-photographs based on edge detection. Agricultural and Forest Meteorology, 128(3-4): 243-250.

Oke, T.R., 1987. Boundary layer climates. Methuen, London ; New York, xxiv, pp. 435.

Pebesma, E.J., 2004. Multivariable geostatistics in S: the gstat package. Computers & Geosciences, 30(7): 683-691.

Perla, R.I. and Martinelli, M., 1976. Avalanche handbook. Agriculture handbook 489. U.S. Dept. of Agriculture, Forest Service : for sale by the Supt. of Docs., U.S. Govt. Print. Off., Washington, v, pp. 238.

Plant, R.E., 2012. Spatial data analysis in ecology and agriculture using R. CRC Press, Boca Raton, xv, pp. 631.

Pomeroy, J.W., Marks, D., Link, T., Ellis, C., Hardy, J., Rowlands, A. and Granger, R., 2009. The impact of coniferous forest temperature on incoming longwave radiation to melting snow. Hydrological Processes, 23(17): 2513-2525.

R Core Team, 2013. R. a language and environment for statistical comping. R Foundation for Statistical Computing, Vienna, Austria. URL: http://www.R-project.org/.

Ramsey, F.L. and Schafer, D.W., 2013. The statistical sleuth : a course in methods of data analysis. Brooks/Cole, Cengage Learning, Australia; Boston, xxiv, pp. 760.

Rosenthal, W., Elder, K., Davis, R.E., 2002. Operational decision tree avalanche forecasting. Proceedings of the 2002 International Snow Science Workshop, Penticton, BC, Canada, pp. 13-18.

Salkind, N.J., 2010. Encyclopedia of research design. SAGE Publications, Thousand Oaks, California.

Schabenberger, O. and Gotway, C.A., 2005. Statistical methods for spatial data analysis. Texts in statistical science. Chapman & Hall/CRC, Boca Raton, xvii, pp. 488.

Schweizer, J. and Jamieson, J.B., 2001. Snow cover properties for skier triggering of avalanches. Cold Regions Science and Technology, 33(2-3): 207-221.

Schweizer, J., Jamieson, J.B. and Schneebeli, M., 2003. Snow avalanche formation. Reviews of Geophysics, 41(4).

Schweizer, J. and Kronholm, K., 2007. Snow cover spatial variability at multiple scales: Characteristics of a layer of buried surface hoar. Cold Regions Science and Technology, 47(3): 207-223.

Schweizer, J., Kronholm, K., Jamieson, J.B. and Birkeland, K.W., 2008. Review of spatial variability of snowpack properties and its importance for avalanche formation. Cold Regions Science and Technology, 51(2-3): 253-272.

Seligman, G., 1936. Snow structure and ski fields; being an account of snow and ice forms met with in nature, and a study on avalanches and snowcraft. Macmillan and Co., limited, London, xii, pp. 555.

Shea, C., 2011. Four applied methods for spatial visualization in snow avalanche forecasting. Ph.D. Dissertation, University of Calgary, Calgary, AB, Canada, pp. 141.

Shea, C., and Jamieson, B., 2010a. Star: an efficient snow point-sampling method. Annals of Glaciology, 51(54): 64-72.

Shea, C. and Jamieson, B., 2010b. Spatial distribution of surface hoar crystals in sparse forests. Natural Hazards and Earth System Sciences, 10(6): 1317-1330.

Shea, C. and Jamieson, B., 2011. Sun effect on surface hoar illustrated by three case studies. Cold Regions Science and Technology, 68(3): 99-105.

Shmueli, G., 2010. To Explain or to Predict? Statistical Science, 25(3): 289-310.

Skoien, J.O. and Bloschl, G., 2006. Sampling scale effects in random fields and implications for environmental monitoring. Environmental Monitoring and Assessment, 114(1-3): 521-552.

Slaughter, A., 2010. Numerical analysis of conditions necessary for near-surface snow metamorphism. Ph.D. Dissertation, Montana State University, Bozeman, MT, USA, pp. 562.

Stanton, B., Miller, D., and Adams, E., 2012. Analysis of surface hoar growth under simulated meteorological conditions. Proceedings of the 2012 International Snow Science Workshop, Anchorage, AK, USA, pp. 179-185.

Stossel, F., Guala, M., Fierz, C., Manes, C. and Lehning, M., 2010. Micrometeorological and morphological observations of surface hoar dynamics on a mountain snow cover. Water Resources Research, 46.

Suunto. 2015. PM-5/360 PC Clinometer. User manual.

Therneau, T.M., Atkinson, E.J., and Ripley, B., 2015. Rpart: recursive partitioning and regression trees. URL: http://CRAN.R-project.org/package=rpart.

Zeidler, A. and Jamieson, B., 2006. Refinements of empirical models to forecast the shear strength of persistent weak snow layers - PART B: Layers of surface hoar crystals. Cold Regions Science and Technology, 44(3): 184-193.

Wang, J., Zamar, R., Marazzi, A., Yohai, V., Salibian-Barrera, M., Maronna, R., Zivot, E., Rocke, D., Martin, D., Maechler, M., and Konis, K., 2014. Robust: robust library. URL: http://CRAN.R-project.org/package=robust.

Webster, R. and Oliver, M.A., 2001. Geostatistics for environmental scientists. Statistics in practice. John Wiley & Sons, Chichester, England ; New York, xi, pp. 271.

Yokley, L., Hendrikx, J., Birkeland, K., Williams, K., Leonoard, T., 2014. Role of synoptic atmospheric conditions in the formation and distribution of surface hoar. Proceedings of the 2014 International Snow Science Workshop, Banff, AB, CA, pp. 622-627.

Zar, J.H., 1972. Significance Testing of Spearman Rank Correlation Coefficient. Journal of the American Statistical Association, 67(339): 578-580.

APPENDICES

APPENDIX A

SAMPLING LAYOUTS

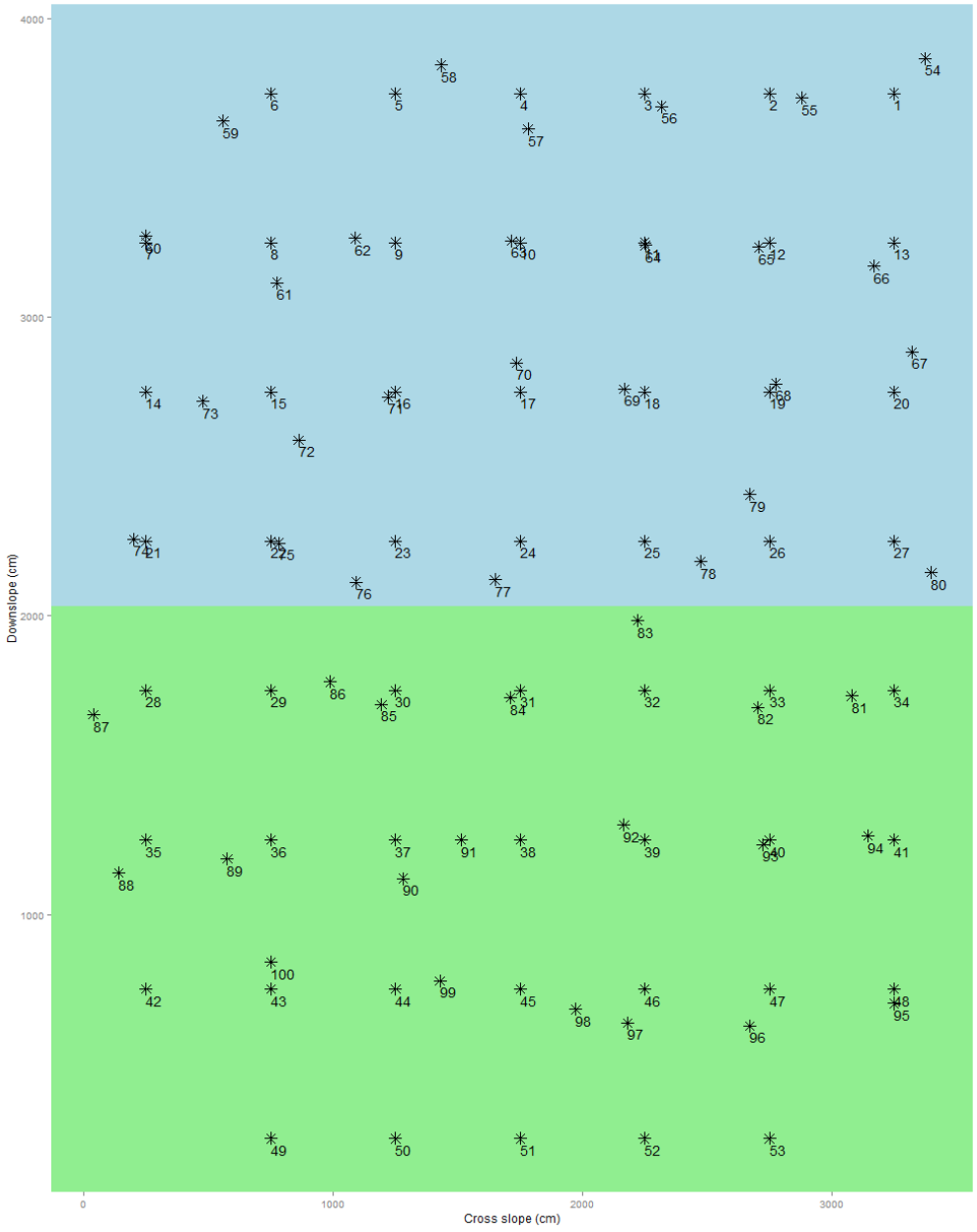


Figure A 1. Sampling layout for the Jan2014 event at the South Site. Observations are numbered in the order they were taken. Blue represents the north plot and green represents the south plot. Points numbered 1 through 53 are on a gridded layout and points 53 through 100 are based on random assignments.

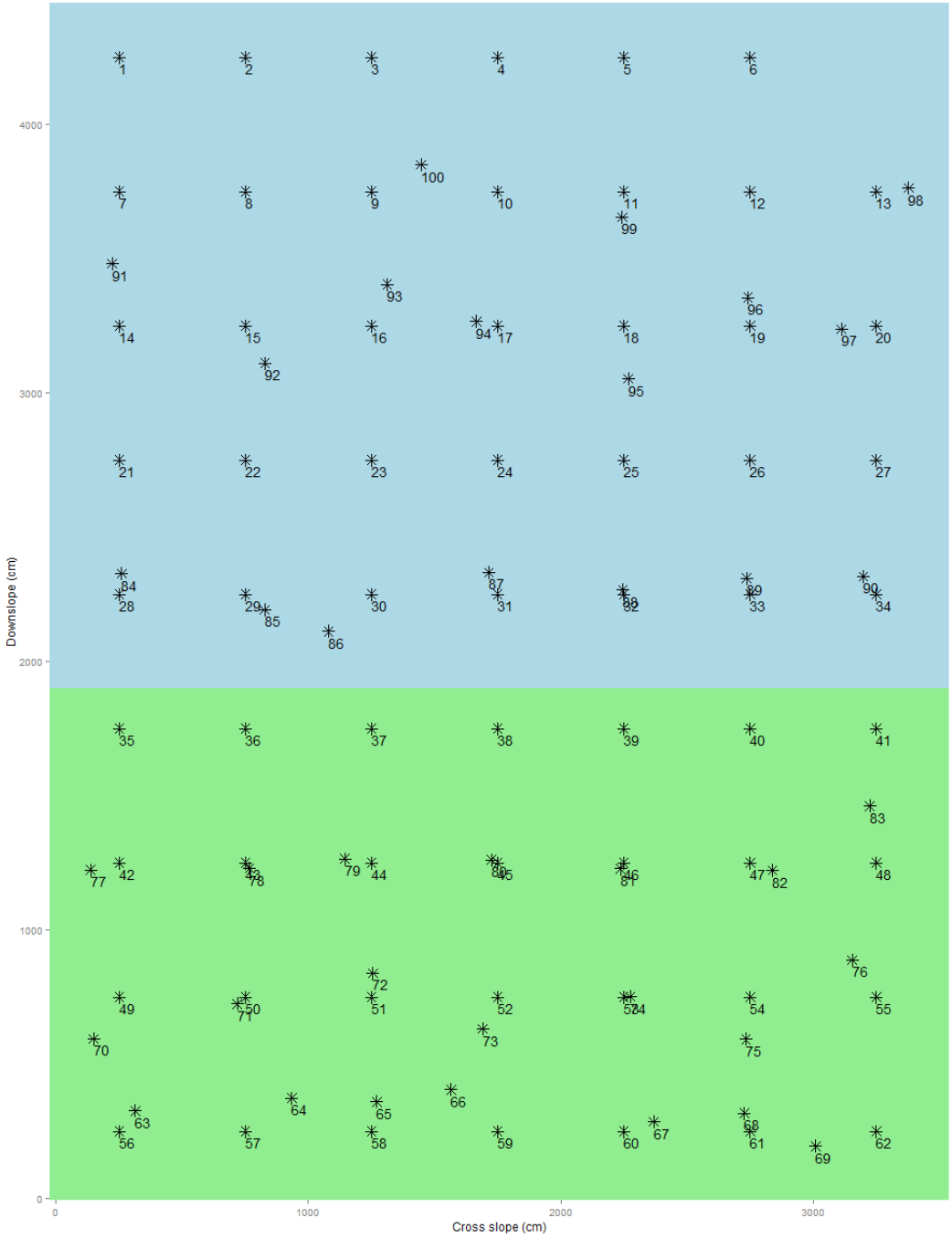


Figure A 2. Sampling layout for the April2014 event at the South Site. Observations are numbered in the order they were taken. Blue represents the north plot and green represents the south plot. Points numbered 1 through 62 are on a gridded layout and points 63 through 100 are based on random assignments.

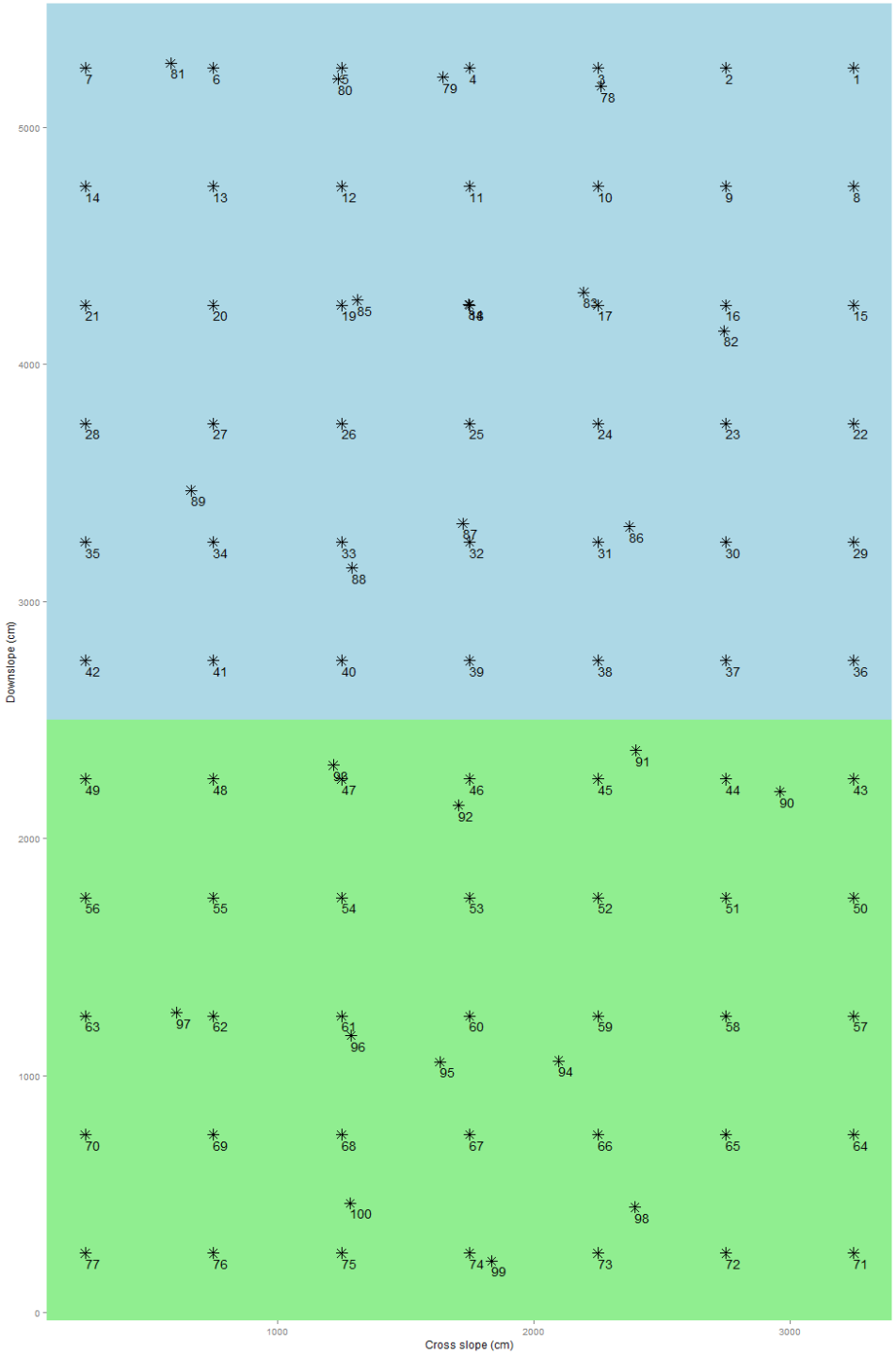


Figure A 3. Sampling layout for the Jan2015 event at the North Site. Observations are numbered in the order they were taken. Blue represents the north plot and green represents the south plot. Points numbered 1 through 77 are on a gridded layout and points 78 through 100 are based on random assignments.

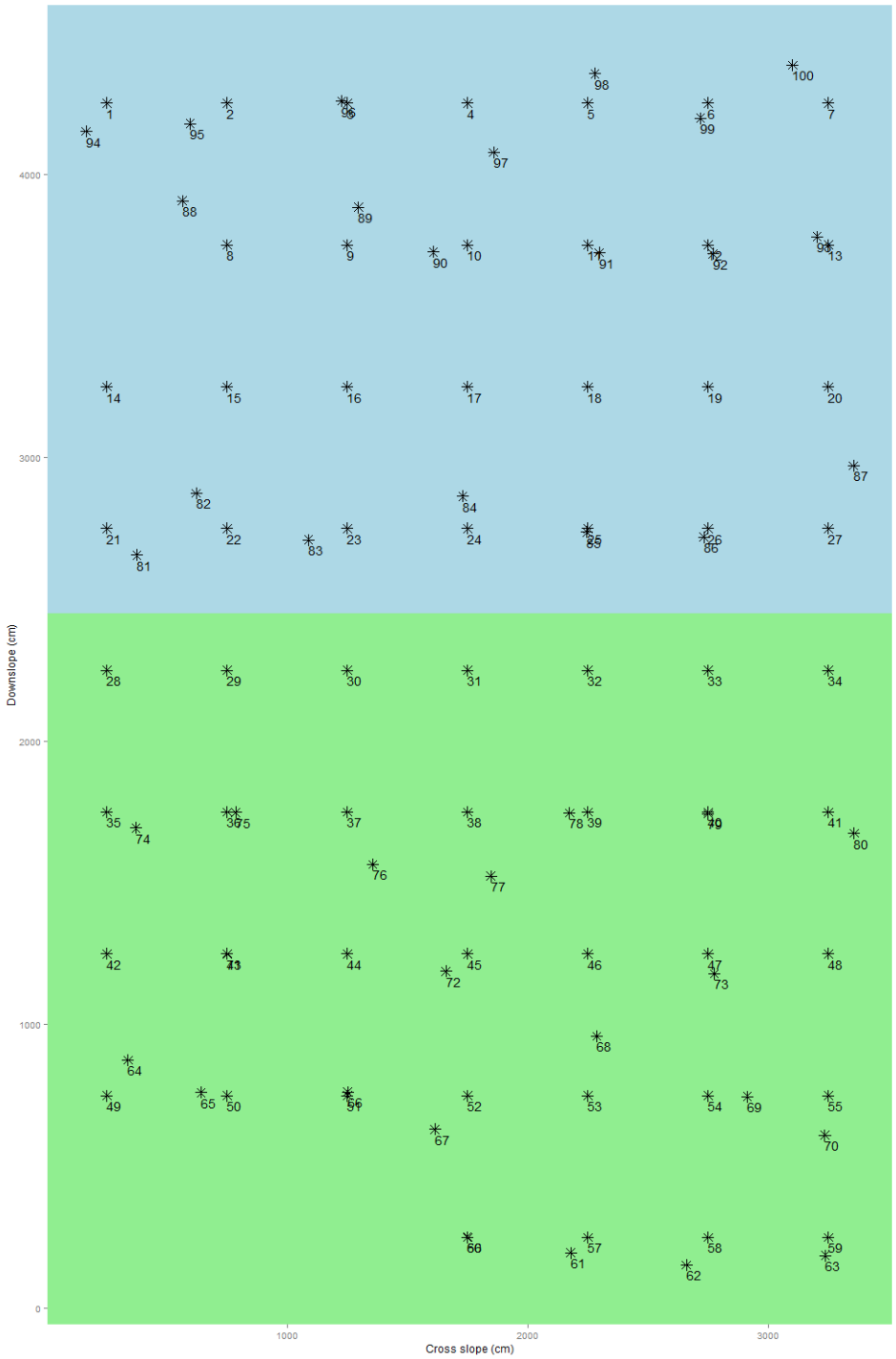


Figure A 4. Sampling layout for the Jan2015 event at the South Site. Observations are numbered in the order they were taken. Blue represents the north plot and green represents the south plot. Points numbered 1 through 59 are on a gridded layout and points 60 through 100 are based on random assignments.

APPENDIX B

SAMPLE SEMI-VARIOGRAMS

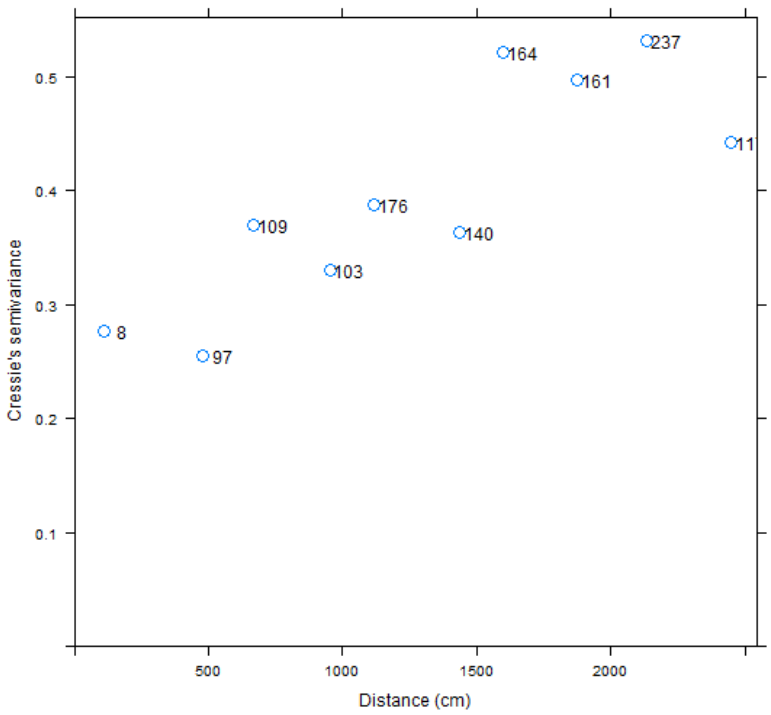


Figure B 1. Sample semi-variogram for the Size$_{Mean}$ for the Jan2014 event at the North Site.

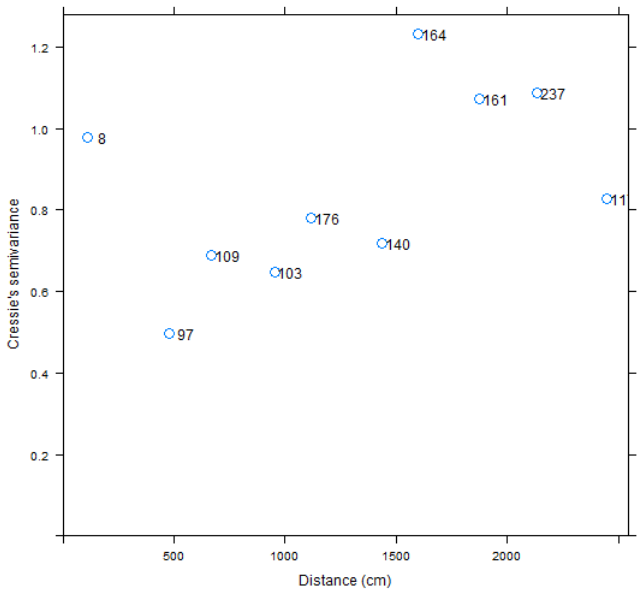


Figure B 2. Sample semi-variogram for the Size$_{90th}$ for the Jan2014 event at the North Site.

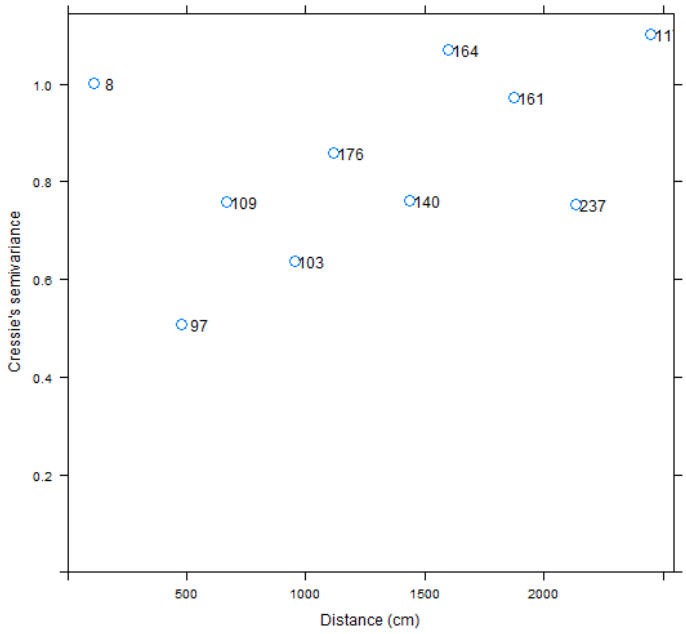


Figure B 3. Sample semi-variogram for the Size$_{Max}$ for the Jan2014 event at the North Site.

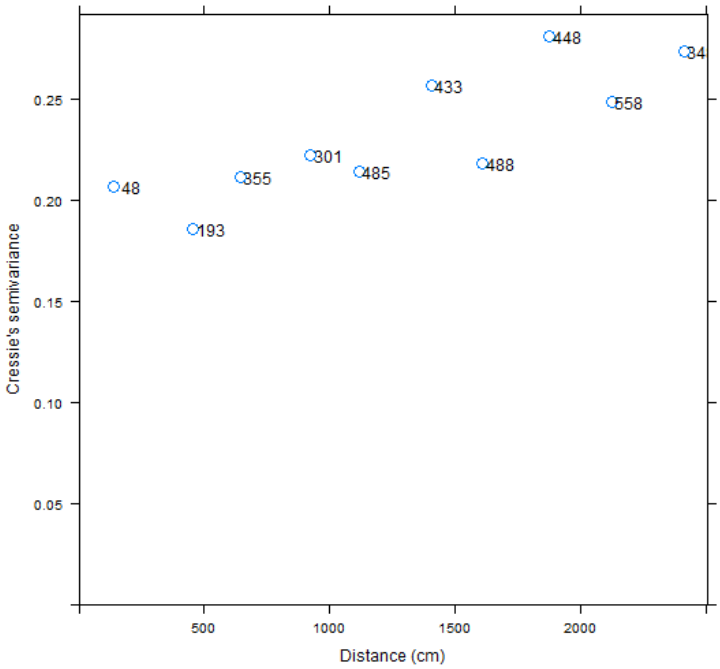


Figure B 4. Sample semi-variogram for the Size$_{90th}$ for the Jan2014 event at the South Site.

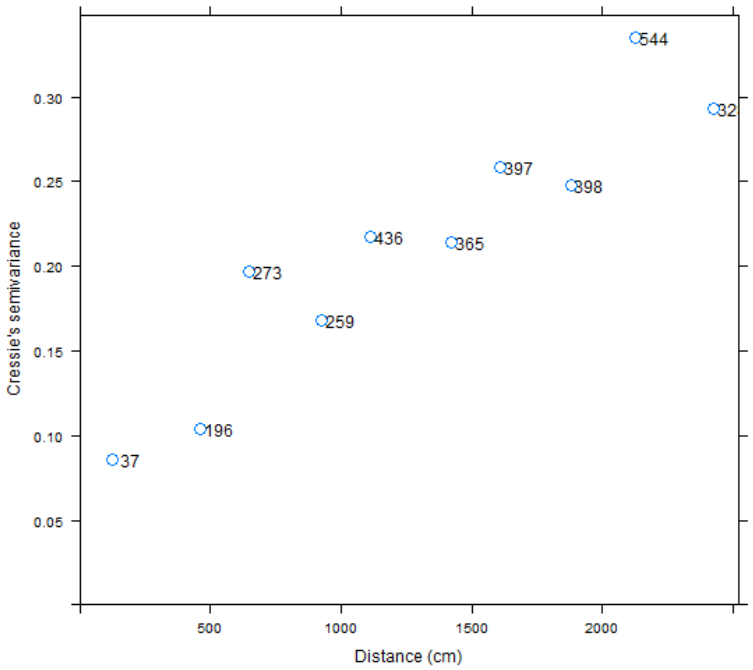


Figure B 5. Sample semi-variogram for the $Size_{Actual}$ for the April2014 event at the South Site.

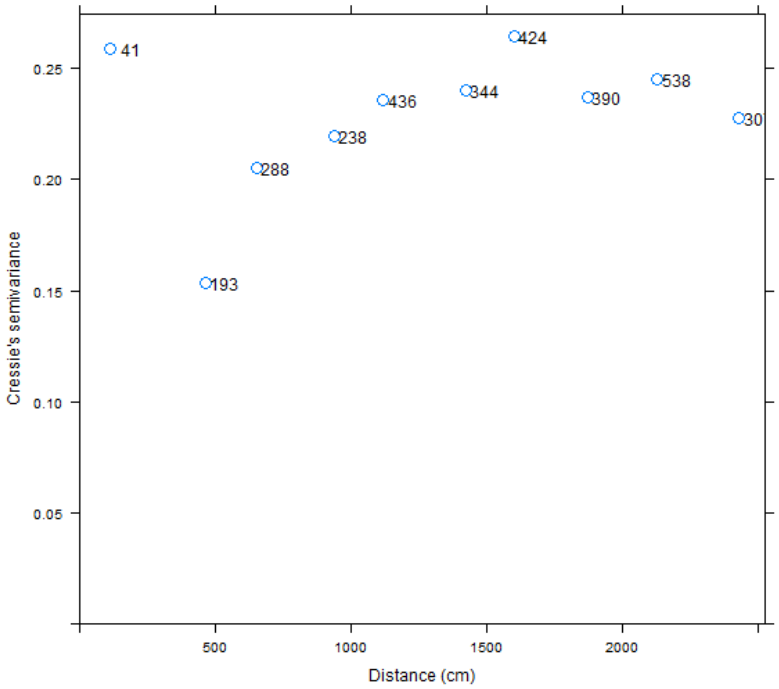


Figure B 6. Sample semi-variogram for the $Size_{Mean}$ for the Jan2015 event at the South Site.

APPENDIX C

MORAN'S I AND LINEAR REGRESSIONS

Table C 1. Moran's I test results for the analysis using a single explanatory variable for the Jan2014 event at the North Site. Bold represents a significant (p-value ≤ 0.05) result.

Jan2014-North			
Variables	Extent	Moran's I	
		Moran's I	p-value
$Size_{Mean} \sim \psi_{Sky}$	Site	**0.35**	**<0.01**
	North Plot	**0.44**	**<0.01**
	South Plot	**0.32**	**<0.01**
$Size_{90th} \sim \psi_{Sky}$	Site	**0.29**	**<0.01**
	North Plot	**0.26**	**0.01**
	South Plot	**0.40**	**<0.01**
$Size_{Max} \sim \psi_{Sky}$	Site	**0.23**	**<0.01**
	North Plot	**0.24**	**0.02**
	South Plot	**0.29**	**<0.01**
$Size_{Mean} \sim \Sigma_{Sunfleck}$	Site	**0.35**	**<0.01**
	North Plot	**0.39**	**<0.01**
	South Plot	**0.37**	**<0.01**
$Size_{90th} \sim \Sigma_{Sunfleck}$	Site	**0.29**	**<0.01**
	North Plot	**0.19**	**0.05**
	South Plot	**0.43**	**<0.01**
$Size_{Max} \sim \Sigma_{Sunfleck}$	Site	**0.22**	**<0.01**
	North Plot	**0.19**	**0.04**
	South Plot	**034**	**<0.01**
$Size_{Mean} \sim \Sigma_{Shortwave}$	Site	**0.22**	**<0.01**
	North Plot	**0.43**	**<0.01**
	South Plot	**0.37**	**<0.01**
$Size_{90th} \sim \Sigma_{Shortwave}$	Site	**0.29**	**<0.01**
	North Plot	**0.22**	**0.02**
	South Plot	**0.42**	**<0.01**
$Size_{Max} \sim \Sigma_{Shortwave}$	Site	**0.22**	**<0.01**
	North Plot	**0.22**	**0.02**
	South Plot	**0.34**	**<0.01**

Table C 2. Moran's I test results for the analysis using a single explanatory variable for the Jan2014 event at the South Site. Bold represents a significant (p-value ≤ 0.05) result.

Jan2014 - South Site			
Variable	Extent	Moran's I	
		Moran's I	**p-value**
$Size_{Mean} \sim \psi_{Sky}$	Site	**0.58**	**<0.01**
	North Plot	**0.49**	**<0.01**
	South Plot	**0.30**	**<0.01**
$Size_{90th} \sim \psi_{Sky}$	Site	**0.55**	**<0.01**
	North Plot	**0.49**	**<0.01**
	South Plot	**0.25**	**<0.01**
$Size_{Max} \sim \psi_{Sky}$	Site	**0.48**	**<0.01**
	North Plot	**.041**	**<0.01**
	South Plot	**0.19**	**<0.01**
$Size_{Mean} \sim \Sigma_{Sunfleck}$	Site	**0.41**	**<0.01**
	North Plot	**0.49**	**<0.01**
	South Plot	**0.24**	**<0.01**
$Size_{90th} \sim \Sigma_{Sunfleck}$	Site	**0.36**	**<0.01**
	North Plot	**0.49**	**<0.01**
	South Plot	**0.19**	**<0.01**
$Size_{Max} \sim \Sigma_{Sunfleck}$	Site	**0.33**	**<0.01**
	North Plot	**0.45**	**<0.01**
	South Plot	**0.16**	**0.01**
$Size_{Mean} \sim \Sigma_{Shortwave}$	Site	**0.39**	**<0.01**
	North Plot	**0.49**	**<0.01**
	South Plot	**0.24**	**<0.01**
$Size_{90th} \sim \Sigma_{Shortwave}$	Site	**0.34**	**<0.01**
	North Plot	**0.49**	**<0.01**
	South Plot	**0.19**	**<0.01**
$Size_{Max} \sim \Sigma_{Shortwave}$	Site	**0.31**	**<0.01**
	North Plot	**0.41**	**<0.01**
	South Plot	**0.16**	**0.02**

Table C 3. Moran's I test results for the analysis using a single explanatory variable for the April2014 event at the South Site. Bold represents a significant (p-value ≤ 0.05) result.

April2014 - South Site			
Variable	Extent	Moran's I	
		Moran's I	p-value
$Size_{actual} \sim \psi_{Sky}$	Site	**0.62**	**<0.01**
	North Plot	**0.61**	**<0.01**
	South Plot	**0.36**	**<0.01**
$Size_{actual} \sim \Sigma_{Sunfleck}$	Site	**0.62**	**<0.01**
	North Plot	**0.64**	**<0.01**
	South Plot	**0.50**	**<0.01**
$Size_{actual} \sim \Sigma_{Shortwave}$	Site	**0.61**	**<0.01**
	North Plot	**0.59**	**<0.01**
	South Plot	**0.51**	**<0.01**

Table C 4. Moran's I test results for the analysis using a single explanatory variable for the Jan2015 event at the North Site. Bold represents a significant (p-value ≤ 0.05) result.

Jan2015 – North Site			
Variable	Extent	Moran's I	
		Moran's I	p-value
$Size_{Mean} \sim \psi_{Sky}$	Site	**0.21**	**<0.01**
	North Plot	**0.20**	**0.01**
	South Plot	**0.15**	**0.04**
$Size_{90th} \sim \psi_{Sky}$	Site	**0.18**	**<0.01**
	North Plot	**0.01**	**0.02**
	South Plot	**0.10**	**0.05**
$Size_{Max} \sim \psi_{Sky}$	Site	**0.16**	**<0.01**
	North Plot	**0.10**	**<0.01**
	South Plot	**0.09**	**0.05**
$Size_{Mean} \sim \Sigma_{Sunfleck}$	Site	**0.23**	**<0.01**
	North Plot	**0.01**	**0.01**
	South Plot	**0.34**	**<0.01**
$Size_{90th} \sim \Sigma_{Sunfleck}$	Site	**0.22**	**<0.01**
	North Plot	**0.04**	**0.02**
	South Plot	**0.29**	**<0.01**
$Size_{Max} \sim \Sigma_{Sunfleck}$	Site	**0.20**	**<0.01**
	North Plot	**0.06**	**<0.01**
	South Plot	**0.27**	**<0.01**
$Size_{Mean} \sim \Sigma_{Shortwave}$	Site	**0.23**	**<0.01**
	North Plot	**0.09**	**<0.01**
	South Plot	**0.27**	**<0.01**
$Size_{90th} \sim \Sigma_{Shortwave}$	Site	**0.21**	**<0.01**
	North Plot	**0.03**	**0.03**
	South Plot	**0.20**	**0.01**
$Size_{Max} \sim \Sigma_{Shortwave}$	Site	**0.20**	**<0.01**
	North Plot	**0.11**	**<0.01**
	South Plot	**0.17**	**0.02**

Table C 5. Moran's I test results for the analysis using a single explanatory variable for the Jan2015 event at the South Site. Bold represents a significant (p-value ≤ 0.05) result.

	Jan2015 – South Site		
Variable	Extent	Moran's I	
		Moran's I	p-value
$Size_{Mean} \sim \psi_{Sky}$	Site	**0.16**	**<0.01**
	North Plot	**0.01**	**0.03**
	South Plot	**0.21**	**<0.01**
$Size_{90th} \sim \psi_{Sky}$	Site	**0.14**	**<0.01**
	North Plot	**0.18**	**0.01**
	South Plot	**0.05**	**0.02**
$Size_{Max} \sim \psi_{Sky}$	Site	**0.16**	**<0.01**
	North Plot	**0.07**	**0.03**
	South Plot	**0.14**	**0.02**
$Size_{Mean} \sim \Sigma_{Sunfleck}$	Site	**0.19**	**<0.01**
	North Plot	**0.07**	**0.02**
	South Plot	**0.30**	**<0.01**
$Size_{90th} \sim \Sigma_{Sunfleck}$	Site	**0.37**	**<0.01**
	North Plot	**0.35**	**<0.01**
	South Plot	**0.14**	**0.02**
$Size_{Max} \sim \Sigma_{Sunfleck}$	Site	**0.19**	**<0.01**
	North Plot	**0.13**	**0.01**
	South Plot	**0.26**	**<0.01**
$Size_{Mean} \sim \Sigma_{Shortwave}$	Site	**0.19**	**<0.01**
	North Plot	**0.15**	**0.01**
	South Plot	**0.31**	**<0.01**
$Size_{90th} \sim \Sigma_{Shortwave}$	Site	**0.37**	**<0.01**
	North Plot	**0.34**	**<0.01**
	South Plot	**0.17**	**0.01**
$Size_{Max} \sim \Sigma_{Shortwave}$	Site	**0.19**	**<0.01**
	North Plot	**0.09**	**0.04**
	South Plot	**0.26**	**<0.01**

Table C 6. Moran's I test results for the analysis using multiple explanatory variables for the Jan2014 event at the North Site. Bold represents a significant (p-value ≤ 0.05) result.

Jan2014 – North Site			
Variables	Extent	Moran's I	
		Moran's I	p-value
$Size_{Mean} \sim \psi_{Sky} + \Sigma_{Sunfleck}$	Site	**0.06**	**<0.01**
	North Plot	**0.16**	**<0.01**
	South Plot	**0.08**	**<0.01**
$Size_{Mean} \sim \psi_{Sky} + \Sigma_{Shortwave}$	Site	**0.08**	**<0.01**
	North Plot	**0.19**	**<0.01**
	South Plot	**0.12**	**<0.01**
$Size_{90th} \sim \psi_{Sky} + \Sigma_{Sunfleck}$	Site	**0.05**	**<0.01**
	North Plot	**0.07**	**<0.01**
	South Plot	**0.05**	**<0.01**
$Size_{90th} \sim \psi_{Sky} + \Sigma_{Shortwave}$	Site	**0.07**	**<0.01**
	North Plot	**0.12**	**<0.01**
	South Plot	**0.05**	**<0.01**
$Size_{Max} \sim \psi_{Sky} + \Sigma_{Sunfleck}$	Site	**0.06**	**<0.01**
	North Plot	**0.07**	**<0.01**
	South Plot	**0.04**	**<0.01**
$Size_{Max} \sim \psi_{Sky} + \Sigma_{Shortwave}$	Site	**0.08**	**<0.01**
	North Plot	**0.13**	**<0.01**
	South Plot	**0.10**	**<0.01**

Table C 7. Moran's I test results for the analysis using multiple explanatory variables for the Jan2014 event at the South Site. Bold represents a significant (p-value ≤ 0.05) result.

Jan2014 – South Site			
Variable	Extent	Moran's I	
		Moran's I	p-value
$Size_{Mean} \sim \psi_{Sky} + \Sigma_{Sunfleck}$	Site	**0.10**	**<0.01**
	North Plot	**0.06**	**<0.01**
	South Plot	**0.02**	**<0.01**
$Size_{Mean} \sim \psi_{Sky} + \Sigma_{Shortwave}$	Site	**0.08**	**<0.01**
	North Plot	**0.06**	**<0.01**
	South Plot	**0.01**	**<0.01**
$Size_{90th} \sim \psi_{Sky} + \Sigma_{Sunfleck}$	Site	**0.09**	**<0.01**
	North Plot	**0.05**	**<0.01**
	South Plot	**0.01**	**0.05**
$Size_{90th} \sim \psi_{Sky} + \Sigma_{Shortwave}$	Site	**0.07**	**<0.01**
	North Plot	**0.05**	**<0.01**
	South Plot	**0.01**	**<0.01**
$Size_{Max} \sim \psi_{Sky} + \Sigma_{Sunfleck}$	Site	**0.09**	**<0.01**
	North Plot	**0.06**	**<0.01**
	South Plot	**0.01**	**0.05**
$Size_{Max} \sim \psi_{Sky} + \Sigma_{Shortwave}$	Site	**0.07**	**<0.01**
	North Plot	**0.05**	**<0.01**
	South Plot	**0.00**	**0.05**

Table C 8. Moran's I test results for the analysis using multiple explanatory variables for the April2014 event at the South Site. Bold represents a significant (p-value ≤ 0.05) result.

April2014 - South Site			
Variable	Extent	Moran's I	
		Moran's I	p-value
$Size_{actual} \sim \psi_{Sky} + \Sigma_{Sunfleck}$	Site	**0.24**	**<0.01**
	North Plot	**0.26**	**<0.01**
	South Plot	**0.00**	**0.01**
$Size_{actual} \sim \psi_{Sky} + \Sigma_{Shortwave}$	Site	**0.27**	**<0.01**
	North Plot	**0.26**	**<0.01**
	South Plot	**0.01**	**<0.01**

Table C 9. Moran's I test results for the analysis using multiple explanatory variables for the Jan2015 event at the North Site. Bold represents a significant (p-value ≤ 0.05) result.

Jan2015 – North Site			
Variable	Extent	Moran's I	
		Moran's I	p-value
$Size_{Mean} \sim \psi_{Sky} + \Sigma_{Sunfleck}$	Site	**0.04**	**<0.01**
	North Plot	**0.01**	**0.01**
	South Plot	**0.01**	**0.02**
$Size_{Mean} \sim \psi_{Sky} + \Sigma_{Shortwave}$	Site	**0.05**	**<0.01**
	North Plot	**0.02**	**<0.01**
	South Plot	**0.00**	**0.05**
$Size_{90th} \sim \psi_{Sky} + \Sigma_{Sunfleck}$	Site	**0.05**	**<0.01**
	North Plot	**0.01**	**0.01**
	South Plot	**0.00**	**0.01**
$Size_{90th} \sim \psi_{Sky} + \Sigma_{Shortwave}$	Site	**0.06**	**<0.01**
	North Plot	**0.01**	**0.01**
	South Plot	**0.02**	**<0.01**
$Size_{Max} \sim \psi_{Sky} + \Sigma_{Sunfleck}$	Site	**0.06**	**<0.01**
	North Plot	**0.01**	**<0.01**
	South Plot	**0.02**	**0.01**
$Size_{Max} \sim \psi_{Sky} + \Sigma_{Shortwave}$	Site	**0.07**	**<0.01**
	North Plot	**0.01**	**<0.01**
	South Plot	**0.03**	**<0.01**

Table C 10. Moran's I test results for the analysis using multiple explanatory variables for the Jan2015 event at the South Site. Bold represents a significant (p-value ≤ 0.05) result.

Jan2015 – South Site			
Variable	Extent	Moran's I	
		Moran's I	p-value
$Size_{Mean} \sim \psi_{Sky} + \Sigma_{Sunfleck}$	Site	**0.02**	**<0.01**
	North Plot	**0.01**	**0.02**
	South Plot	**0.02**	**<0.01**
$Size_{Mean} \sim \psi_{Sky} + \Sigma_{Shortwave}$	Site	**0.02**	**<0.01**
	North Plot	**0.01**	**<0.01**
	South Plot	**0.01**	**0.02**
$Size_{90th} \sim \psi_{Sky} + \Sigma_{Sunfleck}$	Site	**0.01**	**0.05**
	North Plot	**0.00**	**<0.01**
	South Plot	**0.03**	**<0.01**
$Size_{90th} \sim \psi_{Sky} + \Sigma_{Shortwave}$	Site	**0.00**	**0.03**
	North Plot	**0.00**	**<0.01**
	South Plot	**0.02**	**<0.01**
$Size_{Max} \sim \psi_{Sky} + \Sigma_{Sunfleck}$	Site	**0.00**	**0.05**
	North Plot	**0.01**	**<0.01**
	South Plot	**0.02**	**<0.01**
$Size_{Max} \sim \psi_{Sky} + \Sigma_{Shortwave}$	Site	**0.00**	**0.03**
	North Plot	**0.01**	**<0.01**
	South Plot	**0.02**	**0.01**

Table C 11. Spatial lag model regressions for the Jan2014 event at the North Site.

Jan2014 – North Site – Spatial Lag				
Variable	Extent	Regression Coefficient		
		$ß_0$	$ß_1$	p-value
$Size_{Mean} \sim \psi_{Sky}$	Site	0.91	0.16	0.45
	North Plot	-3.12	0.07	0.32
	South Plot	-1.04	0.04	0.18
$Size_{90th} \sim \psi_{Sky}$	Site	1.32	0.03	0.37
	North Plot	-11.30	0.20	0.11
	South Plot	-1.74	0.06	0.15
$Size_{Max} \sim \psi_{Sky}$	Site	2.00	0.03	0.43
	North Plot	-7.68	0.16	0.29
	South Plot	-1.92	0.09	0.09
$Size_{Mean} \sim \Sigma_{Sunfleck}$	Site	1.98	0.00	0.95
	North Plot	1.87	0.00	0.95
	South Plot	1.84	0.00	0.65
$Size_{90th} \sim \Sigma_{Sunfleck}$	Site	3.38	0.00	0.81
	North Plot	5.05	0.00	0.51
	South Plot	2.03	0.00	0.58
$Size_{Max} \sim \Sigma_{Sunfleck}$	Site	4.57	0.00	0.47
	North Plot	6.88	-0.01	0.19
	South Plot	3.35	0.00	0.77
$Size_{Mean} \sim \Sigma_{Shortwave}$	Site	1.79	0.03	0.73
	North Plot	0.86	0.17	0.42
	South Plot	1.70	0.09	0.59
$Size_{90th} \sim \Sigma_{Shortwave}$	Site	3.07	0.03	0.81
	North Plot	3.07	0.12	0.76
	South Plot	1.87	0.13	0.53
$Size_{Max} \sim \Sigma_{Shortwave}$	Site	4.19	-0.03	0.85
	North Plot	4.75	-0.14	0.76
	South Plot	3.08	0.12	0.63

Table C 12. Spatial lag model regressions for the Jan2014 event at the South Site.

Jan2014 – South Site - Spatial Lag				
Variable	Extent	Regression Coefficient		
		$ß_0$	$ß_1$	p-value
$Size_{Mean} \sim \psi_{Sky}$	Site	0.08	0.01	0.52
	North Plot	0.02	0.01	0.61
	South Plot	0.37	0.01	0.39
$Size_{90th} \sim \psi_{Sky}$	Site	-0.06	0.01	0.39
	North Plot	-0.33	0.01	0.39
	South Plot	0.51	0.01	0.45
$Size_{Max} \sim \psi_{Sky}$	Site	0.19	0.01	0.52
	North Plot	-0.03	0.01	0.54
	South Plot	0.72	0.02	0.43
$Size_{Mean} \sim \Sigma_{Sunfleck}$	Site	0.74	0.00	0.16
	North Plot	0.24	0.00	0.79
	South Plot	1.16	0.00	0.72
$Size_{90th} \sim \Sigma_{Sunfleck}$	Site	1.01	0.00	0.14
	North Plot	0.00	0.00	0.99
	South Plot	1.60	0.00	0.61
$Size_{Max} \sim \Sigma_{Sunfleck}$	Site	1.23	0.00	0.14
	North Plot	0.76	0.00	0.94
	South Plot	1.79	0.00	0.82
$Size_{Mean} \sim \Sigma_{Shortwave}$	Site	0.89	-0.03	0.06
	North Plot	0.14	0.02	0.77
	South Plot	1.27	-0.02	0.52
$Size_{90th} \sim \Sigma_{Shortwave}$	Site	1.20	-0.04	0.06
	North Plot	0.14	0.03	0.76
	South Plot	1.76	-0.03	0.43
$Size_{Max} \sim \Sigma_{Shortwave}$	Site	1.43	-0.04	0.06
	North Plot	0.31	0.03	0.78
	South Plot	1.91	-0.02	0.64

Table C 13. Spatial lag model regressions for the April2014 event at the South Site.

April2014 – South Site – Spatial Lag				
Variable	Extent	Regression Coefficient		
		$ß_0$	$ß_1$	p-value
$Size_{actual} \sim \psi_{Sky}$	Site	0.03	0.00	0.55
	North Plot	0.94	-0.01	0.41
	South Plot	-1.37	**0.03**	**<0.01**
$Size_{actual} \sim \Sigma_{Sunfleck}$	Site	0.11	0.00	0.58
	North Plot	0.52	0.00	0.76
	South Plot	-0.30	0.00	0.12
$Size_{actual} \sim \Sigma_{Shortwave}$	Site	0.21	0.00	0.79
	North Plot	0.87	-0.22	0.40
	South Plot	-0.25	0.02	0.11

Table C 14. Spatial lag model regressions for the Jan2015 event at the North Site.

Jan2015 – North Site – Spatial Lag				
Variable	Extent	Regression Coefficient		
		$ß_0$	$ß_1$	p-value
$Size_{Mean} \sim \psi_{Sky}$	Site	2.49	0.36	0.11
	North Plot	9.07	-0.03	0.69
	South Plot	**-0.11**	**0.09**	**<0.01**
$Size_{90th} \sim \psi_{Sky}$	Site	3.50	0.05	0.09
	North Plot	7.24	0.04	0.94
	South Plot	2.48	0.14	0.28
$Size_{Max} \sim \psi_{Sky}$	Site	**3.22**	**0.08**	**0.03**
	North Plot	4.47	0.09	0.43
	South Plot	0.73	0.19	0.33
$Size_{Mean} \sim \Sigma_{Sunfleck}$	Site	4.97	0.00	0.19
	North Plot	8.10	0.00	0.58
	South Plot	3.14	0.00	0.80
$Size_{90th} \sim \Sigma_{Sunfleck}$	Site	6.52	0.00	0.46
	North Plot	10.51	0.00	0.28
	South Plot	4.75	0.00	0.98
$Size_{Max} \sim \Sigma_{Sunfleck}$	Site	7.49	0.00	0.87
	North Plot	11.34	0.00	0.87
	South Plot	5.22	0.01	0.67
$Size_{Mean} \sim \Sigma_{Shortwave}$	Site	4.75	-0.10	0.65
	North Plot	8.29	-0.36	0.31
	South Plot	2.74	0.52	0.30
$Size_{90th} \sim \Sigma_{Shortwave}$	Site	6.29	-0.02	0.95
	North Plot	10.32	-0.11	0.83
	South Plot	4.31	0.71	0.34
$Size_{Max} \sim \Sigma_{Shortwave}$	Site	7.08	0.17	0.63
	North Plot	10.99	0.09	0.85
	South Plot	4.41	1.35	0.14

Table C 15. Spatial lag model regressions for the Jan2015 event at the South Site.

Jan2015 - South Site – Spatial Lag				
Variable	Extent	Regression Coefficient		
		$ß_0$	$ß_1$	p-value
$Size_{Mean} \sim \psi_{Sky}$	Site	0.70	0.01	0.12
	North Plot	1.58	0.02	0.51
	South Plot	0.43	0.01	0.11
$Size_{90th} \sim \psi_{Sky}$	Site	-5.08	**0.20**	**<0.01**
	North Plot	-5.57	**0.18**	**0.02**
	South Plot	-7.17	**0.31**	**<0.01**
$Size_{Max} \sim \psi_{Sky}$	Site	-9.23	**0.29**	**<0.01**
	North Plot	-9.49	**0.35**	**<0.01**
	South Plot	-7.57	**0.47**	**<0.01**
$Size_{Mean} \sim \Sigma_{Sunfleck}$	Site	1.05	0.00	0.63
	North Plot	1.15	0.00	0.22
	South Plot	0.78	0.00	0.72
$Size_{90th} \sim \Sigma_{Sunfleck}$	Site	3.01	0.00	0.54
	North Plot	1.16	0.01	0.57
	South Plot	3.63	**0.02**	**0.02**
$Size_{Max} \sim \Sigma_{Sunfleck}$	Site	0.27	0.00	0.23
	North Plot	3.40	0.00	0.87
	South Plot	2.48	**0.02**	**0.01**
$Size_{Mean} \sim \Sigma_{Shortwave}$	Site	1.07	0.00	0.82
	North Plot	1.57	0.02	0.73
	South Plot	0.77	0.01	0.73
$Size_{90th} \sim \Sigma_{Shortwave}$	Site	7.48	0.09	0.68
	North Plot	2.98	0.00	0.99
	South Plot	3.30	0.44	0.07
$Size_{Max} \sim \Sigma_{Shortwave}$	Site	0.46	0.13	0.36
	North Plot	5.33	-0.11	0.80
	South Plot	1.58	**0.70**	**0.02**

Table C 16. Spatial lag model multiple regressions for the Jan2014 event at the North Site.

Jan2014 – North Site – Spatial Lag						
Variable	Extent	Regression Coefficient				
		ß$_0$	ß$_1$	p-value	ß$_2$	p-value
$Size_{Mean} \sim \psi_{Sky} + \Sigma_{Sunfleck}$	Site	-3.00	**0.07**	**0.03**	-0.01	0.06
	North Plot	-10.50	**0.17**	**0.04**	0.00	0.09
	South Plot	2.36	**0.11**	**0.02**	0.00	0.27
$Size_{Mean} \sim \psi_{Sky} + \Sigma_{Shortwave}$	Site	-2.24	0.06	0.10	-0.23	0.23
	North Plot	-6.86	0.11	0.26	-0.14	0.65
	South Plot	1.76	**0.13**	**0.01**	-0.33	0.19
$Size_{90th} \sim \psi_{Sky} + \Sigma_{Sunfleck}$	Site	-4.47	**0.12**	**0.02**	-0.01	0.04
	North Plot	-30.58	**0.52**	**<0.01**	**-0.02**	**<0.01**
	South Plot	0.92	**0.13**	**0.03**	0.00	0.58
$Size_{90th} \sim \psi_{Sky} + \Sigma_{Shortwave}$	Site	-3.24	0.09	0.10	-0.37	0.20
	North Plot	-26.44	**0.44**	**0.01**	-0.94	0.07
	South Plot	0.23	**0.15**	**0.04**	-0.24	0.48
$Size_{Max} \sim \psi_{Sky} + \Sigma_{Sunfleck}$	Site	-7.30	**0.17**	**<0.01**	**-0.01**	**<0.01**
	North Plot	-32.45	**0.57**	**<0.01**	**-0.03**	**<0.01**
	South Plot	-1.81	**0.17**	**<0.01**	0.00	0.16
$Size_{Max} \sim \psi_{Sky} + \Sigma_{Shortwave}$	Site	-5.82	**0.15**	**0.02**	**-0.66**	**0.03**
	North Plot	-26.72	**0.48**	**0.01**	**-1.31**	**0.03**
	South Plot	-2.91	**0.20**	**<0.01**	-0.55	0.11

Table C 17. Spatial lag model multiple regressions for the Jan2014 event at the South Site.

Jan2014 - South Site – Spatial Lag						
Variable	Extent	Regression Coefficient				
		ß$_0$	ß$_1$	p-value	ß$_2$	p-value
$Size_{Mean} \sim \psi_{Sky} + \Sigma_{Sunfleck}$	Site	-0.92	**0.03**	**<0.01**	**-0.01**	**<0.01**
	North Plot	-0.49	0.01	0.30	0.00	0.93
	South Plot	7.88	0.00	0.62	0.00	0.13
$Size_{Mean} \sim \psi_{Sky} + \Sigma_{Shortwave}$	Site	-0.74	**0.05**	**<0.01**	**-0.07**	**<0.01**
	North Plot	-0.28	0.01	0.27	-0.03	0.73
	South Plot	8.23	0.00	0.64	-0.05	0.08
$Size_{90th} \sim \psi_{Sky} + \Sigma_{Sunfleck}$	Site	-1.27	**0.04**	**<0.01**	**-0.02**	**<0.01**
	North Plot	-0.66	0.02	0.18	0.00	0.72
	South Plot	8.49	0.01	0.50	0.00	0.11
$Size_{90th} \sim \psi_{Sky} + \Sigma_{Shortwave}$	Site	-1.01	**0.04**	**<0.01**	**-0.09**	**<0.01**
	North Plot	-0.48	0.02	0.17	-0.05	0.65
	South Plot	9.05	0.01	0.54	-0.08	0.07
$Size_{Max} \sim \psi_{Sky} + \Sigma_{Sunfleck}$	Site	-1.25	**0.03**	**0.01**	**-0.01**	**<0.01**
	North Plot	-0.37	0.02	0.33	0.00	0.78
	South Plot	6.40	0.02	0.44	0.00	0.27
$Size_{Max} \sim \psi_{Sky} + \Sigma_{Shortwave}$	Site	-1.02	**0.03**	**0.01**	**-0.09**	**<0.01**
	North Plot	-0.31	0.02	0.34	-0.03	0.79
	South Plot	6.68	0.01	0.43	-0.06	0.20

Table C 18. Spatial lag model multiple regressions for the April2014 event at the South Site.

April2014-South Site – Spatial Lag						
Variable	Extent	Regression Coefficient				
		ß$_0$	ß$_1$	p-value	ß$_2$	p-value
$Size_{actual} \sim \psi_{Sky} + \Sigma_{Sunfleck}$	Site	0.21	0.00	0.28	0.00	0.30
	North Plot	1.62	**-0.05**	**0.01**	0.00	0.06
	South Plot	-2.02	**0.05**	**<0.01**	0.00	0.07
$Size_{actual} \sim \psi_{Sky} + \Sigma_{Shortwave}$	Site	0.27	-0.01	0.88	0.00	0.67
	North Plot	1.54	-0.02	0.49	0.00	0.82
	South Plot	-2.16	**0.06**	**<0.01**	**-0.04**	**0.02**

Table C 19. Spatial lag model multiple regressions for the Jan2015 event at the North Site.

Jan2015 - North Site – Spatial lag						
Variable	Extent	Regression Coefficient				
		ß$_0$	ß$_1$	p-value	ß$_2$	p-value
$Size_{Mean} \sim \psi_{Sky} + \Sigma_{Sunfleck}$	Site	-6.28	**0.18**	**<0.01**	**-0.01**	**<0.01**
	North Plot	-10.22	0.27	0.40	-0.01	0.11
	South Plot	-1.54	**0.21**	**<0.01**	**-0.01**	**0.02**
$Size_{Mean} \sim \psi_{Sky} + \Sigma_{Shortwave}$	Site	-6.85	**0.21**	**<0.01**	**-1.43**	**<0.01**
	North Plot	-8.71	0.25	0.61	-1.03	0.30
	South Plot	-2.92	**0.23**	**<0.01**	**-1.16**	**0.01**
$Size_{90th} \sim \psi_{Sky} + \Sigma_{Sunfleck}$	Site	-7.78	**0.21**	**<0.01**	**-0.01**	**<0.01**
	North Plot	-12.43	0.31	0.32	-0.01	0.25
	South Plot	-5.80	**0.26**	**<0.01**	-0.01	0.08
$Size_{90th} \sim \psi_{Sky} + \Sigma_{Shortwave}$	Site	-8.32	**0.23**	**<0.01**	**-1.39**	**<0.01**
	North Plot	-10.50	0.28	0.53	-0.71	0.55
	South Plot	-6.84	**0.28**	**<0.01**	-1.12	0.03
$Size_{Max} \sim \psi_{Sky} + \Sigma_{Sunfleck}$	Site	-10.08	**0.25**	**<0.01**	**-0.01**	**<0.01**
	North Plot	-8.80	0.38	0.30	-0.01	0.47
	South Plot	-11.02	**0.30**	**<0.01**	-0.01	0.15
$Size_{Max} \sim \psi_{Sky} + \Sigma_{Shortwave}$	Site	-10.61	**0.27**	**<0.01**	**-1.43**	**0.01**
	North Plot	-7.16	0.35	0.45	-0.62	0.77
	South Plot	-11.55	**0.32**	**<0.01**	-0.87	0.08

Table C 20. Spatial lag model multiple regressions for the Jan2015 event at the South Site.

Jan2015 - South Site – Spatial Lag						
Variable	Extent	Regression Coefficients				
		ß$_0$	ß$_1$	p-value	ß$_2$	p-value
$Size_{Mean} \sim \psi_{Sky} + \Sigma_{Sunfleck}$	Site	0.71	**0.01**	**0.02**	0.00	0.39
	North Plot	2.36	-0.01	0.85	0.00	0.26
	South Plot	2.56	**0.03**	**<0.01**	0.00	0.13
$Size_{Mean} \sim \psi_{Sky} + \Sigma_{Shortwave}$	Site	0.73	**0.01**	**0.01**	-0.01	0.20
	North Plot	2.36	-0.01	0.90	0.00	0.97
	South Plot	2.57	**0.03**	**<0.01**	-0.04	0.13
$Size_{90th} \sim \psi_{Sky} + \Sigma_{Sunfleck}$	Site	-11.87	**0.38**	**<0.01**	**-0.01**	**0.01**
	North Plot	6.02	**0.35**	**<0.01**	-0.03	0.12
	South Plot	-4.99	**0.46**	**<0.01**	0.00	0.70
$Size_{90th} \sim \psi_{Sky} + \Sigma_{Shortwave}$	Site	-11.49	**0.38**	**<0.01**	**-0.49**	**<0.01**
	North Plot	3.49	**0.35**	**<0.01**	**-0.97**	**0.01**
	South Plot	-5.17	**0.43**	**<0.01**	-0.12	0.89
$Size_{Max} \sim \psi_{Sky} + \Sigma_{Sunfleck}$	Site	-14.40	**0.46**	**<0.01**	-0.01	0.02
	North Plot	6.52	**0.44**	**<0.01**	-0.04	0.15
	South Plot	-10.66	**0.54**	**<0.01**	0.00	0.86
$Size_{Max} \sim \psi_{Sky} + \Sigma_{Shortwave}$	Site	-14.02	**0.46**	**<0.01**	**-0.50**	**0.01**
	North Plot	4.07	**0.45**	**<0.01**	**-1.09**	**0.02**
	South Plot	-10.10	**0.53**	**<0.01**	-0.15	0.86

Table C 21. Spatial error model regressions for the Jan2014 event at the North Site.

Jan2014 - North Site – Spatial Error				
Variable	Extent	Regression Coefficient		
		$ß_0$	$ß_1$	p-value
$Size_{Mean} \sim \psi_{Sky}$	Site	2.20	0.03	0.40
	North Plot	-5.01	0.12	0.17
	South Plot	-0.25	0.07	0.18
$Size_{90th} \sim \psi_{Sky}$	Site	2.23	0.05	0.31
	North Plot	**-16.55**	**0.29**	**0.05**
	South Plot	-0.88	0.10	0.14
$Size_{Max} \sim \psi_{Sky}$	Site	2.91	0.04	0.36
	North Plot	-12.13	0.24	0.17
	South Plot	-1.40	0.11	0.08
$Size_{Mean} \sim \Sigma_{Sunfleck}$	Site	4.25	0.00	0.93
	North Plot	3.73	0.00	0.72
	South Plot	3.85	0.00	0.63
$Size_{90th} \sim \Sigma_{Sunfleck}$	Site	5.92	0.00	0.63
	North Plot	6.79	-0.01	0.52
	South Plot	5.25	0.00	0.72
$Size_{Max} \sim \Sigma_{Sunfleck}$	Site	6.94	0.00	0.35
	North Plot	9.42	-0.01	0.16
	South Plot	6.05	0.00	0.85
$Size_{Mean} \sim \Sigma_{Shortwave}$	Site	3.85	0.07	0.68
	North Plot	2.22	0.36	0.22
	South Plot	3.54	0.16	0.55
$Size_{90th} \sim \Sigma_{Shortwave}$	Site	5.45	0.01	0.95
	North Plot	4.59	0.16	0.74
	South Plot	4.99	0.15	0.68
$Size_{Max} \sim \Sigma_{Shortwave}$	Site	6.49	-0.07	0.76
	North Plot	7.23	-0.21	0.71
	South Plot	5.57	0.16	0.66

Table C 22. Spatial error model regressions for the Jan2014 event at the South Site.

Jan2014 - South Site – Spatial Error				
Variable	Extent	Regression Coefficient		
		$ß_0$	$ß_1$	p-value
$Size_{Mean} \sim \psi_{Sky}$	Site	1.21	0.01	0.60
	North Plot	2.23	-0.01	0.59
	South Plot	0.66	0.02	0.20
$Size_{90th} \sim \psi_{Sky}$	Site	0.49	0.03	0.24
	North Plot	1.38	0.01	0.82
	South Plot	0.54	0.03	0.22
$Size_{Max} \sim \psi_{Sky}$	Site	1.03	0.02	0.41
	North Plot	1.35	0.01	0.76
	South Plot	0.99	0.03	0.30
$Size_{Mean} \sim \Sigma_{Sunfleck}$	Site	1.87	0.00	0.70
	North Plot	1.43	0.00	0.94
	South Plot	2.10	0.00	0.92
$Size_{90th} \sim \Sigma_{Sunfleck}$	Site	2.22	0.00	0.67
	North Plot	2.16	0.00	0.72
	South Plot	2.52	0.00	0.82
$Size_{Max} \sim \Sigma_{Sunfleck}$	Site	2.60	0.00	0.38
	North Plot	2.55	0.00	0.64
	South Plot	2.62	0.00	0.92
$Size_{Mean} \sim \Sigma_{Shortwave}$	Site	2.20	-0.04	0.23
	North Plot	1.48	0.00	0.99
	South Plot	2.23	-0.02	0.64
$Size_{90th} \sim \Sigma_{Shortwave}$	Site	2.57	-0.05	0.28
	North Plot	1.47	0.02	0.86
	South Plot	2.71	-0.03	0.55
$Size_{Max} \sim \Sigma_{Shortwave}$	Site	2.92	-0.06	0.15
	North Plot	1.47	0.03	0.82
	South Plot	2.77	-0.02	0.70

Table C 23. Spatial error model regressions for the April2014 event at the South Site.

April2014 - South Site – Spatial Error				
Variable	Extent	Regression Coefficient		
		ß$_0$	ß$_1$	p-value
$Size_{actual} \sim \psi_{Sky}$	Site	-0.12	0.02	0.18
	North Plot	1.33	0.00	0.99
	South Plot	**-2.49**	**0.06**	**<0.01**
$Size_{actual} \sim \Sigma_{Sunfleck}$	Site	0.62	0.00	0.41
	North Plot	1.38	0.00	0.97
	South Plot	-0.06	0.00	0.09
$Size_{actual} \sim \Sigma_{Shortwave}$	Site	0.84	0.02	0.55
	North Plot	1.81	-0.02	0.70
	South Plot	0.18	0.04	0.13

Table C 24. Spatial error model regressions for the Jan2015 event at the North Site.

Jan2015 - North Site – Spatial Error				
Variable	Extent	Regression Coefficient		
		ß$_0$	ß$_1$	p-value
$Size_{Mean} \sim \psi_{Sky}$	Site	4.52	0.05	0.09
	North Plot	8.94	-0.02	0.96
	South Plot	1.65	**0.11**	**<0.01**
$Size_{90th} \sim \psi_{Sky}$	Site	6.26	0.06	0.10
	North Plot	7.45	0.04	0.91
	South Plot	1.58	0.15	0.47
$Size_{Max} \sim \psi_{Sky}$	Site	**5.34**	**0.10**	**0.03**
	North Plot	4.11	0.10	0.88
	South Plot	0.26	0.19	0.24
$Size_{Mean} \sim \Sigma_{Sunfleck}$	Site	8.12	-0.01	0.13
	North Plot	8.13	0.00	0.95
	South Plot	8.19	-0.01	0.25
$Size_{90th} \sim \Sigma_{Sunfleck}$	Site	10.75	0.00	0.32
	North Plot	10.59	0.00	0.71
	South Plot	11.04	-0.02	0.31
$Size_{Max} \sim \Sigma_{Sunfleck}$	Site	11.65	0.00	0.85
	North Plot	11.31	0.00	0.99
	South Plot	11.99	0.00	0.70
$Size_{Mean} \sim \Sigma_{Shortwave}$	Site	7.97	-0.18	0.58
	North Plot	8.28	0.36	0.99
	South Plot	7.64	0.15	0.82
$Size_{90th} \sim \Sigma_{Shortwave}$	Site	6.28	-0.02	0.95
	North Plot	10.39	-0.14	0.81
	South Plot	10.77	-0.13	0.89
$Size_{Max} \sim \Sigma_{Shortwave}$	Site	11.02	0.24	0.64
	North Plot	10.87	0.13	0.94
	South Plot	10.38	1.00	0.39

Table C 25. Spatial error model regressions for the Jan2015 event at the South Site.

Jan2015 – South Site – Spatial Error				
Variable	Extent	Regression Coefficient		
		$ß_0$	$ß_1$	p-value
$Size_{Mean} \sim \psi_{Sky}$	Site	1.15	0.01	0.11
	North Plot	1.55	0.00	0.48
	South Plot	1.05	0.01	0.12
$Size_{90th} \sim \psi_{Sky}$	Site	-5.5	**0.26**	**0.00**
	North Plot	-4.28	**0.22**	**0.02**
	South Plot	0.76	0.02	0.75
$Size_{Max} \sim \psi_{Sky}$	Site	-7.85	**0.34**	**<0.01**
	North Plot	-13.55	**0.42**	**<0.01**
	South Plot	-9.32	**0.38**	**<0.01**
$Size_{Mean} \sim \Sigma_{Sunfleck}$	Site	1.72	0.00	0.59
	North Plot	1.29	0.00	0.99
	South Plot	1.82	0.00	0.83
$Size_{90th} \sim \Sigma_{Sunfleck}$	Site	6.68	0.01	0.32
	North Plot	0.05	0.03	0.11
	South Plot	5.92	**0.03**	**0.01**
$Size_{Max} \sim \Sigma_{Sunfleck}$	Site	3.93	**0.02**	**0.04**
	North Plot	7.66	0.01	0.68
	South Plot	6.50	**0.03**	**0.01**
$Size_{Mean} \sim \Sigma_{Shortwave}$	Site	1.75	0.01	0.82
	North Plot	1.83	0.00	0.89
	South Plot	1.82	-0.01	0.87
$Size_{90th} \sim \Sigma_{Shortwave}$	Site	7.48	0.09	0.68
	North Plot	5.38	0.23	0.66
	South Plot	6.06	0.59	0.07
$Size_{Max} \sim \Sigma_{Shortwave}$	Site	5.26	0.41	0.18
	North Plot	10.48	-0.09	0.85
	South Plot	6.27	**0.82**	**0.02**

Table C 26. Spatial error model multiple regressions for the Jan2014 event at the North Site.

Jan2014 - North Site – Spatial Error						
Variable	Extent	Regression Coefficient				
		$ß_0$	$ß_1$	p-value	$ß_2$	p-value
$Size_{Mean} \sim \psi_{Sky} + \Sigma_{Sunfleck}$	Site	-0.36	**0.07**	**0.03**	0.00	0.11
	North Plot	-6.10	0.16	0.06	0.00	0.18
	South Plot	-13.01	**0.27**	**<0.01**	**-0.01**	**<0.01**
$Size_{Mean} \sim \psi_{Sky} + \Sigma_{Shortwave}$	Site	-0.11	0.07	0.07	-0.25	0.25
	North Plot	-3.78	0.11	0.21	-0.15	0.61
	South Plot	-14.11	**0.30**	**<0.01**	**-0.62**	**<0.01**
$Size_{90th} \sim \psi_{Sky} + \Sigma_{Sunfleck}$	Site	-1.29	0.12	0.03	0.00	0.07
	North Plot	-25.93	**0.50**	**<0.01**	**-0.02**	**<0.01**
	South Plot	-19.26	**0.39**	**<0.01**	**-0.01**	**<0.01**
$Size_{90th} \sim \psi_{Sky} + \Sigma_{Shortwave}$	Site	-0.69	0.11	0.07	-0.40	0.21
	North Plot	-22.92	0.45	<0.01	-0.98	0.06
	South Plot	-20.37	**0.42**	**<0.01**	**-0.69**	**<0.01**
$Size_{Max} \sim \psi_{Sky} + \Sigma_{Sunfleck}$	Site	-3.02	**0.17**	**<0.01**	**-0.01**	**<0.01**
	North Plot	-26.63	**0.54**	**<0.01**	**-0.03**	**<0.01**
	South Plot	-14.28	**0.33**	**<0.01**	**-0.01**	**<0.01**
$Size_{Max} \sim \psi_{Sky} + \Sigma_{Shortwave}$	Site	-2.66	**0.17**	**0.01**	**-0.79**	**0.02**
	North Plot	-22.60	**0.49**	**0.01**	**-1.45**	**0.02**
	South Plot	-15.58	**0.36**	**<0.01**	**-0.74**	**<0.01**

Table C 27. Spatial error model multiple regressions for the Jan2014 event at the South Site.

Jan2014 - South Site – Spatial Error						
Variable	Extent	Regression Coefficient				
		ß$_0$	ß$_1$	p-value	ß$_2$	p-value
$Size_{Mean} \sim \psi_{Sky} + \Sigma_{Sunfleck}$	Site	-0.15	**0.04**	**0.01**	**-0.02**	**<0.01**
	North Plot	0.68	0.02	0.22	0.00	0.63
	South Plot	3.15	**-0.01**	**0.05**	0.00	0.37
$Size_{Mean} \sim \psi_{Sky} + \Sigma_{Shortwave}$	Site	0.02	**0.04**	**<0.01**	**-0.10**	**<0.01**
	North Plot	1.07	0.02	0.16	-0.08	0.40
	South Plot	3.24	**-0.01**	**0.02**	-0.02	0.23
$Size_{90th} \sim \psi_{Sky} + \Sigma_{Sunfleck}$	Site	-0.46	**0.05**	**<0.01**	**0.00**	**<0.01**
	North Plot	0.65	0.03	0.12	0.00	0.45
	South Plot	3.81	-0.01	0.10	0.00	0.36
$Size_{90th} \sim \psi_{Sky} + \Sigma_{Shortwave}$	Site	-0.19	**0.05**	**<0.01**	**-0.13**	**<0.01**
	North Plot	1.01	0.03	0.10	-0.12	0.36
	South Plot	3.94	-0.01	0.06	-0.04	0.23
$Size_{Max} \sim \psi_{Sky} + \Sigma_{Sunfleck}$	Site	-0.39	**0.05**	**<0.01**	**0.00**	**0.01**
	North Plot	1.04	0.02	0.23	0.00	0.49
	South Plot	3.77	-0.01	0.22	0.00	0.78
$Size_{Max} \sim \psi_{Sky} + \Sigma_{Shortwave}$	Site	-0.17	**0.06**	**<0.01**	**-0.12**	**<0.01**
	North Plot	1.31	0.03	0.20	-0.10	0.45
	South Plot	3.80	-0.01	0.20	-0.02	0.62

Table C 28. Spatial error model multiple regressions for the April2014 event at the South Site.

April2014 - South Site – Spatial Error						
Variable	Extent	Regression Coefficient				
		ß$_0$	ß$_1$	p-value	ß$_2$	p-value
$Size_{actual} \sim \psi_{Sky} + \Sigma_{Sunfleck}$	Site	1.61	-0.02	0.12	0.00	0.20
	North Plot	2.78	**-0.06**	**0.01**	0.00	0.11
	South Plot	-1.57	**0.05**	**<0.01**	**-0.01**	**<0.01**
$Size_{actual} \sim \psi_{Sky} + \Sigma_{Shortwave}$	Site	1.55	-0.01	0.45	0.02	0.72
	North Plot	2.89	-0.04	0.31	0.04	0.83
	South Plot	-1.92	**0.07**	**<0.01**	**-0.04**	**<0.01**

Table C 29. Spatial error model multiple regressions for the Jan2015 event at the North Site.

Jan2015 - North Site – Spatial Error						
Variable	Extent	Regression Coefficient				
		ß$_0$	ß$_1$	p-value	ß$_2$	p-value
$Size_{Mean} \sim \psi_{Sky} + \Sigma_{Sunfleck}$	Site	-4.03	**0.20**	**<0.01**	**-0.01**	**<0.01**
	North Plot	-10.20	0.27	0.42	-0.01	0.10
	South Plot	-4.53	**0.21**	**<0.01**	-0.01	0.08
$Size_{Mean} \sim \psi_{Sky} + \Sigma_{Shortwave}$	Site	-4.60	**0.23**	**<0.01**	**-1.43**	**<0.01**
	North Plot	-8.01	0.25	0.63	-1.05	0.29
	South Plot	-4.76	**0.23**	**<0.01**	**-1.15**	**<0.01**
$Size_{90th} \sim \psi_{Sky} + \Sigma_{Sunfleck}$	Site	-3.94	**0.23**	**<0.01**	**-0.01**	**<0.01**
	North Plot	-11.10	0.31	0.34	-0.01	0.25
	South Plot	-5.11	**0.26**	**<0.01**	-0.01	0.09
$Size_{90th} \sim \psi_{Sky} + \Sigma_{Shortwave}$	Site	-4.41	**0.26**	**<0.01**	**-1.25**	**0.01**
	North Plot	-8.52	0.28	0.54	-0.72	0.57
	South Plot	-5.34	**0.28**	**<0.01**	**-1.08**	**0.02**
$Size_{Max} \sim \psi_{Sky} + \Sigma_{Sunfleck}$	Site	-5.84	**0.28**	**<0.01**	**-0.01**	**0.03**
	North Plot	-17.41	0.42	0.29	-0.01	0.45
	South Plot	-7.05	**0.31**	**<0.01**	-0.01	0.16
$Size_{Max} \sim \psi_{Sky} + \Sigma_{Shortwave}$	Site	-6.29	**0.30**	**<0.01**	-1.15	0.05
	North Plot	-14.70	0.38	0.44	-0.71	0.73
	South Plot	-7.17	**0.32**	**<0.01**	-0.83	0.08

Table C 30. Spatial error model multiple regressions for the Jan2015 event at the South Site.

Jan2015 - South Site – Spatial Error						
Variable	Extent	Regression Coefficient				
		$ß_0$	$ß_1$	p-value	$ß_2$	p-value
$Size_{Mean} \sim \psi_{Sky} + \Sigma_{Sunfleck}$	Site	1.02	**0.01**	**0.01**	0.00	0.41
	North Plot	2.52	-0.01	0.58	**-0.01**	**0.01**
	South Plot	0.19	**0.03**	**<0.01**	0.00	0.06
$Size_{Mean} \sim \psi_{Sky} + \Sigma_{Shortwave}$	Site	1.02	**0.01**	**<0.01**	-0.02	0.20
	North Plot	2.49	-0.01	0.79	0.01	0.87
	South Plot	0.28	**0.03**	**<0.01**	-0.06	0.06
$Size_{90th} \sim \psi_{Sky} + \Sigma_{Sunfleck}$	Site	-10.94	**0.40**	**<0.01**	**-0.01**	**<0.01**
	North Plot	-2.18	**0.32**	**<0.01**	-0.03	0.21
	South Plot	-12.30	**0.42**	**<0.01**	-0.01	0.64
$Size_{90th} \sim \psi_{Sky} + \Sigma_{Shortwave}$	Site	-10.57	**0.40**	**<0.01**	**-0.52**	**<0.01**
	North Plot	-3.05	**0.33**	**<0.01**	-0.85	0.34
	South Plot	-12.01	**0.42**	**<0.01**	**-0.41**	**0.02**
$Size_{Max} \sim \psi_{Sky} + \Sigma_{Sunfleck}$	Site	-13.82	**0.48**	**<0.01**	**-0.01**	**<0.01**
	North Plot	-4.11	**0.37**	**<0.01**	-0.02	0.93
	South Plot	-15.34	**0.50**	**<0.01**	-0.01	0.20
$Size_{Max} \sim \psi_{Sky} + \Sigma_{Shortwave}$	Site	-13.39	**0.48**	**<0.01**	**-0.53**	**<0.01**
	North Plot	-4.87	**0.38**	**<0.01**	**-0.78**	**0.04**
	South Plot	-14.58	**0.48**	**<0.01**	-0.30	0.70

APPENDIX D

OVERFIT REGRESSION TREES

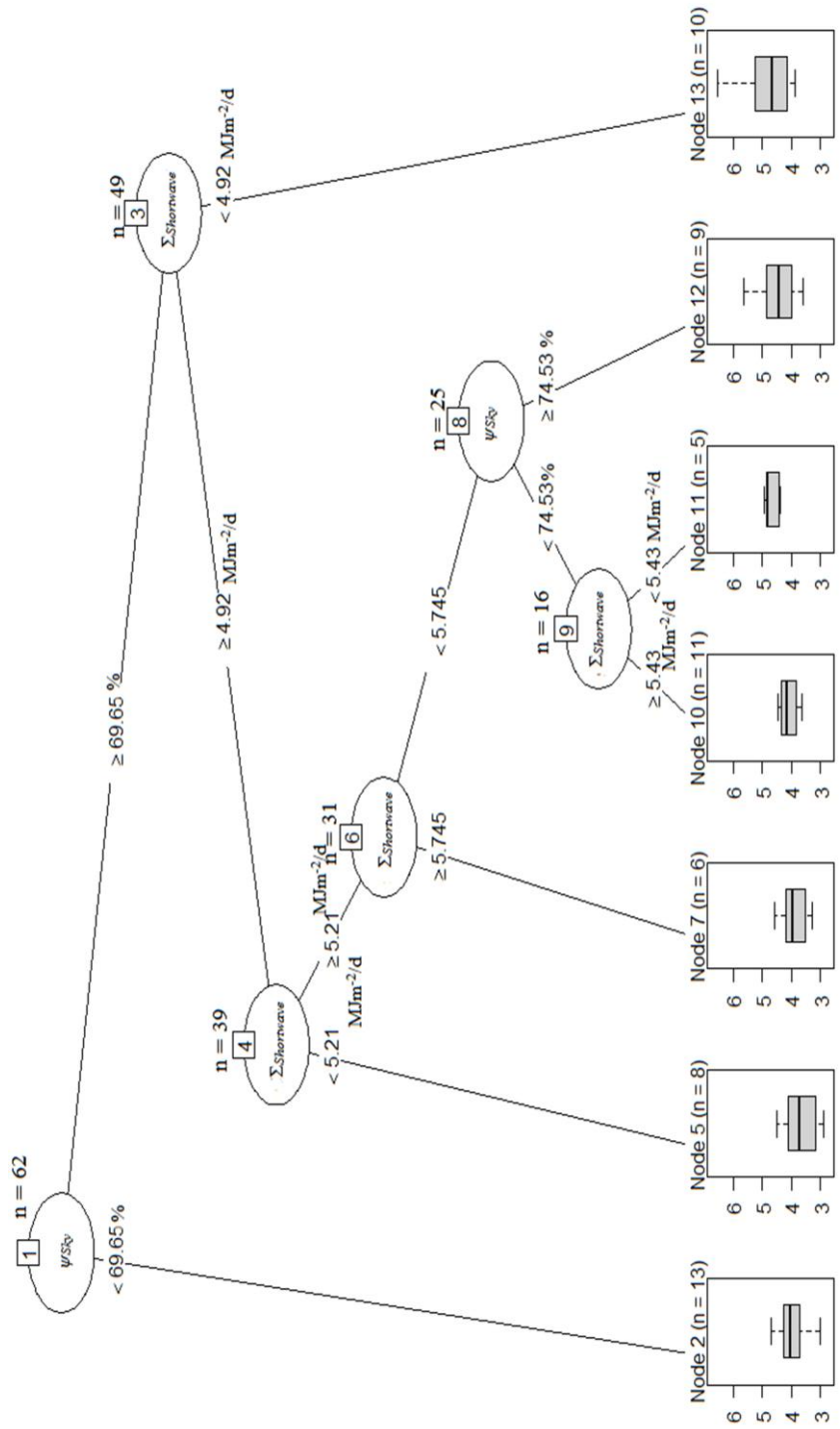


Figure D 1. Overfit regression tree for $Size_{Mean}$ for Jan2014 at the North Site with boxplots. For each boxplot the bold line represents the median, the box represents the interquartile range, and the whiskers represent 1.5x the interquartile range. Dots represent outlier values.

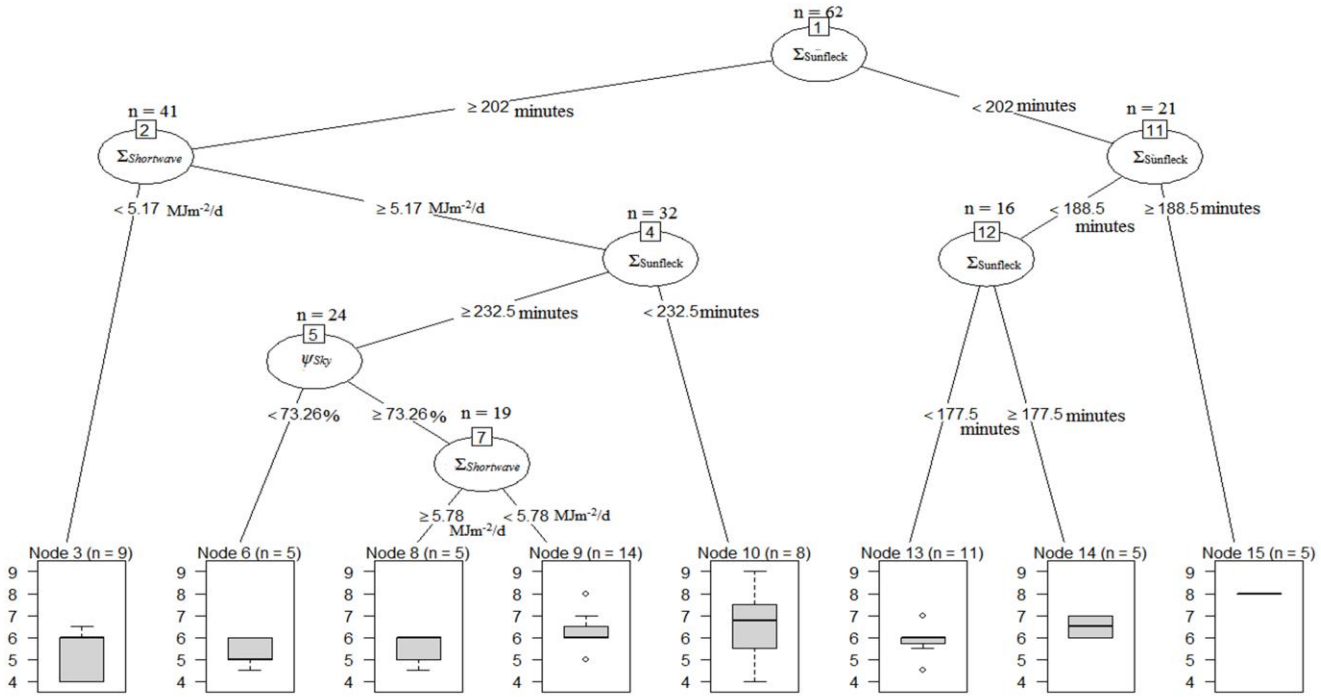


Figure D 2. Overfit regression tree for $Size_{Max}$ for Jan2014 at the North Site with boxplots. For each boxplot the bold line represents the median, the box represents the interquartile range, and the whiskers represent 1.5x the interquartile range. Dots represent outlier values.

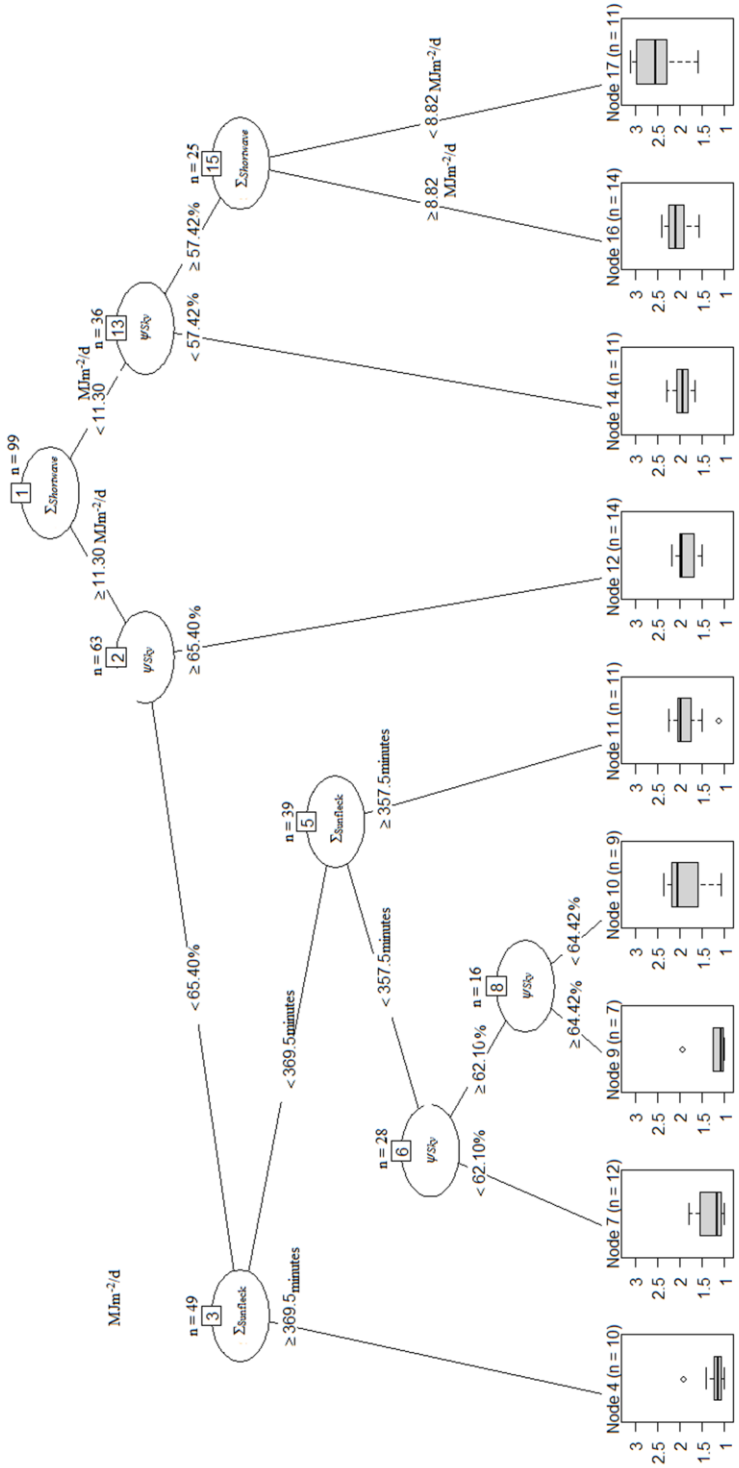


Figure D 3. Overfit regression tree for Size$_{Mean}$ for Jan2014 at the South Site with boxplots. For each boxplot the bold line represents the median, the box represents the interquartile range, and the whiskers represent 1.5x the interquartile range. Dots represent outlier values.

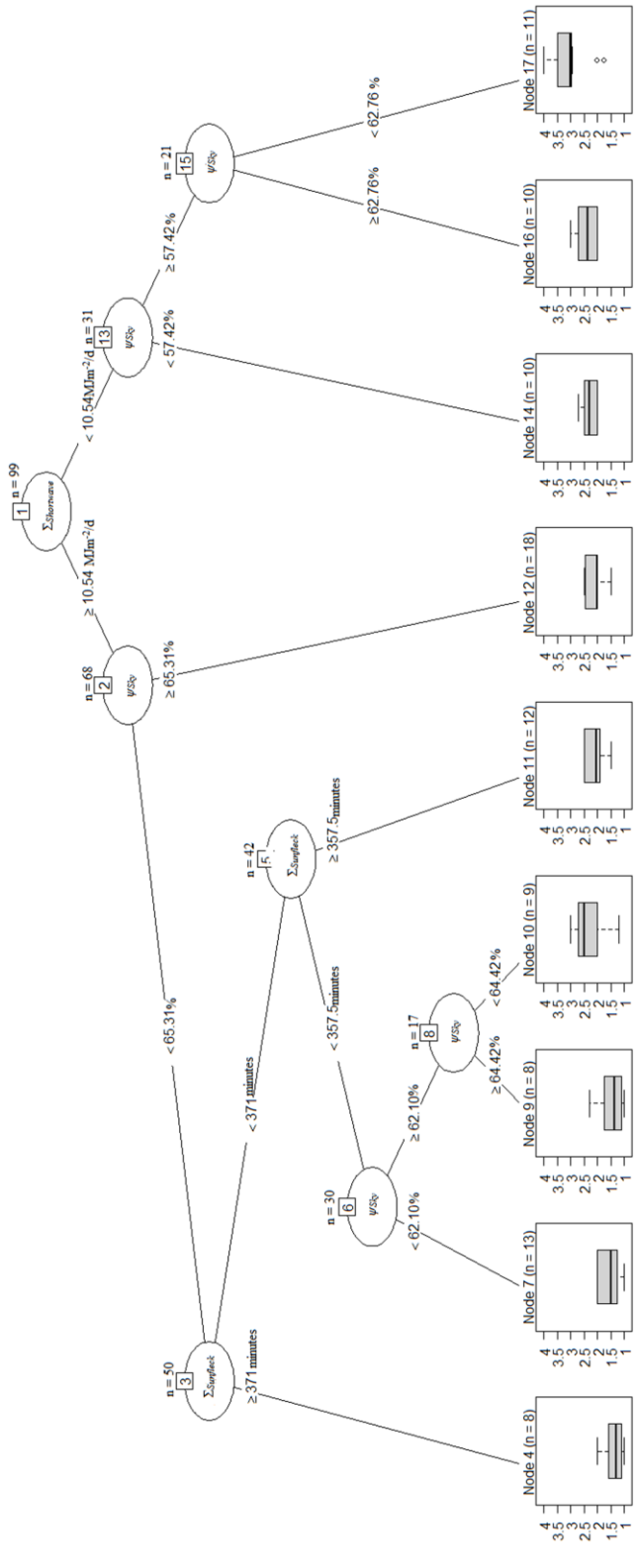


Figure D 4. Overfit regression tree for Size$_{90th}$ for Jan2014 at the South Site with boxplots. For each boxplot the bold line represents the median, the box represents the interquartile range, and the whiskers represent 1.5x the interquartile range. Dots represent outlier values.

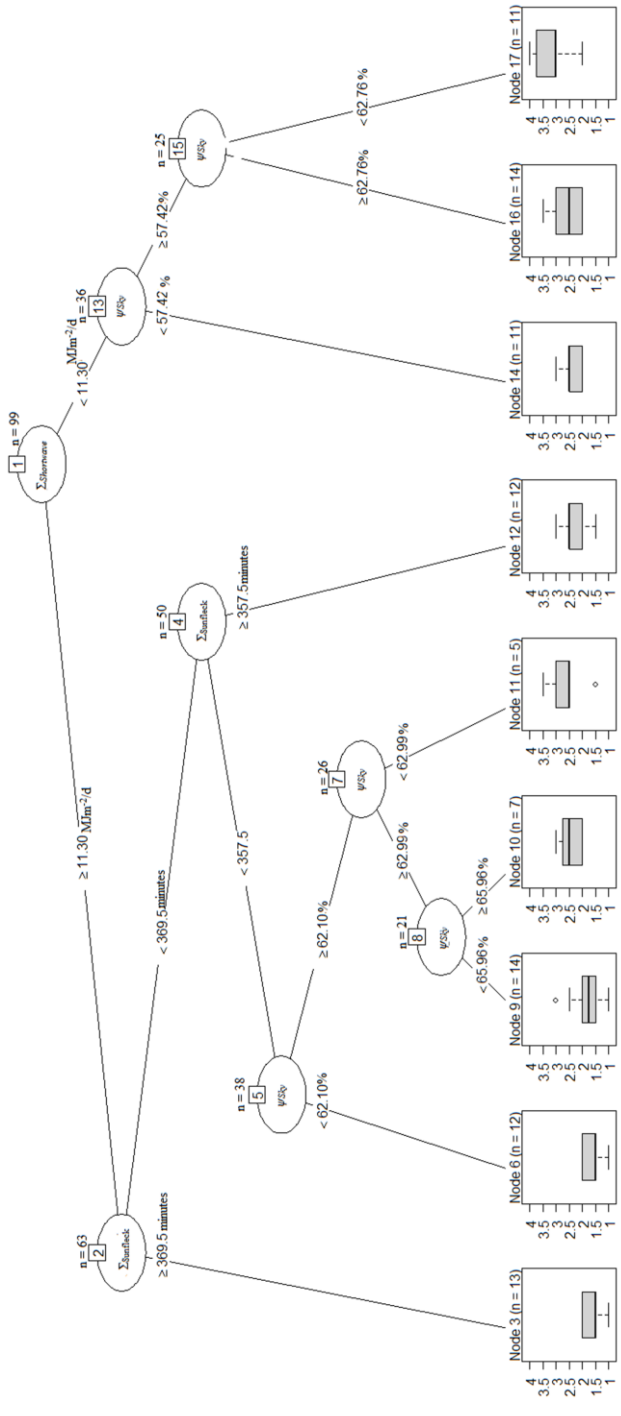


Figure D 5. Overfit regression tree for Size$_{Max}$ for Jan2014 at the South Site with boxplots. For each boxplot the bold line represents the median, the box represents the interquartile range, and the whiskers represent 1.5x the interquartile range. Dots represent outlier values.

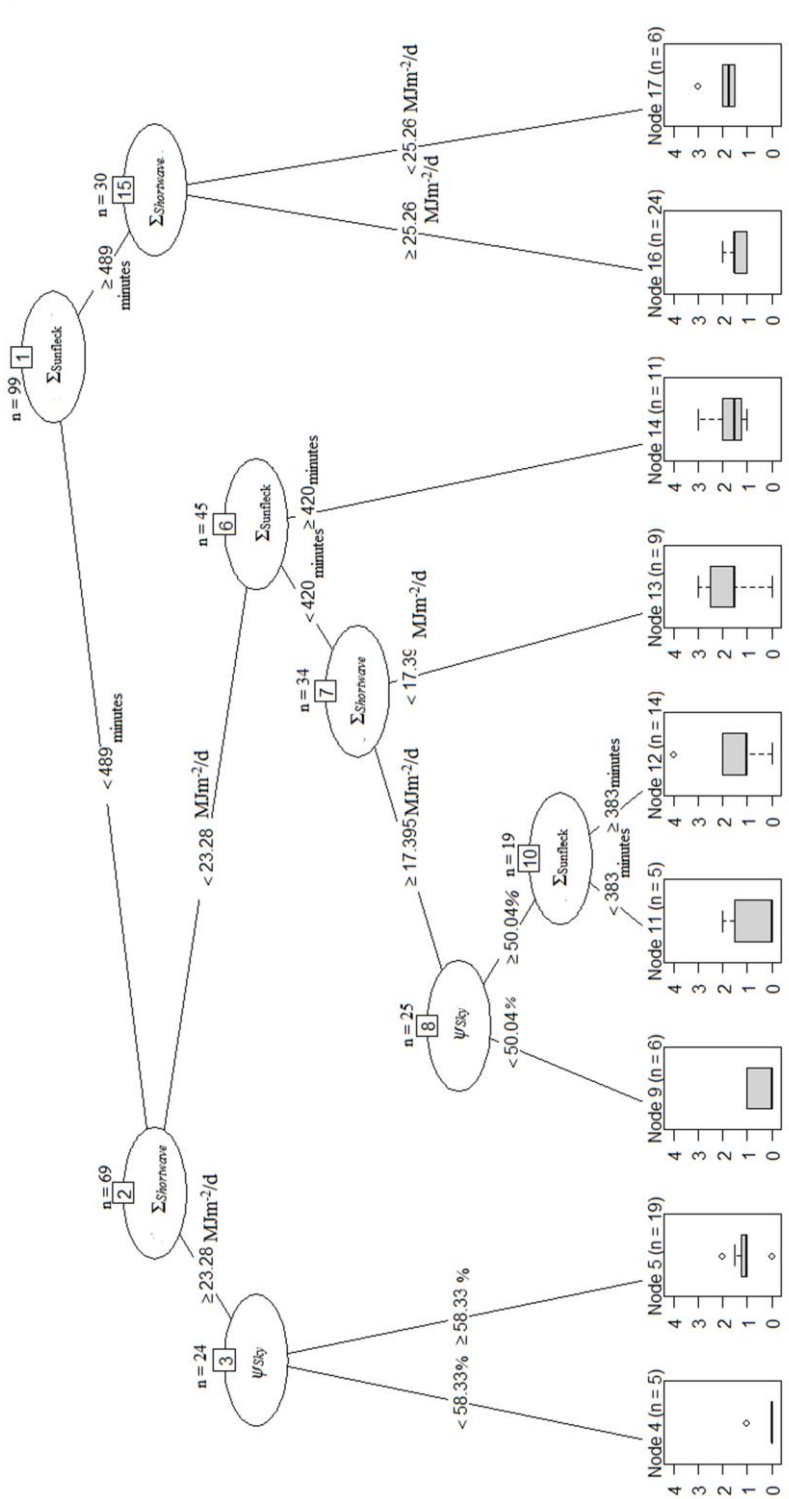


Figure D 6. Overfit regression tree for Size$_{Actual}$ for April2014 at the South Site with boxplots. For each boxplot the bold line represents the median, the box represents the interquartile range, and the whiskers represent 1.5x the interquartile range. Dots represent outlier values.

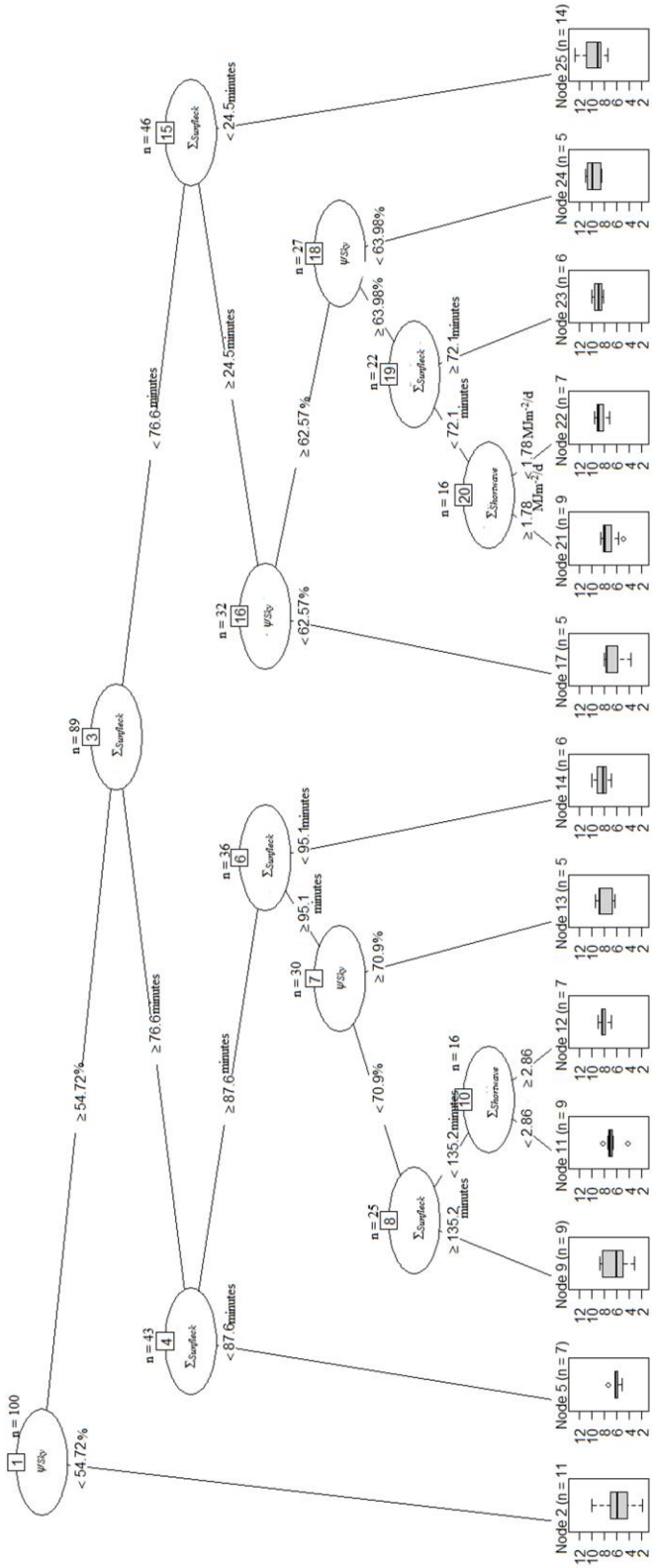


Figure D 7. Overfit regression tree for Size$_{Mean}$ for Jan2015 at the North Site with boxplots. For each boxplot the bold line represents the median, the box represents the interquartile range, and the whiskers represent 1.5x the interquartile range. Dots represent outlier values.

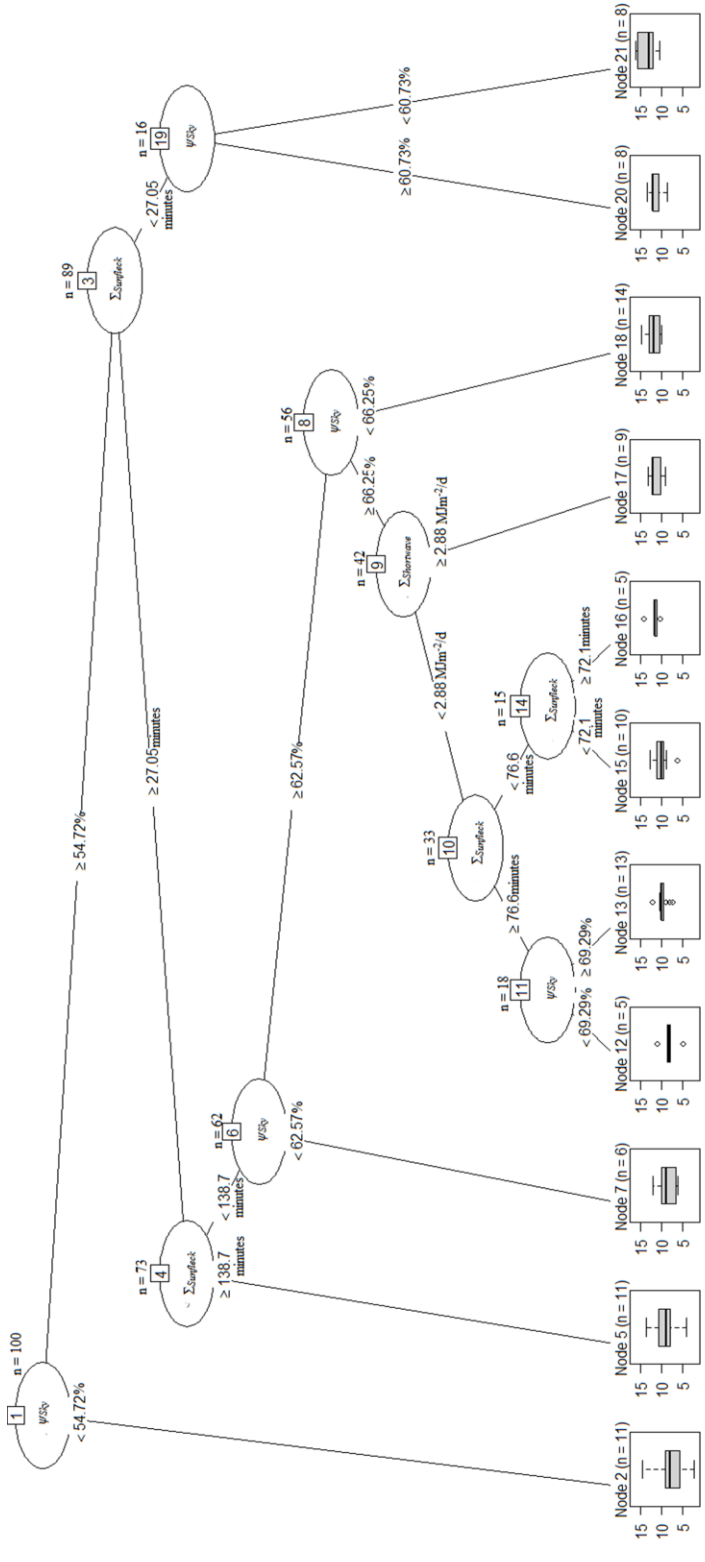


Figure D 8. Overfit regression tree for Size$_{90th}$ for Jan2015 at the North Site with boxplots. For each boxplot the bold line represents the median, the box represents the interquartile range, and the whiskers represent 1.5x the interquartile range. Dots represent outlier values.

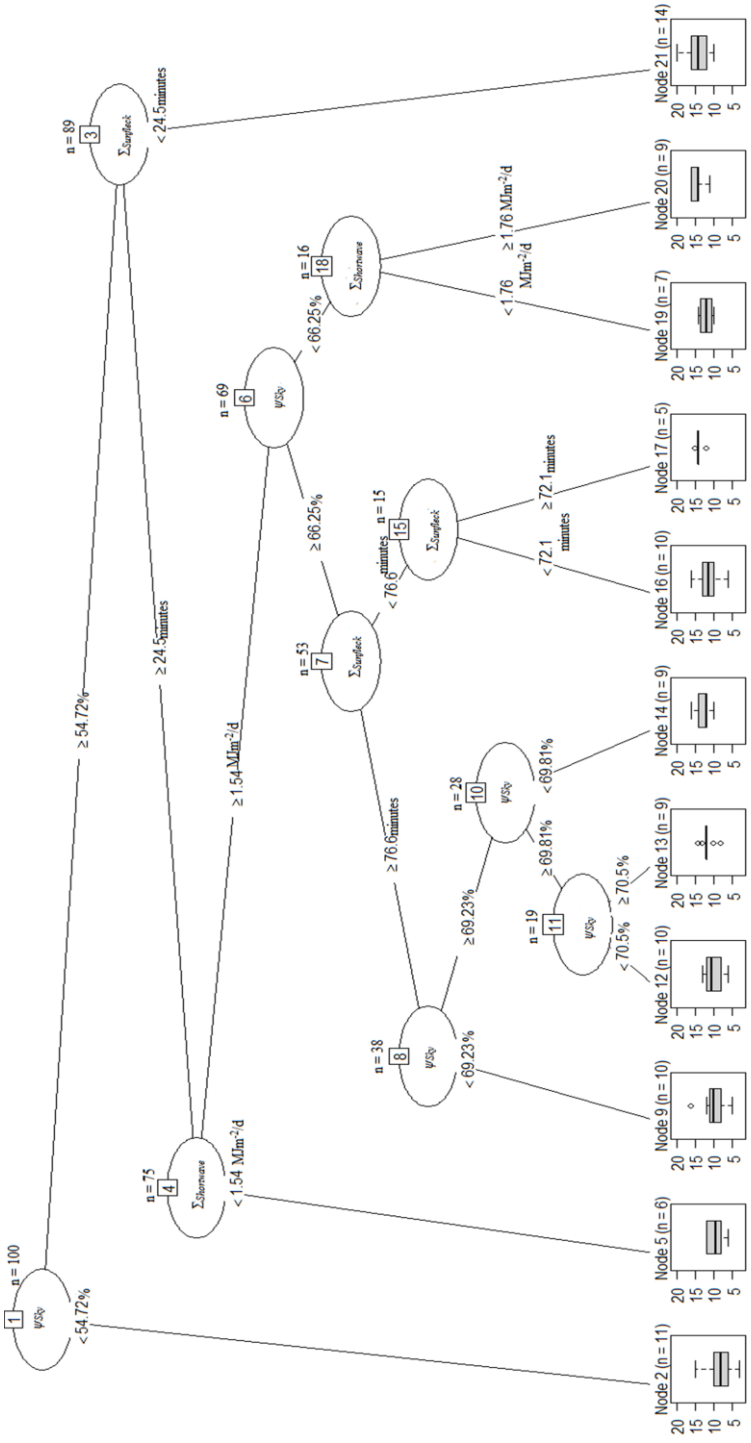


Figure D 9. Overfit regression tree for $Size_{Max}$ for Jan2015 at the North Site with boxplots. For each boxplot the bold line represents the median, the box represents the interquartile range, and the whiskers represent 1.5x the interquartile range. Dots represent outlier values.

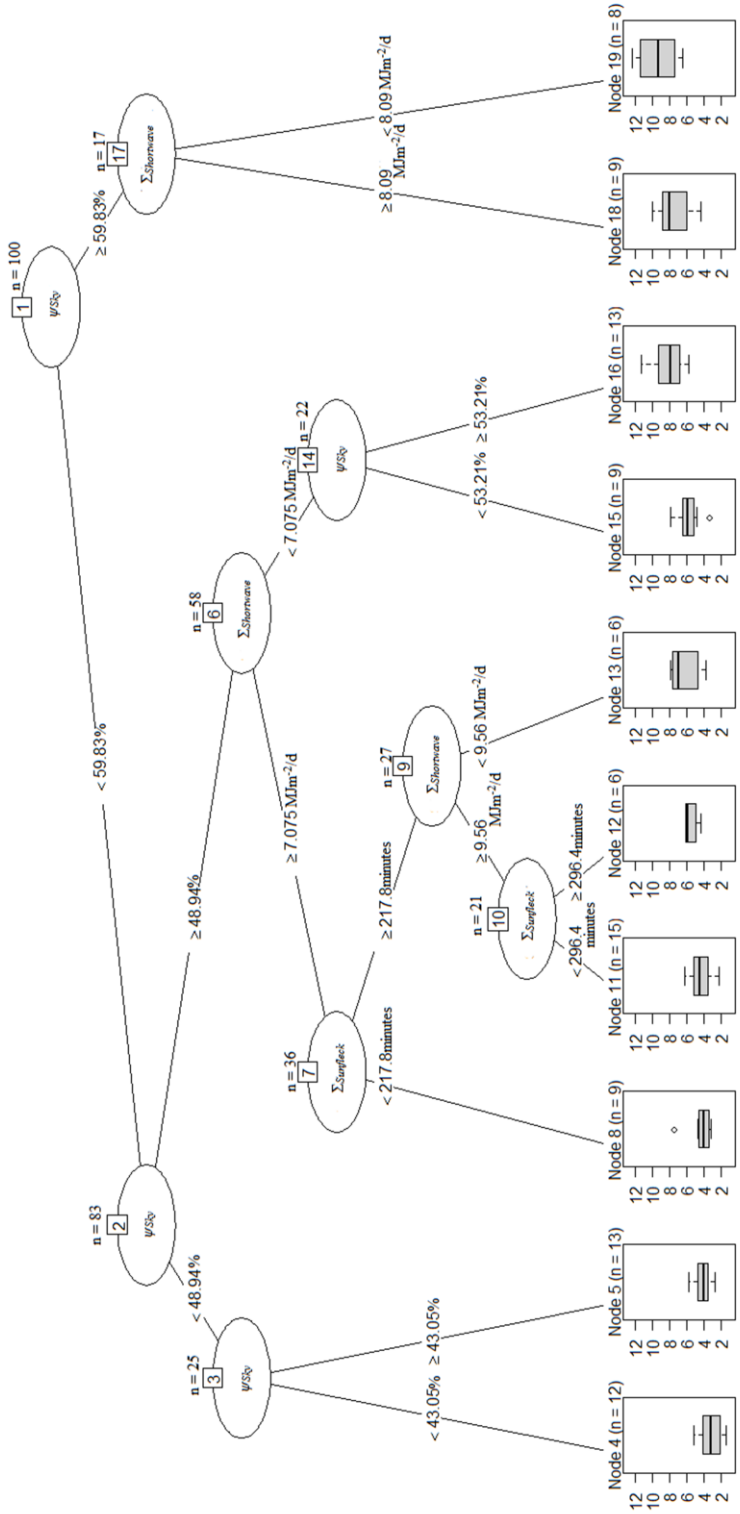


Figure D 10. Overfit regression tree for Size$_{Mean}$ for Jan2015 at the South Site with boxplots. For each boxplot the bold line represents the median, the box represents the interquartile range, and the whiskers represent 1.5x the interquartile range. Dots represent outlier values.

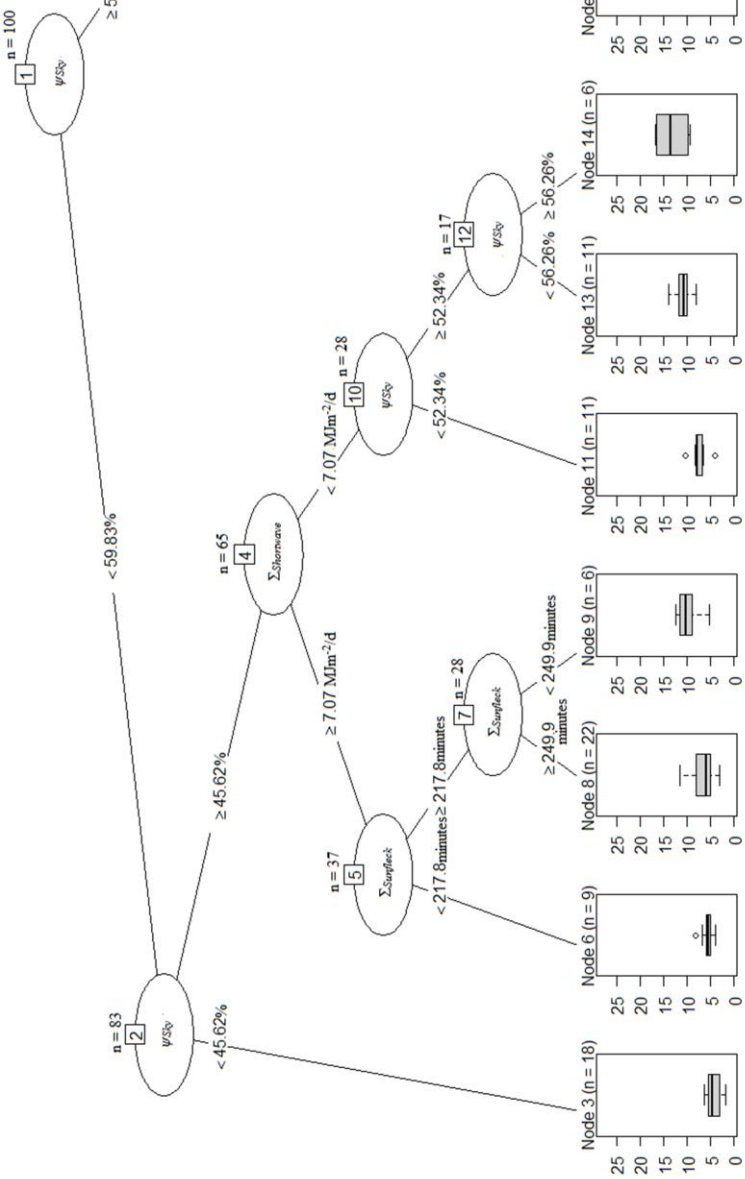


Figure D 11. Overfit regression tree for Size$_{90th}$ for Jan2015 at the South Site with boxplots. For each boxplot the bold line represents the median, the box represents the interquartile range, and the whiskers represent 1.5x the interquartile range. Dots represent outlier values.

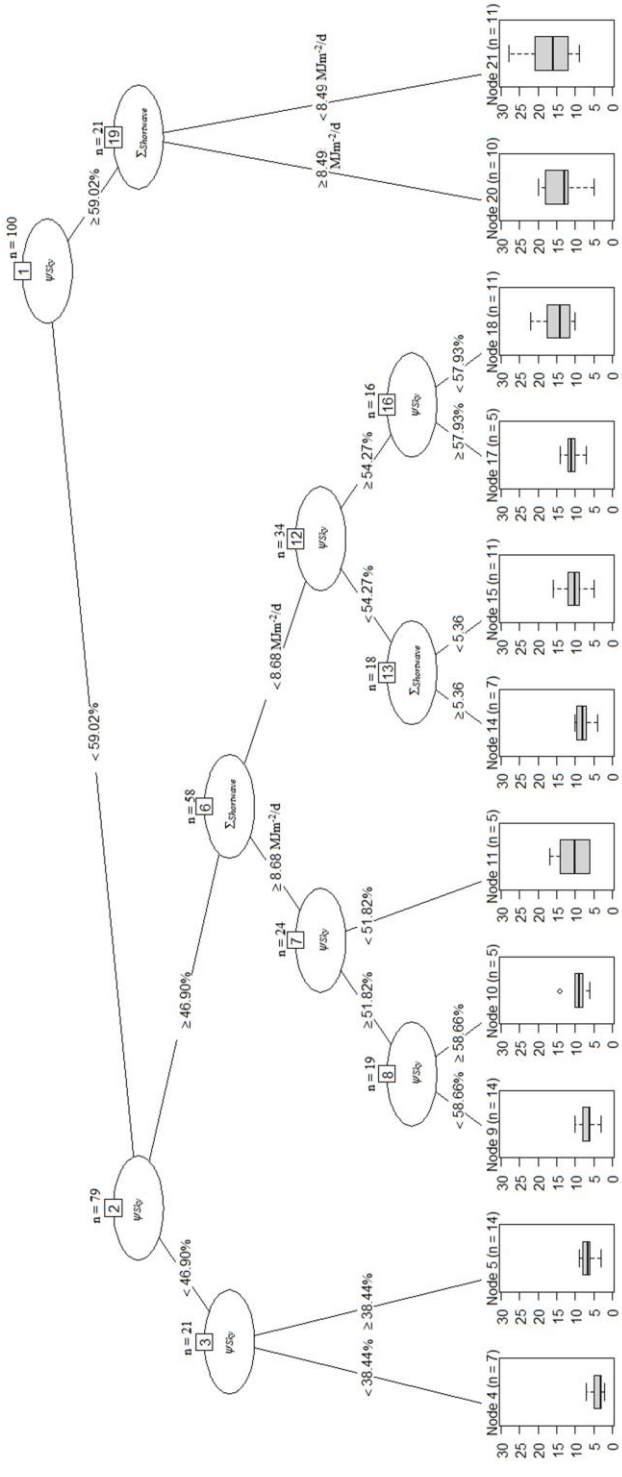


Figure D 12. Overfit regression tree for $Size_{Max}$ for Jan2015 at the South Site with boxplots. For each boxplot the bold line represents the median, the box represents the interquartile range, and the whiskers represent 1.5x the interquartile range. Dots represent outlier values.

APPENDIX E

CAMERA CALIBRATION

Table E 1. Office calibration data.

Angle	Distance (pixels)
3.814075	82
7.594643	170
11.30993	255
14.93142	332
18.43495	413
21.80141	487
25.01689	556
28.07249	621
30.96376	684
33.69007	739
36.25384	790
38.65981	840
40.91438	887
43.02507	931
45	1020
46.97493	1063
49.08562	1108
51.34019	1157
53.74616	1207
56.30993	1259
59.03624	1315
61.92751	1372
64.98311	1433
68.19859	1495
71.56505	1559
75.06858	1623
78.69007	1686
82.40536	1750
86.18593	1815
90	1864

Table E 2. Field calibration data from the 10 m building distance.

Angle	Distance (pixels)
13	268
16	323
18	357
19	400
22	463
23.5	427
30	616
36	742
45	920
53.5	1173

Table E 3. Field calibration data from the 15 m building distance.

Angle	Distance (pixels)
18.5	424
22.5	491
24	539
27	600
31	668
35.5	754
40	862
46	1000
54	1172
66	1381

Table E 4. Calibration file used in Gap Light Analyzer.

Angle	Distance (pixels)
0	0
5	117.2741
10	224.3286
15	331.3831
20	438.4376
25	545.4921
30	652.5466
35	759.6011
40	866.6556
45	973.7101
50	1080.765
55	1187.819
60	1294.874
65	1401.928
70	1508.983
75	1616.037
80	1723.092
85	1830.146
90	1937.201